Development of the diamond detector based real-time monitoring system for the ELI-NP gamma beam source

Themistoklis Williams

NNT : 2018SACLS277

Thèse de doctorat

Development of the diamond detector based real-time monitoring system for the ELI-NP gamma beam source

Thèse de doctorat de l'Université Paris-Saclay
préparée à l'Université Paris-Sud

Ecole doctorale n°576: Particules, Hadrons, Energie, Noyau, Instrumentation, Imagerie, Cosmos et Simulation (PHENIICS)
Spécialité de doctorat : Physique des accélérateurs

Thèse présentée et soutenue à Orsay, le 04/10/18, par

THEMISTOKLIS WILLIAMS

Composition du Jury :

Achille Stocchi Professeur, Université Paris-Sud (LAL)	Président
Marco Costa Professeur, Université de Turin	Rapporteur
Alessandro Variola Directeur de recherche, INFN (Frascati)	Rapporteur
Erich Griesmayer Professeur, Université de Vienne	Examinateur
Fabian Zomer Professeur, Université Paris-Sud (LAL)	Directeur de thèse
Aurélien Martens Chargé de recherche, CNRS/LAL	Invité

Laboratoire de l'Accélérateur Linéaire n° LAL 18-017

Remerciements

Je tiens tout d'abord à remercier Aurélien. Sa discipline et sa supervision continue ont assuré que je termine ma thèse dans les temps. Merci à Fabian, qui a supervisé de plus loin mais en trouvant toujours les bons mots pour me guider dans la bonne direction. Merci aux deux Kevin, qui ont eu des roles capitaux lors des diverses experiences présentées dans ce manuscrit.

Je veux remercier Alessandro Variola et Marco Costa d'avoir accepté d'être rapporteurs dans le jury pour ma soutenance de thèse et Achille Stocchi pour l'avoir présidé. Un grand merci à Erich Griesmayer qui en plus d'avoir été examinateur, m'a souvent aidé sur les differentes problématiques du détecteur-diamant.

Je souhaite remercier tout les thésards du groupe, Cheikh, Pierre, Xing, Huan et Loic ainsi que Christian et Titouan pour leur bonne humeur quotidienne et les nombreuses discussions sur de sujets innombrables.

Un grand merci aux divers services administratifs et techniques du LAL pour leur aide continue durant toute ma période de doctorant.

Je remercie tous les colocataires du 49 rue Pierre Vermeir que j'ai pu cotoyer au cours de ces trois longues années: Angèle, Bérangere, Meggan, Madline, Guillaume, Laurent, Jun, Peppino, Yann, Pierre. Avec un merci particulier pour ma copine Ema avec qui on s'est soutenu pour terminer chacun notre thèse.

Finalement, je souhaite remercier ma famille de nombreux physiciens qui m'a inspiré et soutenu avant et pendant la thèse et continuera à le faire bien après.

Contents

List of Tables

List of Figures

Introduction

Light has been an interrogation and a fascination for humans for thousands of years but it is only in the last 150 years that our understanding of it has truly expanded. Quantum mechanics was of paramount importance in this process by putting forward the non-intuitive concept of particle-wave duality. Light can both be described as an elementary particle, the photon, and a wave with all the physical principles such as diffraction that it implies. In this thesis we will be mainly considering the particle approach, with an emphasis on the high energy end of the electromagnetic spectrum with gamma-rays between 1 and 20 MeV. This is the nominal energy range targeted for the ELI-NP Gamma Beam Source upon its completion. This machine is aiming to produce a pulsed gamma beam with an rms bandwidth inferior to 0.5% and a spectral density greater than 5000 photons/$(s.eV)$. To achieve this, a complex optical system, named recirculator, was developed to circulate a high power laser pulse 32 times. The path length is 16 ns so that, on each pass, at the centre of the optical system, this pulse can interact with an accelerated electron bunch that transfers its energy to the photons to generate a train of gamma rays at a rate of 100 Hz. Each macrobunch is composed of the aforementioned 32 pulses separated individually by 16 ns. Once the recirculator is installed and the machine running, it becomes an enclosed under-vacuum "black-box" system so a necessity arises to verify the superposition in space and time of the laser and electron bunches. This problem established the roadmap for my thesis. The chosen solution was the development of a monitoring system based on diamond technology capable of detecting gamma-rays with a time resolution under 16 ns and to be installed a few metres after the interaction point.

Chapter 1 will focus on the history of gamma-rays. First of all, the context in which they were discovered in 1900 is exposed, before we look at some of their nuclear research applications and therapeutic uses in the 21st century. The subject of the various instruments used to detect them is also broached, with practical examples given for each detector type.

Chapter 2 will look at two types of gamma-ray sources and how they are used by physicists, in fields of medicine, teaching or spectroscopy among others.

Radioactive material is the only natural source of gamma-rays on Earth. An excited nucleus goes to a more stable state by emitting a photon of a discrete energy level. These levels have been studied to great extent as it helps identifying nuclear elements in various fields. Man-made gamma-ray sources have only been feasible technically and economically for a couple of decades thanks to great technological advances in lasers and particle accelerators. The functioning principle is based on inverse Compton scattering: electrons are accelerated before being collided with the photons of a laser. There, an energy transfer allows the photons to go from visible light to gamma-rays. Different such machines exist across the world, our focus will be on two facilities where experiments were conducted during this doctoral project: the High Intensity gamma Source at Duke University in the United States of America and newSubaru at the University of Hyogo in Japan.

A third Compton interaction machine, namely the ELI-NP Gamma Beam Source, will be presented in Chapter 3. My laboratory, the *Laboratoire de l'Accélérateur Linéaire* (LAL), as a member of the European EuroGammaS consortium, was tasked with developing most of the optical components. The complex recirculator system allows 32 laser-electron interactions separated by 16 ns each.

One crucial aspect for the production of the gamma-beam is the synchronous arrival at the interaction point of the electron bunches with the laser pulses. This requires a careful synchronisation of all the components of the machine. Chapter 4 focuses on the synchronisation procedure of the photocathode laser system through the use of a balanced optical cross-correlator developed at LAL.

A number of auxiliary devices are then needed to ensure the quality and stability of the produced gamma-beam. One of these devices is the real-time monitoring system of the gamma-ray pulsed beam. A diamond detector acts as semi-conductor when a high voltage is applied to it. When a gamma-ray passing through deposits some energy through a physical interaction, a signal is captured. Information extracted from this is essential to verify the synchronous arrival with a $\Delta t < 1ps$ of the laser and electron pulses, as well as their spatial superposition. This needs to be done online with a detector independent of the recirculator as the latter will be an enclosed optical system, pre-aligned manually before being put under vacuum. The experimental tests to validate the diamond detector I have been working on are presented in Chapter 5. This is the first time, to our knowledge, that a diamond detector has been used to monitor a gamma beam.

Chapter 1

Gamma-rays

1.1 Light and the Electromagnetic Spectrum

Young with his double-slit experiment proved that light is a particle. It was named the photon from the greek $\phi\omega\varsigma$ which means light. It was then discovered that the photon can have a specific energy E given by its wavelength of propagation λ:

$$E = hc/\lambda \tag{1.1}$$

with h the Plank constant. The photons with a wavelength between 400 and 800 nm give the visible light spectrum from violet to red respectively. Beyond 800 nm comes the infrared band and then the micro- and radio-waves. For large wavelengths, the frequency $\nu = c/\lambda$ is more commonly used. Before 400nm comes the ultraviolet (UV) light and at even smaller wavelengths the X-rays. Gamma rays are the part of the electromagnetic spectrum with the shortest wavelengths and they are mostly expressed using their energy in electronVolt (eV) units. All these wavelengths are called collectively the electromagnetic spectrum and are represented in Figure 1.1.

1.2 History of gamma-rays

Paul Villard [1] was the first to report the detection of gamma-rays in 1900 using photographic plates. It was an accidental discovery as he was studying the alpha and beta radiations of radioactive radium discovered by his colleagues Pierre and Marie Curie a few years earlier. In his article, Villard says that he observed a third type of radiation that is non-deviable by a magnetic field and highly penetrating, capable of going through a sheet of lead.

The setup was fairly simple. A glass jar contains some radioactive material. A lead shield with a 6 mm aperture lets the various rays pass into a small area. A

magnetic field is applied to this region. A photographic plate detects the deviated rays while a second plate 25 cm away from the aperture collects the non-deviated rays, that can pass through black paper and even a sheet of lead, 0.2 mm thick. This sheet was to make sure that these rays are different from the alpha rays that were discovered previously by the Curies that presented extremely limited penetration through materials. Interestingly, he names this radiation X-rays in an article [2] a few months later having understood a common nature between these new rays and the X-rays that was a new area of promising physics at the time.

With his results being called into question, notably by his colleague Henri Becquerel [3], this radiation stayed unnamed for three years. Indeed, the first use of the term gamma-ray dates back to 1903 when Ernest Rutherford [4] described three types of radiation from radioactive material: alpha, beta and gamma-rays. This nomenclature is still used and now photons are commonly represented by the symbol γ.

1.3 Different definitions of gamma-rays

X-rays and gamma-rays are at the higher end of the electromagnetic spectrum in terms of energy but the limit between the two is not very well defined. Historically, the term X-ray is used for photons coming from atomic transitions while gamma-ray is preferred for photons from nuclear transitions. There is an overlap in energies as can be seen on Figure 1.1. For high-energy photons produced in other ways such as Compton Interaction Sources which will be discussed in detail in Section 2, both terms are used but we will be using the term gamma-ray exclusively to avoid any confusion.

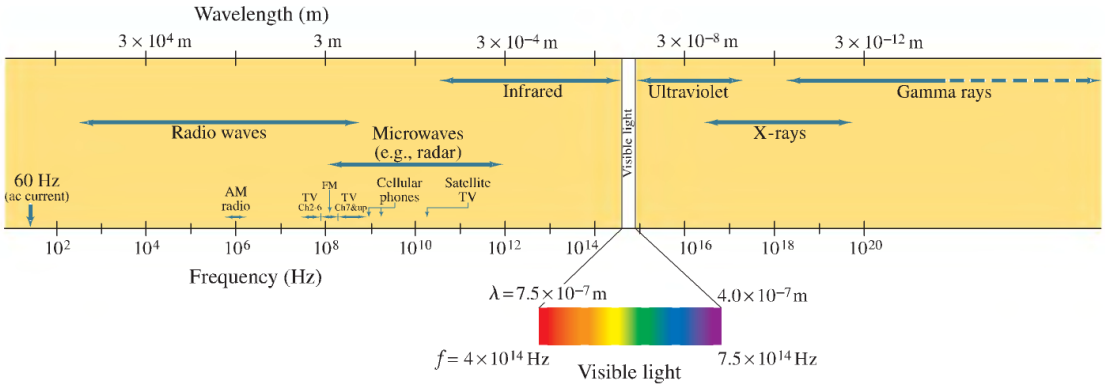

Figure 1.1: The Electromagnetic Spectrum. Reprinted from [5]

1.4 Gamma-ray detection

Gamma-ray detection is based on the interaction between high energy photons and electrons, be it through photoelectric effect, Compton scattering or pair production. The most commonly used detectors are presented in this section together with some of their applications.

1.4.1 X-ray film

The X-ray photographic film is the historic precursor of gamma detection as this is how they were first discovered by Villard, as explained in the previous section.

An X-ray photographic film is constituted of various layers [6–8]. The film base is made of plastic and should be transparent. It is there mainly for structural purposes to withstand use and tear. It comprises most of the thickness of the total film at 0.2 mm.

On both sides of this base are stacked successively an adhesive layer, a film emulsion and a protective layer. The adhesive layer lets the emulsion stick to the base and the protective layer allows it to resist to manipulation and time degradation.

The three layers can be applied on one (single-emulsion) or both (double-emulsion) sides of the film base. The double-emulsion film has the advantage of needing to expose the patient to less radiation to obtain an image. A diagram of such a film is shown schematically in Figure 1.2.

The emulsion is the active material that determines the features of the image. It is composed of silver halide crystals suspended in a gelatin. These crystals absorb the energy of incoming photons. Once the film has been exposed for long enough, it is developed by being put in direct contact with a chemical solution that makes the energised crystals go black. A final fixer solution is then applied to get a definitive image that will not be affected by other sources such as sunlight. This image is a density map of material traversed by the radiation.

The X-ray film is not used very much in the medical world any more due to its single-use limitation. However it has its uses for some peculiar cases such as dental radiography [6] where such a film is placed inside the mouth of the patient, thanks to the flexibility of the film. It is also widely used for industrial purposes such as flaw detection or thickness and spacing measurements in materials [9].

1.4.2 Gas-filled detectors

Gas-filled detectors are chambers filled up with sensitive gas. The encasing serves as an electrode and a thin wire placed in the centre of the chamber as a second electrode. A potential is applied between the two. When radiation goes through

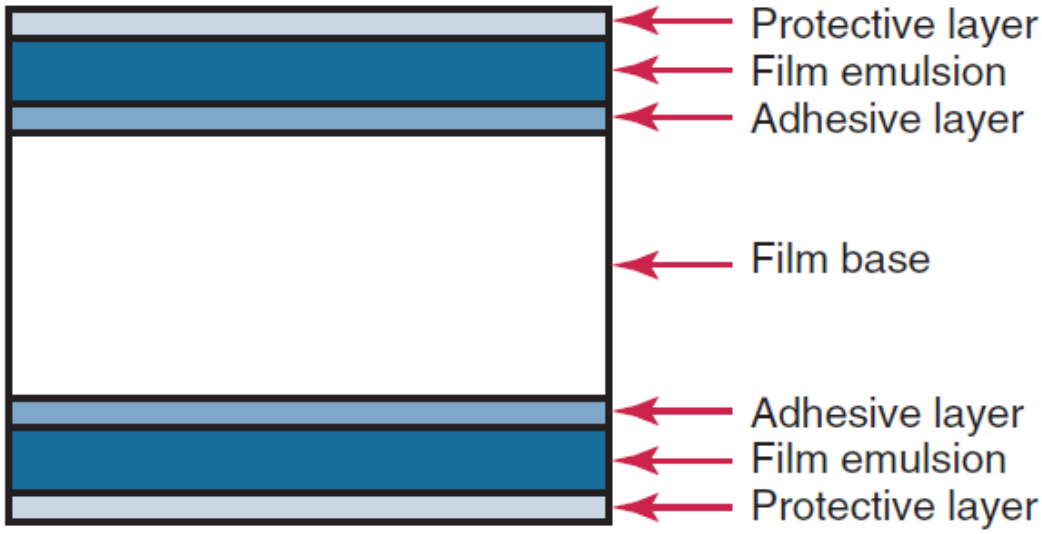

Figure 1.2: Diagram showing the various layers of an X-ray film. Reprinted from [6]

the chamber, gas atoms are ionised and the resulting free electrons are collected by an electrode which then emits an electrical signal to a readout.

The Geiger-Müller counter is an example of a gas-filled detector [10]. It is operated in such a way that the voltage between the electrodes is sufficiently high that an electron separated by the ionising radiation will create an avalanche of electrons through charge multiplication until saturation is reached. This allows the detector to be independent of the initial energy deposited by passing radiation and thus becoming a counter of ionising particles going through the gas. The drawback is obviously that any radiation may activate it. This type of detector is still routinely used for dosimetry. An example is making sure that areas were safe after the disaster at the Fukushima nuclear power plant [11].

A very concrete application of the gas-filled detectors is an object that was found in buildings around the world: the smoke detector [12]. Radioactive Americium is placed between two plates such that a current is flowing between them. The alpha radiation emitted by ^{241}Am ionises the air inside the detector. When smoke infiltrates between the two plates of the chamber, less charges reach the plates, the current drops and the alarm goes off. These smoke detectors present some risks due to the radioactive material they contain and are being phased out. In France [13], for example, their installation is prohibited in new buildings since 2011 and all existing ones must be replaced by optical smoke alarms before 2021.

1.4.3 Scintillators and Photo-multiplier tubes

The very first photomultiplier tube was invented in the 1930s by researchers at the RCA Manufacturing Company [14] and their principle of use has remained the same through the years with various technological improvements. The principle of operation of a photomultiplier is explained below [15]:

1. Photons come into the tube through a glass window.
2. The photons hit an electrode that releases electrons through the photoelectric effect.
3. These electrons, called photoelectrons, are focused with an electrode onto another surface called a dynode that generates more electrons through the secondary-electron emission effect.
4. The third step is repeated a number of times until enough electrons are created to obtain a discernible signal.
5. An anode collects the electrons generated by the last dynode.
6. The signal is read out by an acquisition system.

A scintillator is a luminescent material [16]. When gamma-rays pass through it, the atoms that constitute it are excited. When they relax, they emit photons of lower energy in the visible spectrum. This process is called fluorescence. Scintillator tubes are usually coupled to PMTs which offer a better response to photons in the visible range rather than the gamma range.

Six key aspects have to be considered when choosing a good scintillation material:

1. The conversion of the energy of the incoming photons into visible light.
2. The direct proportionality between the energy deposited and that emitted.
3. The transparency to the wavelength it emits such that there is no cascade of photons over a large time-period.
4. The absence of phosphorescent[1] properties.
5. The good optical quality and manufacturing techniques.
6. The refractive index that should be close to glass to facilitate coupling with PMTs.

[1]Phosphorescence is a similar physical phenomenon to fluorescence but the decay time from an excited state to a lower state is significantly longer.

An example of scintillator is sodium iodine that has been in use for the past 70 years [17]. One application of such a detector is uranium enrichment inspection [18]. The fundamentals of this technique [19] are based on observing the intensity of the gamma-rays line at 186 keV emitted by radioactive Uranium-235. If the depth of the sample D is large enough, the gamma-rays emitted on the side furthest away from the detector are reabsorbed in the material before being able to reach it thus reducing the effective sample depth seen by the detector to a distance shorter than D, D_c. This effect is independent of the isotopic composition of the uranium sample. Therefore, all samples with a depth above the critical point D_c are seen as infinite. Different samples can then be compared by looking at the intensity of the 186 keV line indicating the concentration of Uranium-235 as long as they are each isotropically uniform.

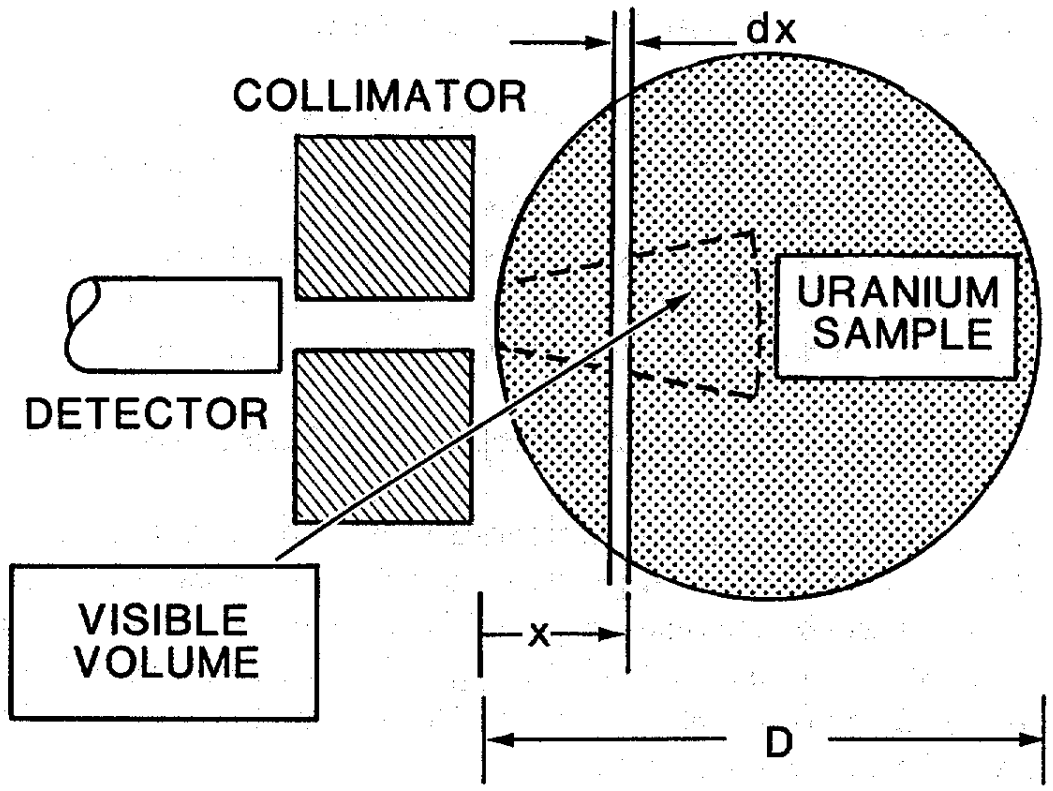

Figure 1.3: Diagram presenting the simplified detector setup for determining the enrichment levels of a uranium sample. Reprinted from [20] with the note: "*For purposes of illustration, the size of the visible volume compared with the detector and collimator is exaggerated. Normally the depth of the visible volume is much smaller than the source-to-detector distance.*"

1.4.4 Semiconductor detectors

In semiconductor detectors, the gamma-rays traverse the active material and deposit some energy which is transferred to the electrons of the material in the form of kinetic energy. These moving charges are encouraged to drift in the material by the bias voltage that is applied on two electrodes on either side of the semiconductor. The charge collected is proportional to the energy deposited by the original photon going through the detector.

Germanium is the most used material for this type of detectors as it presents the best electronic characteristics [20]. For example, germanium detectors are commonly used for nuclear resonance fluorescence experiments [21] which will be delved into in section 1.5.1.

An expensive material that presents semiconductor features when a high voltage is applied to it is diamond. An in-depth look at this will be shown in Chapter 4, as this is the type of detector that was used experimentally for this thesis.

1.5 Uses of gamma-rays

1.5.1 Nuclear research

One area of research that has existed since the 1950s with the help of gamma-rays is Nuclear Resonance Fluorescence (NRF) [22,23]. The principle is that photons of a specific energy come and excite a state of the nucleus. After a certain time, the nucleus releases a photon at a discrete energy level through a desexcitation mode. The nucleus can go through various energy levels before reaching its ground state releasing multiple fluorescent photons, as shown in Figure 1.4.

The energy scale of the photons for these interactions is of a few MeVs. The photon sources to perform such experiments are high-energy bremsstrahlung sources. In recent decades, precision measurements have required the development of Compton Interaction Sources. This is the subject of Section 2.

A spectrum of an NRF experiment performed at MIT High Voltage Research Lab [25] is shown in Figure 1.5. A volume of B_2O_3 powder ($30 \times 30 \times 30$ cm^3) and an Aluminium plate ($25 \times 25 \times 6.3$ cm^3) are irradiated by photons produced by bremsstrahlung effect in a target at the end of a Van de Graaff electron accelerator operating at 2.4 MeV. A germanium detector is placed at an angle of 140° from the photon beam to collect the NRF gamma-rays. The two peaks of ^{11}B and ^{27}Al at 2.12 and 2.21 MeV respectively are clearly distinguishable from the background. With a fine understanding of all possible fluorescence spectral lines, it is possible to evaluate the contents of any unknown sample. This is possible thanks to years and years of research into this subject. An example of such a study dating from

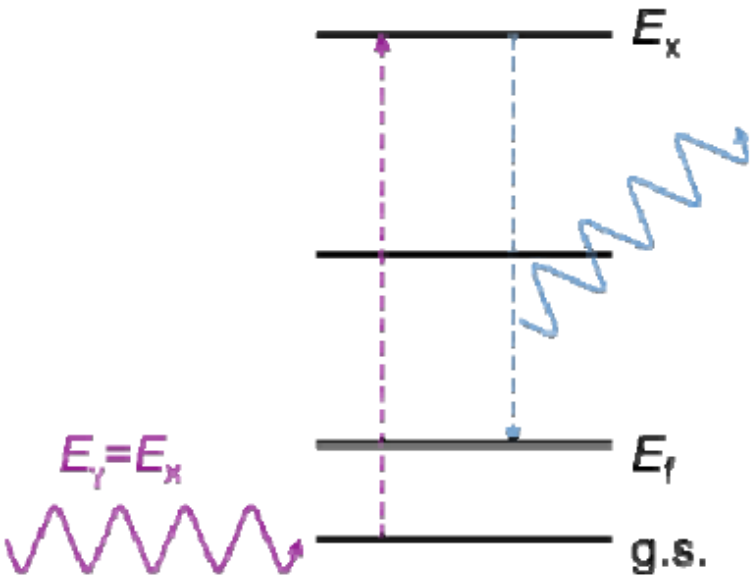

Figure 1.4: Diagram presenting the process of Nuclear Resonance Fluorescence. A photon with energy E_γ excites the nucleus to energy level E_x. A photon of energy $E_x - E_f$ is thereafter released when the nucleus transitions to an energy level E_f. Reprinted from [24]

.

1956 is given in [23] where Franz Metzger reports various fluorescence lines for Mercury, Thallium and Praseodymium.

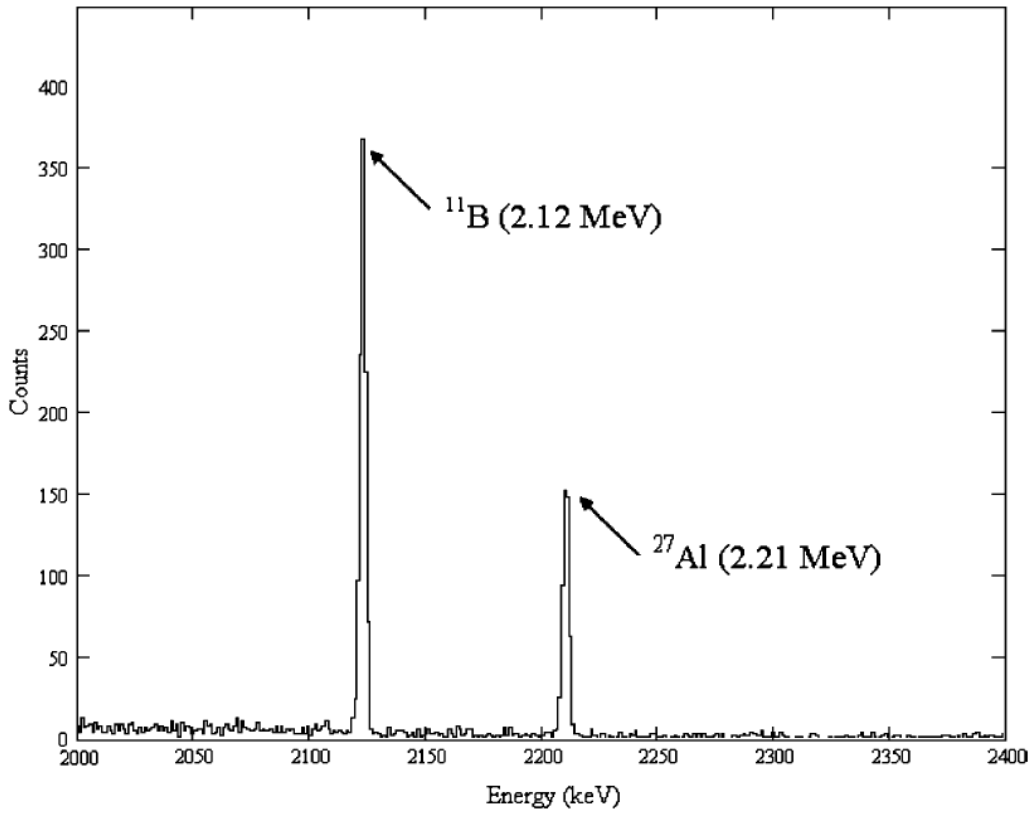

Figure 1.5: NRF Spectrum of a volume of B_2O_3 powder and Aluminium plate. Two lines at 2.12 and 2.21 MeV are clearly visible. They correspond to the known excited states of ^{11}B and ^{27}Al respectively. Reprinted from [25]

.

An interesting application of NRF is the non-intrusive inspection of cargo, invented by Bertozzi and Ledoux [25], but still at the prototype level. Multiple detectors are placed around a container as presented in Figure 1.6. The combination of these detectors allows a precise measurement of the concentration levels of all elements with $Z > 2$ inside the container. This in turn facilitates verifiying the presence or absence of nuclear material, explosives, as well as toxic and poisonous compounds which are all highly regulated due to their importance in military equipment and counter-terrorism intelligence.

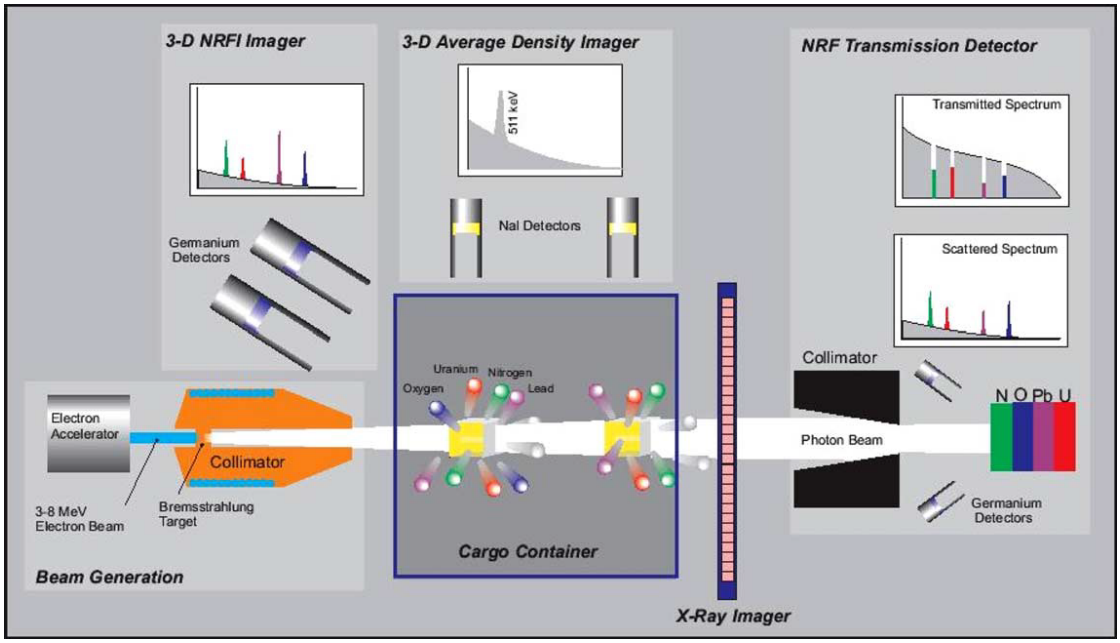

Figure 1.6: Schematic diagram of a nuclear resonance fluorescence imaging set-up for a cargo container. Reprinted from [25]

.

1.5.2 Therapeutic uses

A good understanding of the detection mechanisms of gamma-rays is an essential part in the medical imaging technique of Positron Emission Tomography (PET) [26]. This technique is commonly used to find the precise location of a cancerous tumour in a sick patient. He is first given an injection of a sugar marked with a radioactive tracer. The tracer needs to emit a positron through its decay for this process to be effective. The tracer is then chosen for its half-life that needs to be long enough for the tracer to make its way to the region of interest but short enough so that the patient has a minimal dose of radioactive material once the whole imaging process has been completed. The most commonly used radioactive isotope is Fluorine-18 that has a half-life of 109.8 minutes.

The isotope is then attached to a molecule through a chemical reaction to form what is called a radionuclide.

The most used radionuclide in PET imaging is fluorodeoxyglucose (FDG) as it is a form of sugar. Sugar is known to be absorbed in high quantities by cancerous cells. The radioactive decay then takes place in these cells emitting positrons. In turn, the positrons annihilate with nearby electrons emitting two back-to-back 511 keV photons. Scintillator detectors are placed in a ring around the patient to collect these photons. A line can be drawn for each pair of photons detected and

then the intersection of all lines indicates the cancerous region of the patient.

New developments [27, 28] in PET imaging include improvements on time-of-flight detectors to shorten the lines into segments. Based on the time of arrival difference of the two photons originating from the same positron, a more precise image can be recreated.

The Gamma Knife device was first developped in Sweden in the 1960s by a team led by neurosurgeon Lars Leskell and physicists Kurt Liden and Borje Larsson [29, 30]. The idea was to change the way patients are operated on when suffering from various brain conditions. The traditional method of cutting up the skull to perform open surgery was not always desirable. As a replacement, radiation is a non-intrusive means of operation that can destroy tumours, even those inaccessible by a plain knife.

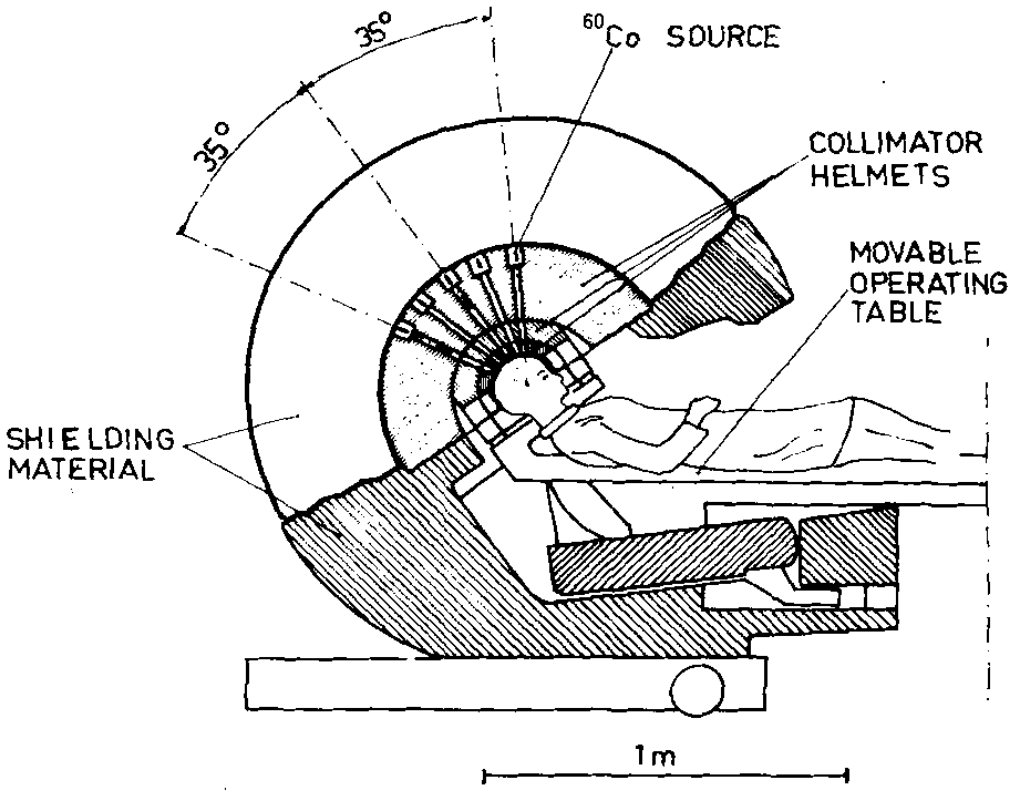

Figure 1.7: Schematic drawing of a section of a Gamma Knife device where five of the ^{60}Co sources are shown. Reprinted from [30]

The way this device works is a multitude of radioactive sources are placed around the patient's head, as shown in Figure 1.7. Cobalt-60 was chosen as it emits gamma-rays at 1.17 and 1.33 MeV which present a low linear energy transfer [31], that is the energy deposited as a function of the distance travelled in tissue is low enough that the radiation can reach the targeted area as well as affecting the healthy parts as little as possible. Cobalt-60 was also chosen as its half-life of 5.27 years means multiple patients can be treated without the need to acquire new radioactive material.

The first device had 179 of these sources, with all the subsequent ones also around the 200 mark. Each source emits a thin line of radiation such that they intersect in the region of the brain that needs to be destroyed. The dose from each source is calculated so that the superposition is sufficient when applied to the tumour while minimising the radiation perceived by the rest of the healthy brain.

A similar technology developed in parallel to the Gamma Knife uses a linear accelerator to fire electrons on to a tungsten target as its source of gamma-rays. Instead of having multiple sources, the gantry of the linac rotates around the head of the patient who can also be moved thanks to a mobile operating table [32–34].

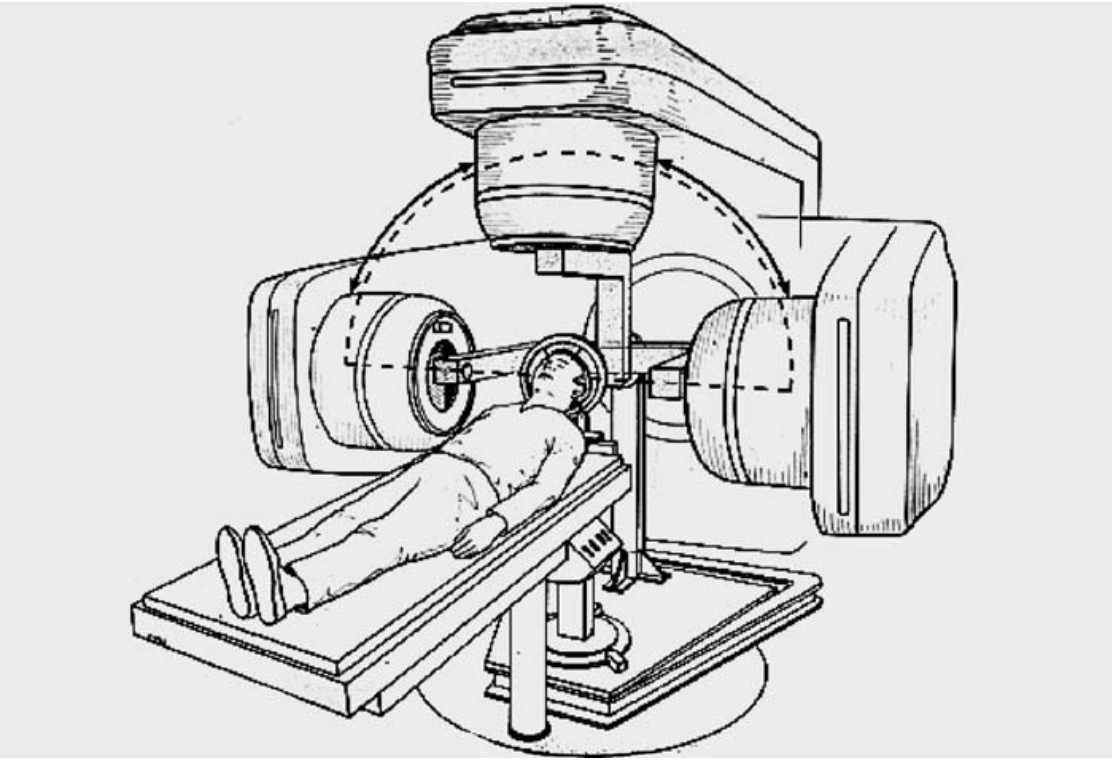

Figure 1.8: Diagram of a rotating radiosurgery linac with a patient lying on a mobile operating table. Reprinted from [32]

1.6 Chapter summary

In this chapter, we discussed the discovery and nature of gamma-rays, the higher energy band of the electromagnetic spectrum. We then detailed the various existing detection systems. The X-ray film is the oldest of these and the one used to discover gamma-rays. It is easy of use and convenient for imaging purposes. Silver halide crystals in the film absorb the energy of incoming photons. After being developed, the film reveals where the gamma-rays passed. The gas-filled detectors use the fact that gamma-rays can ionise gases. This results in free electrons being collected by an electrode in the enclosed chamber. Scintillators use fluorescence to convert gamma-rays into visible light, that can then be studied using photo-multiplier tubes. The last type of detector presented is the semiconductor where the gamma-rays deposit energy in the material through a physical interaction, which is transferred to the electrons it contains. They then drift to electrodes which read out the signal.

Some concrete uses of gamma-rays were presented. NRF uses gamma-rays to excite the nuclei in a sample. When they relax, they emit photons at given discrete levels that allow an identification of the elemental components of the sample. This has promising prospects in the military field when dealing with nuclear materials. Finally, gamma-rays are used in the medical world both for imaging with PET and therapy with the Gamma-knife.

Chapter 2

Gamma Ray Sources

2.1 Radioactive sources

As explained in Chapter 1, gamma-rays were first discovered by Villard while he was studying radioactive radium. Radioactive material use as a source of gammas is still widespread. Some use cases that can be pointed out are the gamma knife radiotherapy machine explained in detail in Section 1.5.2, industrial radiography for material inspection [9] using either photographic film to detect manufacturing defects, as seen in Section 1.4.1, or using a fluorescent screen and camera as seen in Figure 2.1.

Testing photon sensitivity of neutron detectors [35] is another example that we can give. The authors set out a clear goal of finding a viable alternative to ^{3}He detectors due to the dwindling availability of ^{3}He. One of the main preoccupations is to find a technology that has a high sensitivity to neutrons and as low as possible to gamma-rays. To this effect, Cobalt-60 and Iridium-192, which are two of the most commonly used gamma radioisotopes, served as sources to measure gamma efficiency.

Finally, many undergraduate physics students will encounter radioactive sources during the course of their laboratory experiments such as the one described in [36]. Here, the goal is to determine the rest-mass of the electron using the Compton scattering principle. Gamma rays with a known energy E_i are targeted onto an aluminium slab. By measuring the energy of the scattered rays E_f, the rest-mass of the electron can be obtained using the following formula:

$$m_e c^2 = 2\frac{E_i \times E_f}{E_i - E_f} \tag{2.1}$$

The obtention of such radioactive sources is usually regulated by national bodies such as the Autorité de Sûreté Nucléaire (ASN) [37] in France to ensure

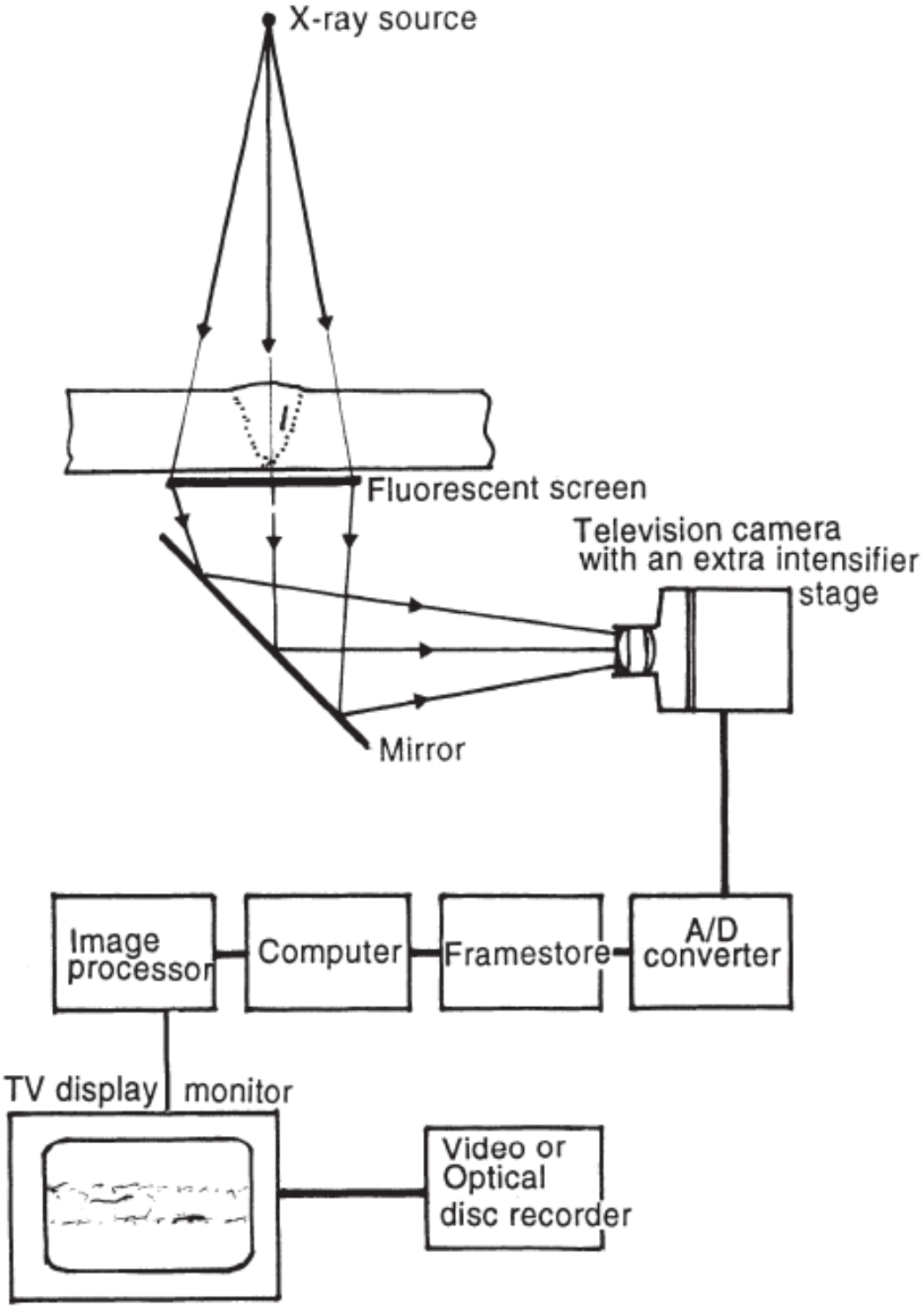

Figure 2.1: Radiography equipment diagram. Reprinted from [9]

the safety of its users and of the general public. They are always provided as sealed sources where the radioactive material is in an enclosed container to avoid any contamination during handling.

2.2 Compton Interaction Machines

2.2.1 Compton Interaction

The Compton interaction named after Arthur Compton [38] is the inelastic scattering of a photon by an electron. He observed a change in wavelength $\Delta\lambda$, now called Compton shift, in the photon before and after interaction corresponding to the energy absorbed by the electron, given by the following equation:

$$\Delta\lambda = \lambda' - \lambda = \frac{h}{m_e c}(1 - \cos\theta) \tag{2.2}$$

where λ and λ' are the initial and final photon wavelengths and θ is the photon scattering angle.

He was awarded a Nobel prize for this discovery as it was an important step in the understanding of the particle-wave dual nature of photons.

The 4-momentum is conserved during the Compton interaction such that:

$$p + k = p' + k' \tag{2.3}$$

where p and k are the 4-momentums of the electron and the photon before interaction, p' and k' the ones after.

In the frame of reference where the incoming electron is at rest, the differential cross-section of the interaction of a polarised photon with an unpolarised electron is given by the following formula [39, 40]:

$$d\sigma = \frac{r_e^2}{4}\left(\frac{\omega'}{\omega}\right)^2 do'\{F_0 + F_3(\xi_3 + \xi_3') + F_{11}\xi_1\xi_1' + F_{22}\xi_2\xi_2' + F_{33}\xi_3\xi_3'\} \tag{2.4}$$

with

$$do' = \sin\theta d\theta d\phi \tag{2.5}$$

$$F_0 = \frac{\omega}{\omega'} + \frac{\omega'}{\omega} - \sin^2\theta \tag{2.6}$$

$$F_3 = \sin^2\theta \tag{2.7}$$

$$F_{11} = 2\cos\theta \tag{2.8}$$

$$F_{22} = (\frac{\omega}{\omega'} + \frac{\omega'}{\omega}) \cos\theta \tag{2.9}$$

$$F_{33} = 1 + \cos^2\theta \tag{2.10}$$

where ω and ω' represent the energy of the initial and scattered photon respectively, r_e is the classical electron radius, θ the scattering angle, ϕ the azimuthal angle of the scattered photon, ξ_{1-3} are the Stokes parameters [41], that describe the polarisation state of the photons along the xyz axes.

2.2.2 Overview of existing machines

The idea of applying the theory explained in the previous section to create beams of high energy photons came in 1963. In this same year, an article by Milburn [42] and another by Arutyunian and Tumanian [43] suggest coupling a ruby laser of wavelength 694.3 nm with a synchrotron with electrons circulating around the GeV range. This was in line with recent technological breakthroughs of that time such as the first working electron synchrotron [44] and the first working laser [45] that employed ruby as amplification medium.

Few GeV photon beams were measured at the Stanford Linear Accelerator Centre (SLAC) [46] in 1969 before many dedicated facilities started being built around the world.

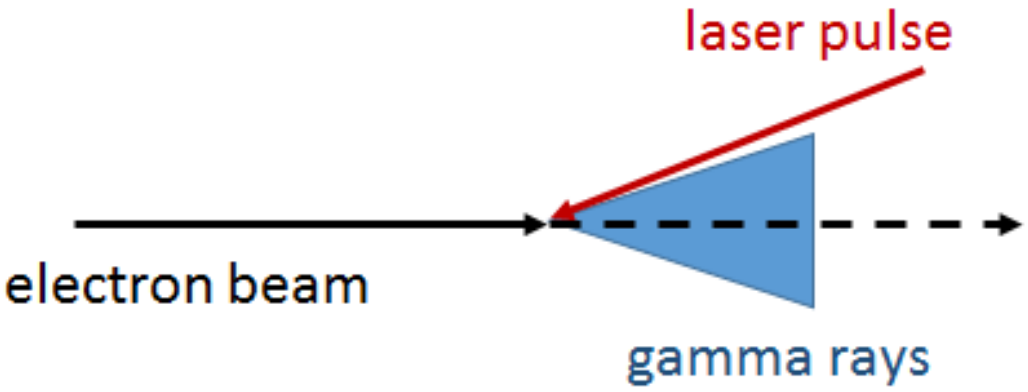

Figure 2.2: Schematic drawing of the Inverse Compton Interaction between an electron beam and a laser pulse.

Nowadays, many different Compton Interaction Sources exist presenting unique specificities. The electron accelerator can be of the linear or circular type. The laser can be delivered directly or amplified in a Fabry-Pérot cavity to increase the resulting photon flux. The underlying process stays nevertheless the same:

producing gamma-rays by focusing a laser and an electron beam on top of each other as seen schematically in Figure 2.2. Three examples of interest to this thesis are described in the following sections: HIγS and newSubaru where experiments were conducted in anticipation of the installation of the detection system for the project I was working on, ELI-NP.

2.2.3 HIγS

The High Intensity gamma Source (HIγS) [47] is a research facility situated at Duke University, in the United States. Electrons are generated on a photocathode, accelerated and then injected in a booster-synchrotron where they are accelerated to the nominal energy needed in the storage ring with continuous top-up. The ring is structured like a racetrack with two parallel straight sections. In one of these sections, a set of wigglers serves to produce Free Electron Laser (FEL) radiation.

A wiggler is an arrangement of multiple dipole magnets, as shown in Figure 2.3 separated by a period length λ_u (=0.1m at HIγS) that make the charged electron undulate with a frequency ω in the laboratory frame given by the equation [48] :

$$\omega = \frac{2\pi\gamma\beta c}{\lambda_u} \tag{2.11}$$

with γ and β relativity constants.

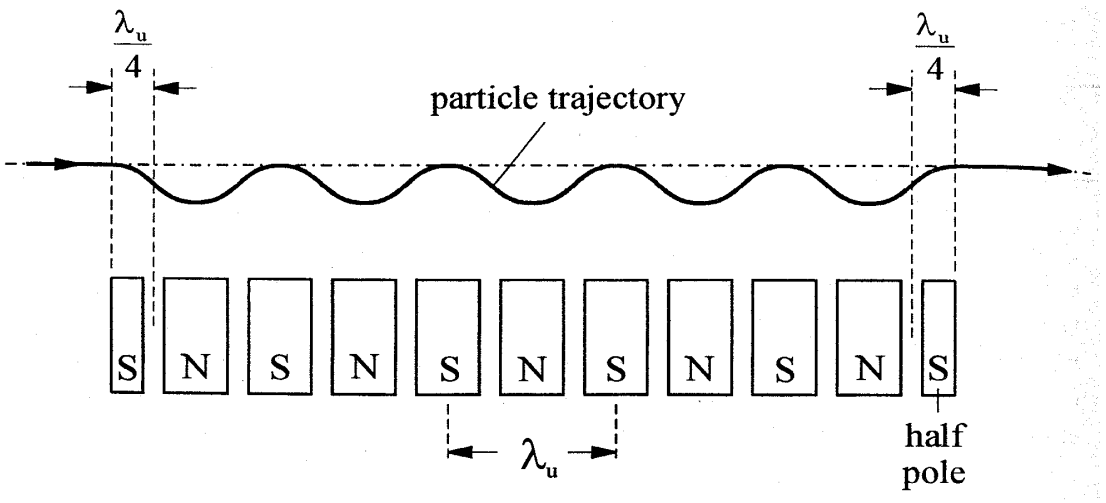

Figure 2.3: Schematic drawing of a wiggler with the successive North (N) and South (S) magnets separated by half a period length $\frac{\lambda_u}{2}$. Reprinted from [48]

.

The wavelength of the produced radiation λ_r along the axis of propagation of the electrons is given by:

$$\lambda_r = \frac{\lambda_u}{2\gamma^2}(1 + \frac{K^2}{2}) \tag{2.12}$$

with the wiggler parameter K given by:

$$K = \frac{\lambda_u e \tilde{B}}{2\pi m_e c} \tag{2.13}$$

where $\tilde{B}$ is the peak value along the beam axis given by:

$$\tilde{B} = \frac{B_0}{\cosh(\frac{\pi g}{\lambda_u})} \tag{2.14}$$

with g the separation between the two poles and B_0 is the magnetic field value in the middle of the poletip, as defined in Figure 2.4.

An optical resonating cavity is created by putting two mirrors at the extremities of the straight section separated by 53.73 m, which is half the circumference of the storage ring. At each pass, more photons are produced through stimulated emission with electron beam being used as lasing material. This is the principle of the Free Electron Laser which allows a high tunability of the laser wavelength compared to traditional lasers which are constrained by the atomic transitions in the amplification medium. A drawing representing the elements comprising the HIγS facility is shown in Figure 2.5.

The HIγS facility offers three main operating modes. The single-bunch mode is the standard FEL mechanism described above. In the two-bunch beam mode, two beams of electrons are circulating in the ring. The first one produces the FEL radiation and the second one serves as target for the Compton interaction to generate gamma-rays. There is also a third mode of operation for continuous emission of photons from the wigglers called multi-bunch. Other custom operating modes can be developed according to experimental needs.

The two-bunch operation is the one that interests us here. The gamma-rays produced are highly tunable with an energy range of 1 to 100 MeV with an FWHM energy spread going down to 0.8%. The polarisation can be linear or circular. This is given by the polarisation of the FEL beam which is controlled by two different sets of wigglers depending on the desired polarity. The pulse length is sub-ns with a flux ranging between 10^6 and 10^9 at a repetition rate of 5.58 MHz.

The upgrade of this facility called HIγS2 [49] includes a Fabry-Pérot resonator in which circulates a laser beam. This will allow the laser power to be much higher than with the FEL thus increasing the flux of gamma-rays produced by two orders of magnitude and allowing a much better control of the polarisation of the gamma beam.

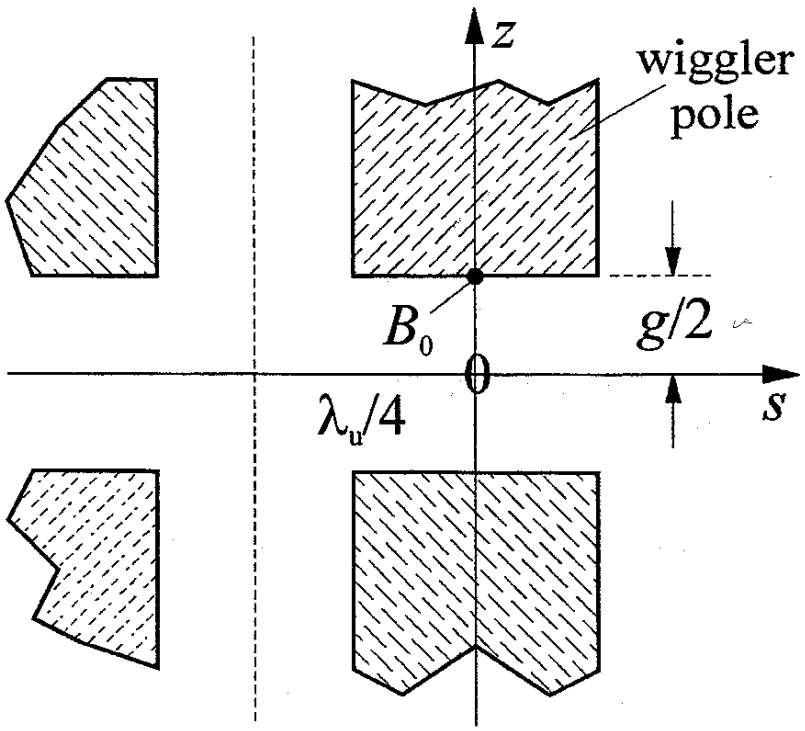

Figure 2.4: Schematic drawing detailing an individual magnet of a wiggler. g is the separation between the two poles. B_0 is the magnetic field value in the middle of the poletip. Reprinted from [48].

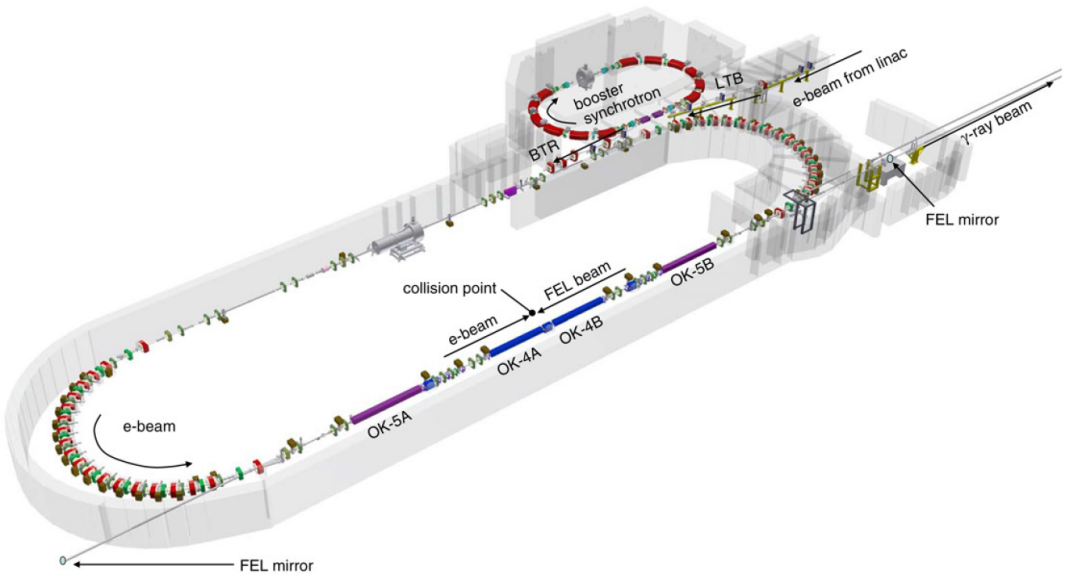

Figure 2.5: Schematic layout of the accelerator and FEL at HIγS. Reprinted from [47]

2.2.4 newSubaru

The newSubaru facility in Japan [50] is an electron storage ring with a circumference of 119 m and two long straight sections of 14 m. On one of these, a set of mirrors brings the laser light to collide head-on with the electrons. A detail of this is shown in Figure 2.7, with the full layout of the ring and beamlines presented in Figure 2.6. Electrons circulate at energies between 0.5 and 1.5 GeV at a repetition rate of 500 MHz. The total current is typically 300 mA in continuous top-up mode where electron bunches are injected into the storage ring to have a constant current. The second mode is without top-up where electrons are injected at the beginning of a run and are then left to decay as they go around the ring. The laser is an industrial Nd:YVO_4 laser at 1064 nm with a pulse width of 60 ns, a time in which 30 electron bunches pass through. The photon beam thus seen by the user is also spread over 60 ns with a flux proportional to the power given by the Gaussian profile of the laser. Other experimental rooms are located around the storage ring to make use of synchrotron radiation and on the second straight section, an undulator is installed to produce FEL radiation.

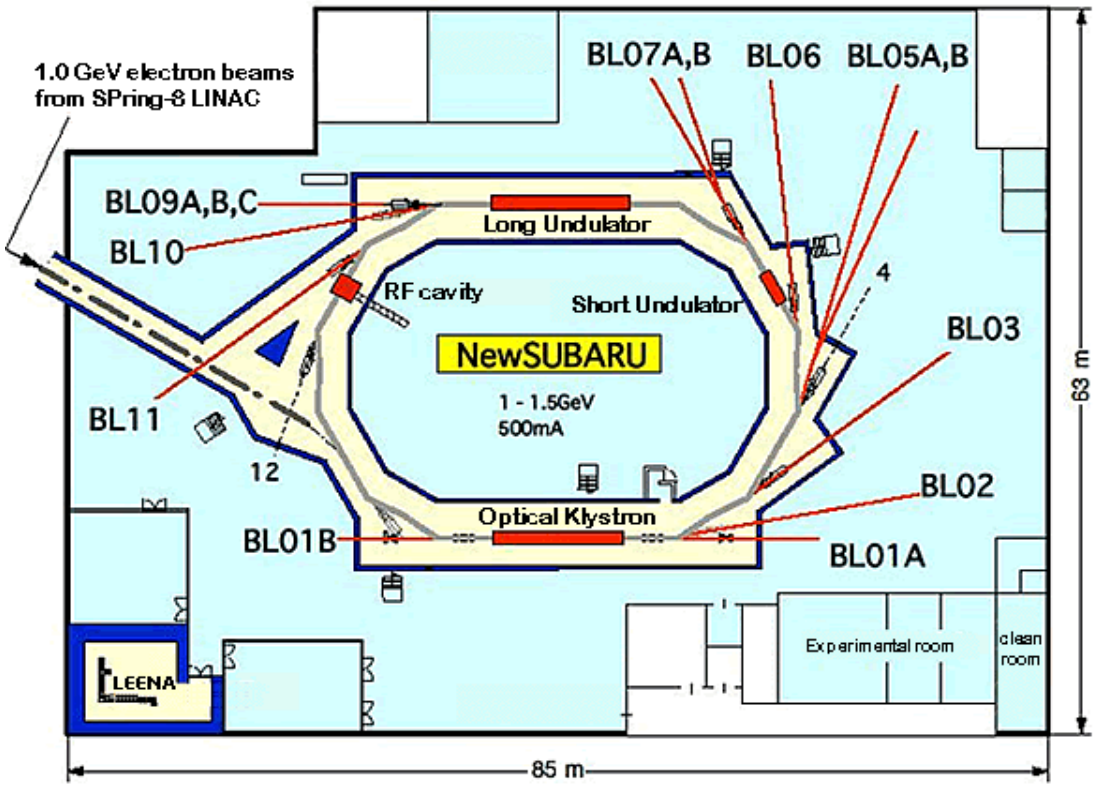

Figure 2.6: Layout of the newSubaru research facility, its storage ring and various beamlines. Reprinted from [51]

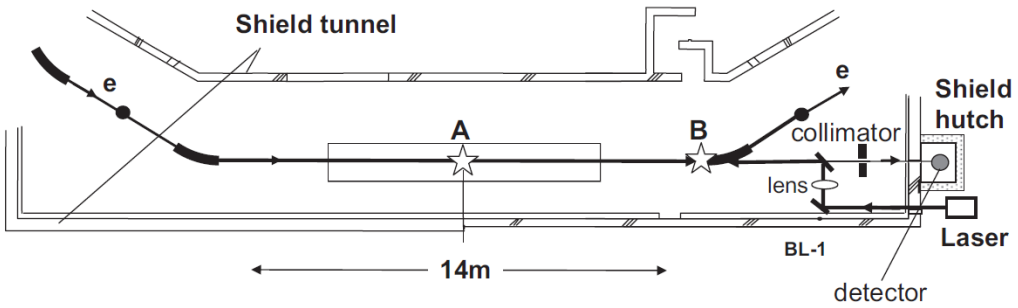

Figure 2.7: Drawing of the laser-electron interaction area at the newSubaru research facility, also known as beamline BL01A. Reprinted from [50]

2.3 Chapter summary

In this chapter, we looked at gamma sources. Some radioactive elements disintegrate by emitting high energy photons. A common example is Cobalt-60, that is used in the Gamma-knife to destroy brain tumors.

The man-made Compton interaction machines use an accelerator to collide electrons with photons from a laser. Through this interaction, the photons gain energy and go from the visible to the gamma spectrum. HIγS presents the particularity of using a storage ring to accelerate the electrons but also to produce FEL radiation that interacts itself with the electrons. NewSubaru is the second machine presented. It boasts a very stable electron beam circulating in a storage ring. An industrial laser, tunable in power, is used for the interaction. In the next chapter, the ELI-NP machine which offered the framework for this thesis is presented.

Chapter 3

ELI-NP

3.1 ELI Project

The Extreme Light Infrastructure (ELI) project [52] is a European project on laser technologies based on three pillars in three different countries. Its ultimate goal is to combine the various technological and scientific breakthroughs that these three pillars will enable to generate 200 PW pulses within the next decades, according to the ELI whitebook [52]. We will be focusing on ELI-NP situated in Romania in this thesis but first the other two pillars are described.

3.1.1 ELI ALPS

Extreme Light Infrastructure Attosecond Light Pulse Source (ELI-ALPS) [53] is a research facility currently being built in Szeged, Hungary. Its main focus is centred on generating attosecond pulses with various parameters using four different laser primary sources, one 15W mid-infra-red and three 100W near infra-red lasers. Two main research axes explored are going beyond the current state-of-the-art repetition rate and pulse energy of attosecond beams.

To generate these attosecond beams, the Gas High-order Harmonics Generation (GHHG) [54] principle is used. A laser is shone into a noble gas container. This ionises an atom. The resulting free electron is moved back to its parent atom by the kinetic energy of the laser before having time to move away. It is then reabsorbed, emitting a photon through the process with a harmonic frequency.

One of the more ambitious goals of ELI-ALPS is to generate attosecond pulses using the new Surface High-order Harmonics Generation (SHHG) method. Here, instead of using a noble gas as the harmonic generation medium, an optically polished rotating glass target is used as a plasma mirror [55]. A waveform-controlled few-cycle near infra-red laser pulse is focused onto it. The intense laser electric field ionizes the surface atoms, creating a plasma mirror,

Beamline	L1	L2	L3	L4
Peak power	7 TW	0.1 PW	$\geq$1 PW	10 PW
Energy in pulse	100 mJ	1.5 J	$\geq$30 J	$\geq$1.5kJ
Pulse duration	<15 fs	<15 fs	$\leq$30 fs	$\leq$150 fs
Repetition rate	1 kHz	10 Hz	10 Hz	<0.1 Hz

Table 3.1: Parameters of the four lasers at ELI-Beamlines

which reflects the laser light. An attosecond pulse train is non-linearly generated in the direction of the reflected laser beam through two processes - coherent wake emission and relativistic oscillating mirror - depending on the laser intensity [53]. For intensities between 10^{14} and 10^{18} W cm$^{-2}\mu$m^2, coherent wake emission [56] takes place. The surface electrons on the mirror are pulled by the electric field of the laser and then pulled back by the plasma, making them oscillate at a harmonic frequency of the driving laser. This electron oscillation radiates short pulse ultra-violet light. At intensities above 10^{18} W cm$^{-2}\mu$m^2, the oscillation of the surface electrons introduces a periodic Doppler shift in the reflected light, that leads to phase locked harmonics also called relativistic oscillating mirror harmonics that present attosecond features.

Before the focusing parabola, the laser goes through a moveable prism that introduces wavefront rotation. This is done so that the generated beam gets separated spatially into single isolated attosecond pulses. A diagram showing the SHHG process is presented in Figure 3.1.

Some research experiments utilising these attosecond beams have been announced [53]. This will involve the installation of specialised equipment on site. Among them, we can site a photoelectron emission microscope for material and surface studies or a cold target recoil ion momentum spectrometer and velocity map imaging spectrometers for fundamental research in atomic, molecular and optical science with an emphasis on photoreactions.

3.1.2 ELI Beamlines

The ELI-Beamlines [57] project is currently under construction in Dolní Břežany, Czech Republic. This centre is a more conventional laser facility. It will house four different lasers, L1, L2, L3 and L4 that each has its specificities and applications. The parameters of the lasers are shown in Table 3.1 and a block diagram of the whole system is presented in Figure 3.2.

As a user facility, ELI-Beamlines can boast an incredible number of applications as lasers have reached more and more scientific areas over the past decades. One example we can start with is laser-plasma acceleration [58]. Its

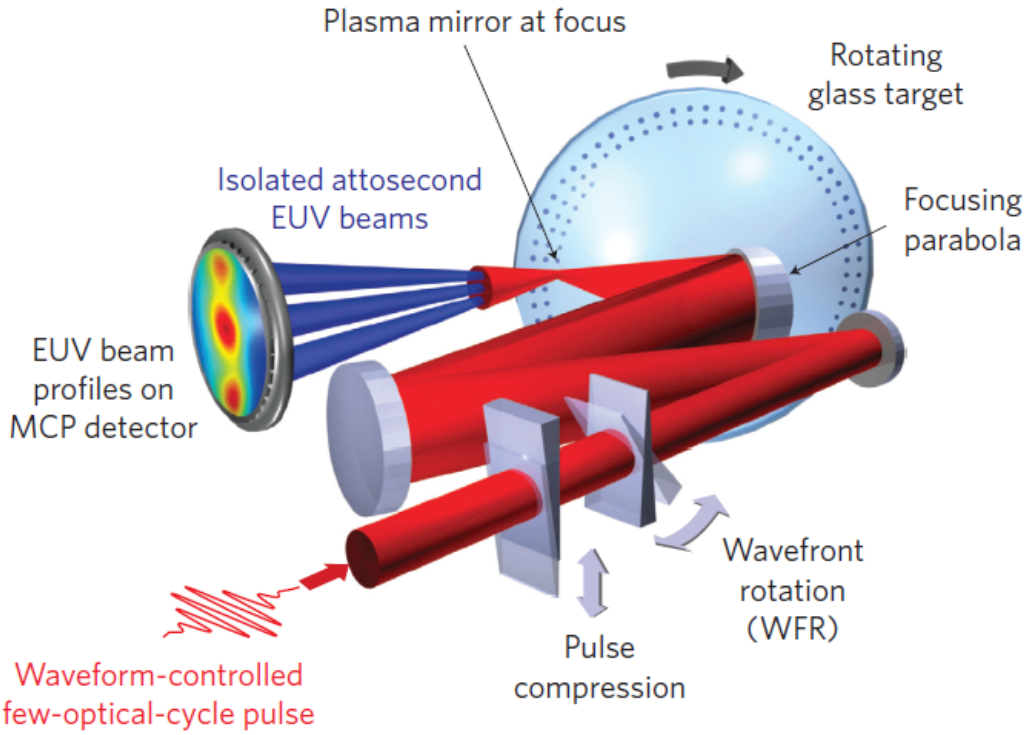

Figure 3.1: Schematic of the SHHG process. An infrared laser goes through a wavefront rotation prism before being focused onto a rotating mirror. In this experiment, the attosecond beamlets are directly imaged onto a microchannel plate (MCP) detector. This gives the spatial beam profile of the extreme ultra-violet (EUV) radiation. Reprinted from [55]

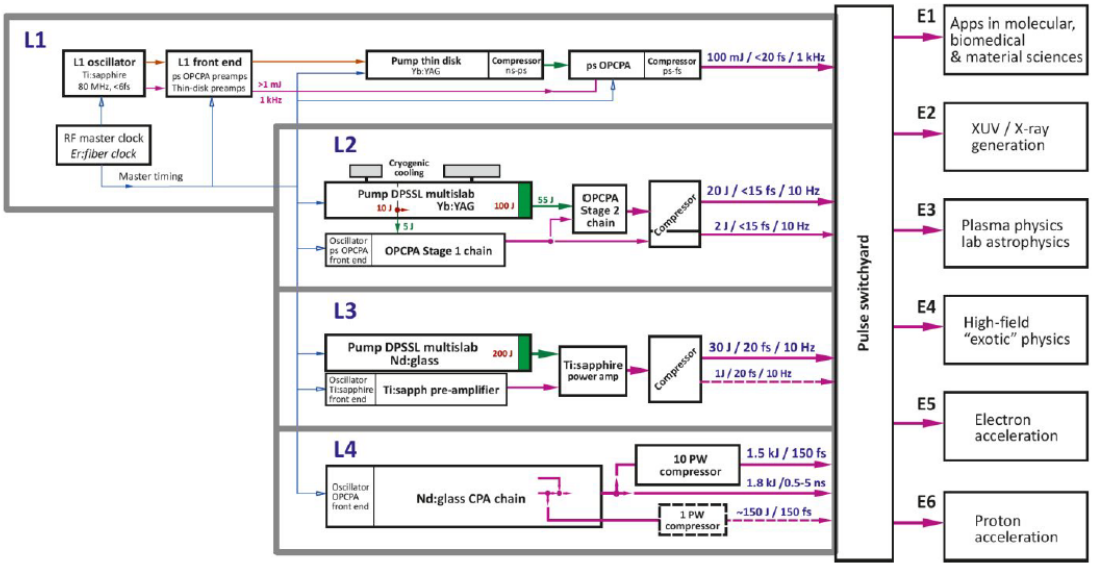

Figure 3.2: Block diagram of the laser systems at ELI-Beamlines. Reprinted from [57]

goal is to render accelerators much more compact. Indeed nowadays, accelerator size has been on an upward trend with the currently longest one, the LHC, 27 km in circumference. Plans for a next-generation accelerator, the Future Circular Collider (FCC) [59], foresee a ring 100 km in circumference to accelerate electrons. To some, this seems excessive and a miniaturisation solution could lie in laser-plasma accelerators, although the performance of such accelerators in terms, for example, of emittance [60] are still far below traditional accelerators and it is imperative for this to be solved before they can become a viable alternative. Other foreseen uses for these laser beams are pump-probe experiments where two pulses separated by a short time delay are sent on the same sample. This is done typically in chemistry and biology where the first pulse leads to a reaction in the target and the second allows the extraction of information, such as reaction time. Here we can point to the extended work of Ahmed Zewail [61], nicknamed the "father of femtochemistry" and who was awarded the Nobel Prize in Chemistry in 1999.

3.2 ELI-NP Gamma Beam Source

The Extreme Light Infrastructure-Nuclear Physics Gamma Beam System (ELI-NP GBS) [62] is a facility currently in its installation phase in Măgurele, Romania. It is one of the three pillars of the Extreme Light Infrastructure European project.

Parameter	**Value**
Photon energy	$0.2 - 19.5$ MeV
Spectral density	$0.8 - 4 \times 10^4$ photons/s . eV
Bandwidth (rms)	$\leq 0.5\%$
Number of photons per shot (within FWHM)	$\leq 2.6 \times 10^5$
Number of photons per second (within FWHM)	$\leq 8.3 \times 10^8$
Source rms size	10 - 30 µm
Source rms divergence	25 - 200 µrad
Peak brillance ($N_{photons}/s.mm^2.mrad^2.0.1\%$)	$10^{20} - 10^{23}$
Linear polarisation	$> 99\%$
Pulse length (rms)	0.7 - 1.5 ps
Pulse repetition rate	62.09 MHz
Number of pulses per train	32
Train repetition rate	100 Hz

Table 3.2: Specifications of the gamma beam source at ELI-NP

Its goal is to develop a high-end nuclear research facility with a gamma-beam source of extremely narrow energy range of 0.5%.

It is constituted of an electron linear accelerator that branches in two to have two possible interaction points, one at low energy with photons produced between 0.2 and 5 MeV and one reaching higher energies up to 20 MeV. The electrons are produced in 32 bunches at 62 MHz frequency by shining a high-power laser on a photocathode. The accelerator branches into two lines leading to two interaction points, one at low energy between 80 and 320 MeV and one at higher energy going up to 720 MeV. There, a laser pulse interacts with the 32 consecutive electron bunches. This is done by making it circulate in an optical system.

This machine is built by a European consortium named EuroGammaS, that was put together to answer a call for bids of the Horia Hulubei National Institute of Physics and Nuclear Engineering, in Romania. The *Centre national de la recherche scientifique, Institut national de physique nucléaire et de physique des particules* (CNRS/IN2P3) is a member and tasked with developing most of the optical components. I prepared the work presented in this manuscript at the *Laboratoire de l'Accélérateur Linéaire*. The *Istituto Nazionale di Fisica Nucleare* (INFN) in Italy was tasked with building the accelerator. Many other European companies and research institutions helped along the way in diverse areas such as the laser systems, infrastructure, network, control systems, mechanical parts, vacuum systems or guidance. A full list of the EuroGammaS members can be found in the Technical Design Report [62] that details all the parts of the machine aiming for the specifications given in Table 3.2.

3.2.1 Photocathode laser and electron production

Let's first look at how the electron beam is produced. This is done at ELI-NP with a 1.6 cell photocathode RF gun similar to the one developed by the BNL/SLAC/UCLA [63]. The photocathode quantum efficiency QE is the ratio of the number of emitted electrons to the number of incident photons. It is given by [64] :

$$QE = \frac{n_e}{n_p} = \frac{h\nu Q}{E_{laser} q_e} \tag{3.1}$$

where $h\nu$ is the photon energy, Q is the charge released by the cathode, E_{laser} is the laser energy and q_e is the electron charge. The photocathode used at ELI-NP will be made of copper, which has a QE of the order of 10^{-5} to 10^{-4} [65] and a work function of 4.7 eV. This means the wavelength of the laser needs to be below 266 nm for the photons to strip electrons from the copper surface. For this purpose, initially a tunable Titanium-Sapphire laser is used at 780 nm. To reach the required laser energy to produce the nominal electron beams, the Chirped Pulse Amplification (CPA) technique [66] is used. The laser pulse is stretched first with a diffraction grating, in a manner similar to the one described in Ref. [67]. Afterwards, it is sent through a regenerative amplifier comprised of two Pockels cells. One to seed the pulse into the cavity and one to dump it at the maximum energy close to 1 mJ at 100 Hz repetition rate. This repetition rate is then kept throughout the optical chain. The laser pulse then goes through a series of multipass amplifiers: crystals pumped by their own external laser and through which the pulse passes multiple times to be amplified up to a few hundreds of millijoules. The lasers used for pumping are two types of industrial lasers, namely the Centurion from Quantel and the Nano-TRL-250-100. Both are Nd:YAG lasers at 532 nm with 100 Hz repetition rate. The first one is based on diode pumping and goes up to 20 mJ, the second one on flash-light pumping at 130 mJ. They appear in green in Figure 3.3 and photos of them are shown in Figure 3.4.

Another important module through which the pulse goes is the multipulse cavity to get 32 pulses spaced by T = 16.108 ns. This is done in multiple steps.

1. The pulse is divided into two pulses with the use of a beamsplitter and their time separation is set to T with a delay line.

2. These two pulses are injected through a dichroic mirror into the vacuum-pumped cavity that has a round trip period of 2T.

3. The pulses are trapped inside the cavity actively with the use of a Pockels cell.

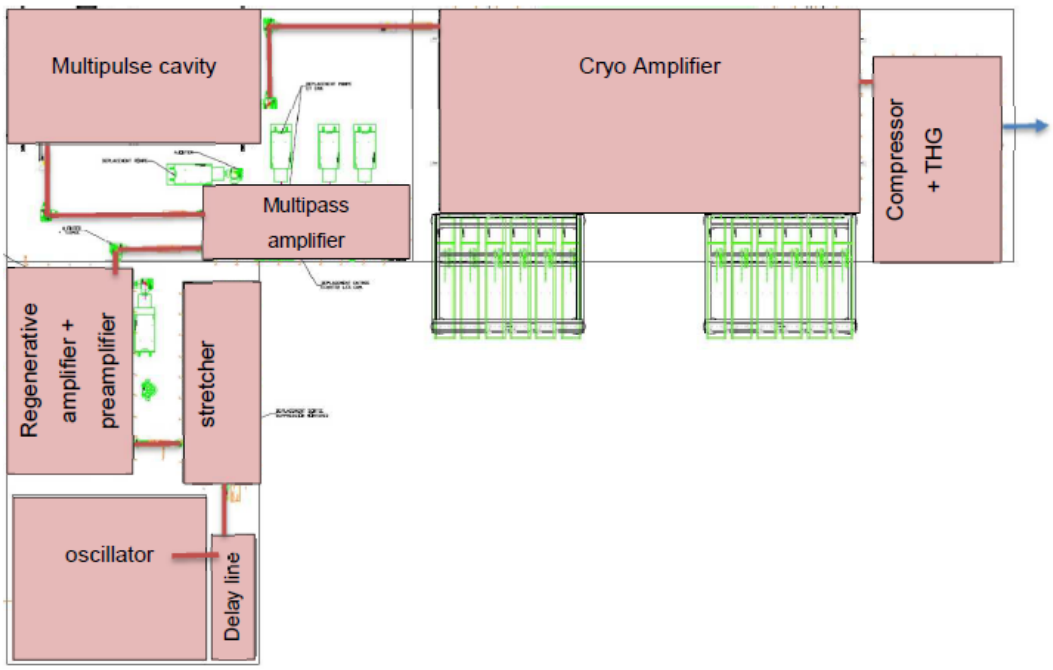

Figure 3.3: Schematic of the components of the photocathode laser of ELI-NP.

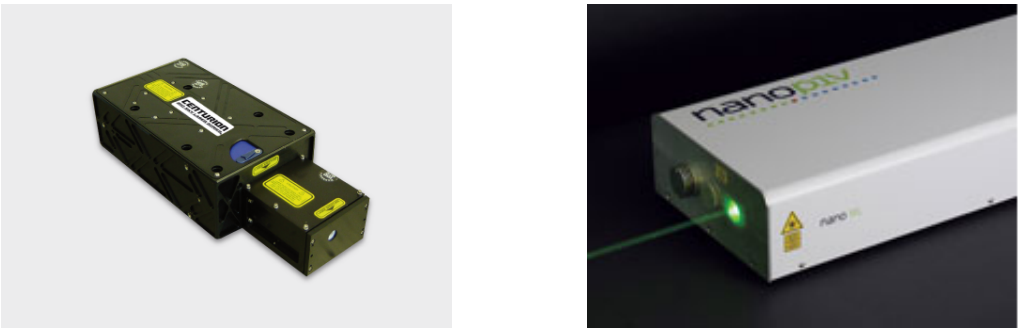

Figure 3.4: Photos of the two types of pumping lasers used in the amplifying chain of the photocathode laser. On the left, the Centurion by Quantel and on the right the Nano-TRL by Litron. The photos were taken from the respective manufacturers' websites.

Parameter	**Value**
Pulse energy	300 μJ
Wavelength	266 nm
Pulse width	8.5 ps
Pulse repetition rate	62.09 MHz
Number of pulses per train	32
Train repetition rate	100 Hz

Table 3.3: Parameters of the photocathode laser at ELI-NP

4. The losses of the cavity are collected behind one mirror that has a higher transmission coefficient than the others. This is where the train of 32 pulses is generated.

5. A fast 32-channel Pockels cell allows the energy modulation of each pulse as all 32 must be within 5%, after the last amplification stage.

6. The pulse train is then fed into the final amplifying stage, which is cryogenically cooled.

Finally the pulses are compressed back to a few ps length individually by going through two gratings. They also go through a set of nonlinear crystals that comprise the Third Harmonic Generator (THG) [68] so that the light wavelength is divided by three to 266 nm, necessary to strip electrons from the cathode. The pulses are now ready to be delivered to the photocathode, several meters away. This is done in vacuum-pumped tubes with a minimum number of mirrors to limit wave-front deformation and other non-linear effects. A drawing of the photocathode laser transport system is shown in Figure 3.5. A summary of the parameters of the laser when it interacts with the photocathode are given in the Table 3.3.

An important step to ensure the production of gamma-rays for the users is the synchronisation of all the systems between themselves. For the photocathode laser, an optical bench was developed with two-photon photodiodes. This will be covered in Chapter 4.

3.2.2 Accelerator

The team working on developing the accelerator was also involved in the construction of SPARC in Frascati, Italy. Understandably, the two accelerators present similar elements. After the electron bunches are generated, they are injected into a first linac composed of S-band accelerating structures, coupled to

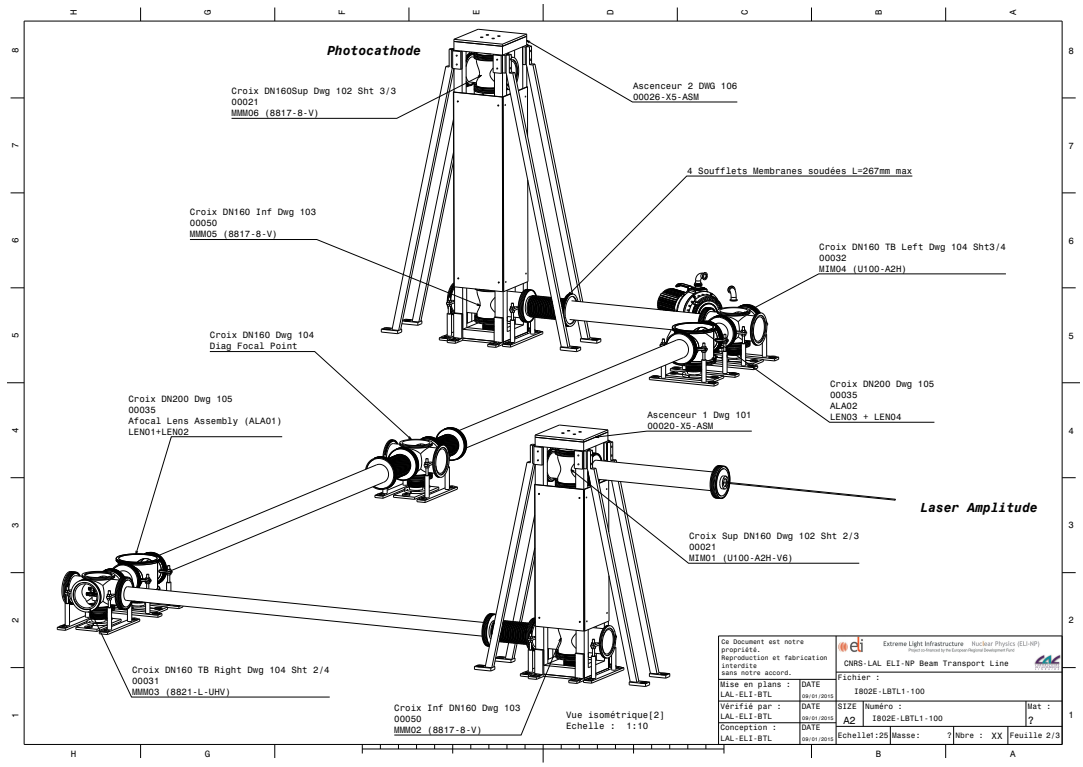

Figure 3.5: Drawing of the photocathode laser transport system.

Parameter	Value
Pulse energy	200 mJ
Wavelength	515 nm
Spectral width	0.1 %
Pulse width	1.5 ps
Repetition rate	100 Hz

Table 3.4: Parameters of the laser at the low energy interaction point. The high energy interaction point presents exactly the same parameters except the energy which is doubled.

RF waveguides. The main linac is then composed of 3 m long C-band accelerating structures, operated at 2.856 GHz. One example is shown in Figure 3.7. A diagram showing the entire accelerator is presented in Figure 3.6.

3.2.3 Interaction laser

The interaction laser starts with a Yb:YAG oscillator at 1030 nm. Then, an amplifying chain based on CPA similar to the photocathode laser lets it reach the desired energy. The pulse is first stretched. It goes through three amplifiers, a regenerative amplifier, a booster and a multipass power amplifier to go from 1 nJ to 600 mJ. It is then recompressed before being reflected on a deformable mirror that corrects wavefront distortions due to amplification. Finally, the laser pulse goes through a Lithium triborate (LBO) crystal to halve the wavelength to 515 nm. It can then be transported to the interaction point in vacuum tubes using two telescopes with a magnifying power of 1 so that the spot size is the same at the beginning and the end of the transport line. Each telescope is made of two parabolic mirrors with each mirror put in a three-mirror system as seen in Figure 3.9. This is to facilitate alignment procedures. One has to be careful to avoid non-linear effects due to the laser going through matter. For this reason, mirrors are preferred to lenses. Indeed, the only material the laser pulses go through is the isolation window that serves to transition from air to vacuum. The high energy interaction point needs two of the lasers described above to reach double the energy. The architecture is the same except the two lasers get combined in the frequency doubling LBO crystal.

A block diagram summarises the elements constituting the interaction laser in Figure 3.8 and its specifications are given in Table 3.4.

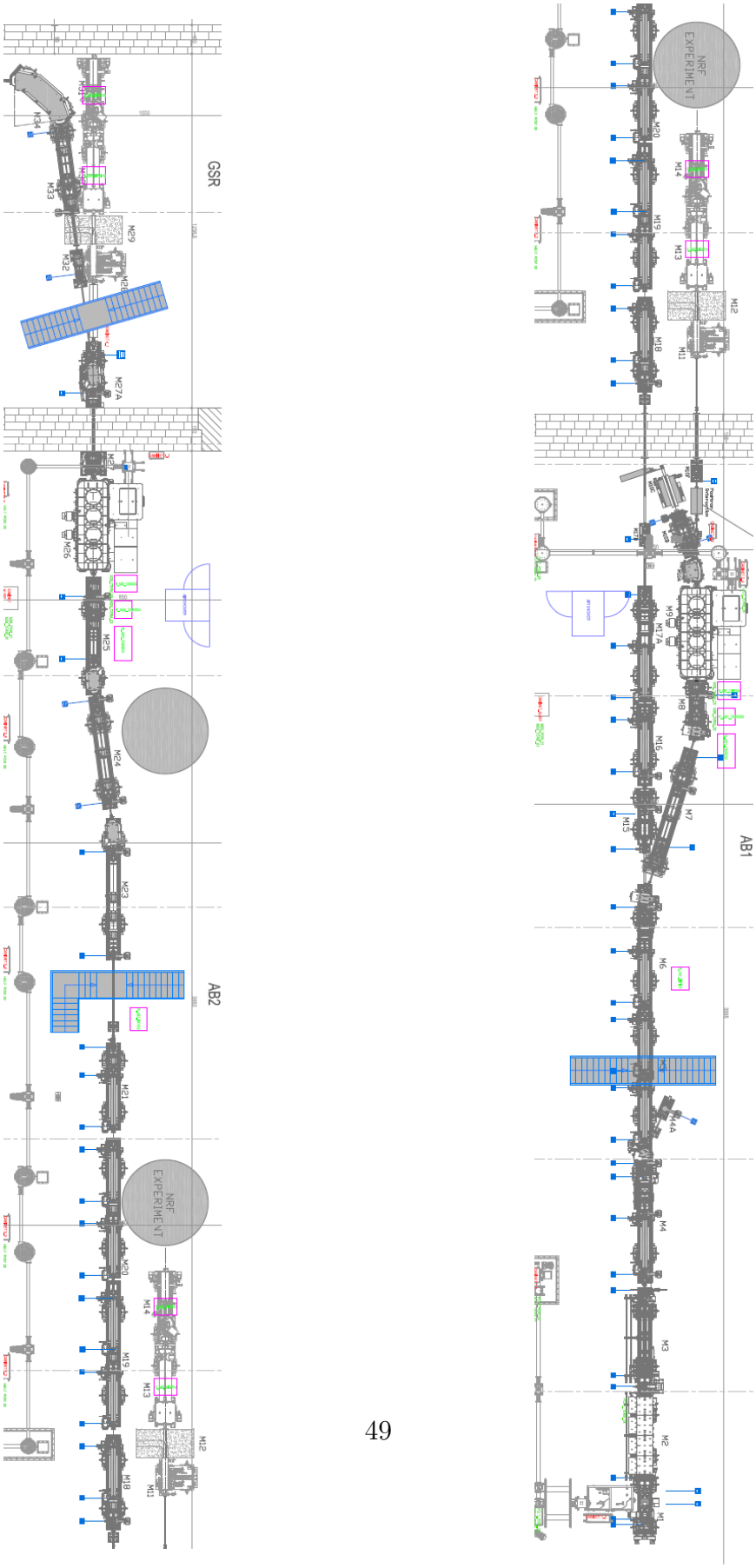

Figure 3.6: Drawing of the full machine. The image is split in two to fit in the page. The photoinjector is on the bottom right of the drawing.

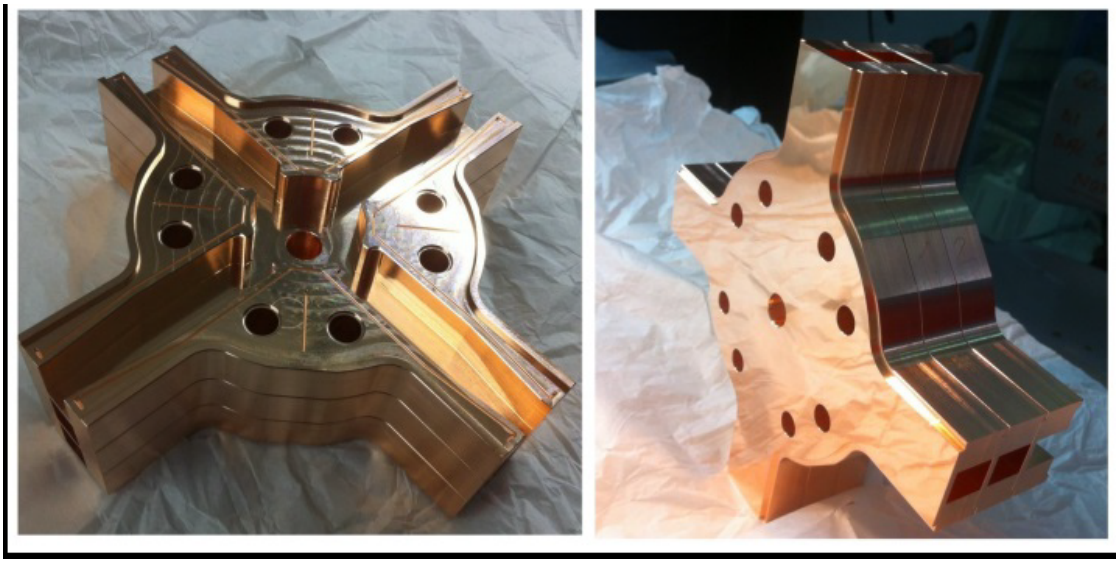

Figure 3.7: Photo of a prototype of a C-Band structure. Reprinted from [69]

3.2.4 Laser beam circulator

The Laser Beam optical Circulator (LBC) is under vacuum with the electrons entering and exiting it through two holes in the centres of two parabolic mirrors. 31 parallel Mirror Pair Systems (MPS) are arranged into a helix between them. The laser pulse is injected into the recirculator, hits a parabolic mirror and then passes through the centre of the recirculator which is where the laser-electron interaction takes place. Only a negligible fraction of the photons constituting the laser pulse are consumed by the interaction and thus the laser pulse continues its way onto the second parabolic mirror, is reflected and is then deviated by an MPS before hitting the first mirror again. This is done to conserve a constant crossing angle between the laser and electron paths that is essential for the monochromaticity of the final photon beam. After passing through all the MPS and crossing the interaction point 32 times, corresponding to the 32 electron bunches constituting one macro-pulse, the laser pulse is ejected from the recirculator. This whole process is then repeated every 10 ms. The design of this recirculator [70, 71] was the PhD work of a student at *Laboratoire de l'Accélérateur Linéaire* and is represented on Figures 3.10 and 3.11.

Two key design features need to be stressed here. On the one hand, there needs to be a good overlapping of the laser and electron beam at each crossing. On the other hand, the path length seen by the laser pulse between two crossings of the interaction point needs to be the same as the spacing between two consecutive electron bunches, i.e. 16 ns. The high degree of complexity of such a system necessitates precise diagnostic tools to verify the quality of the interaction at all

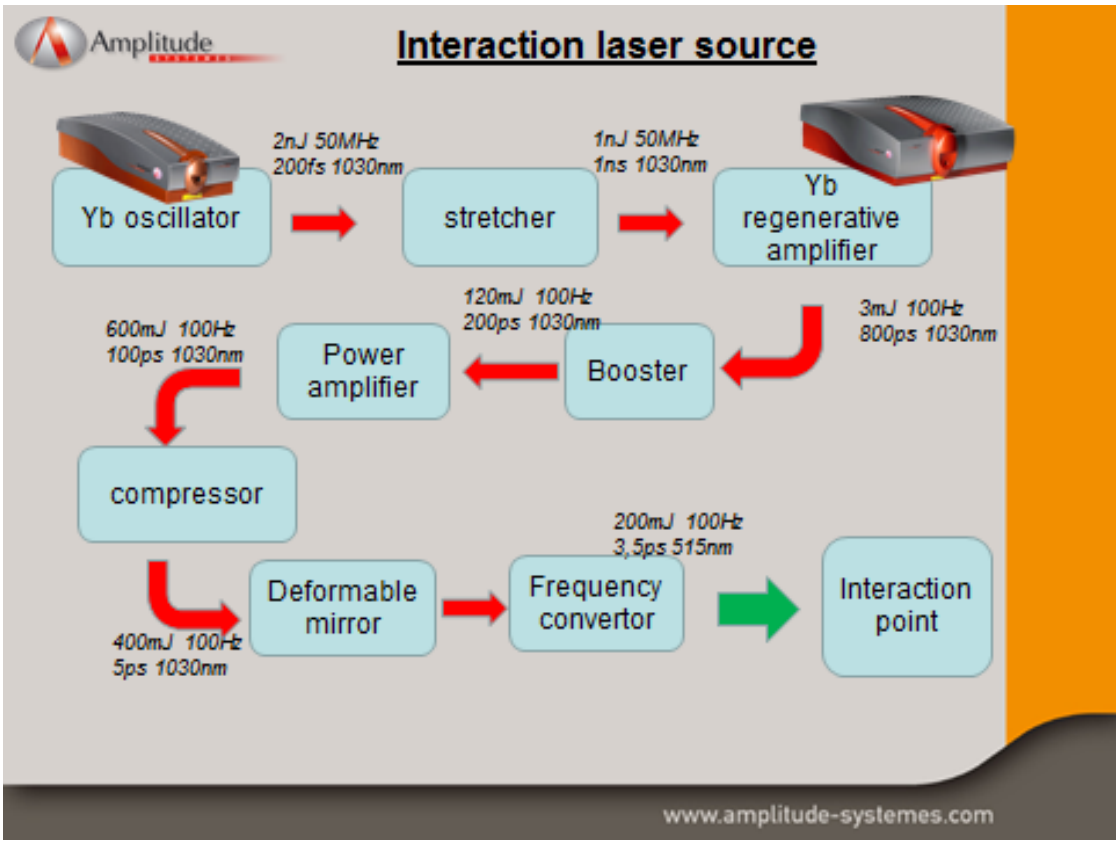

Figure 3.8: Block diagram representing all the elements of the interaction laser. Reprinted from [62].

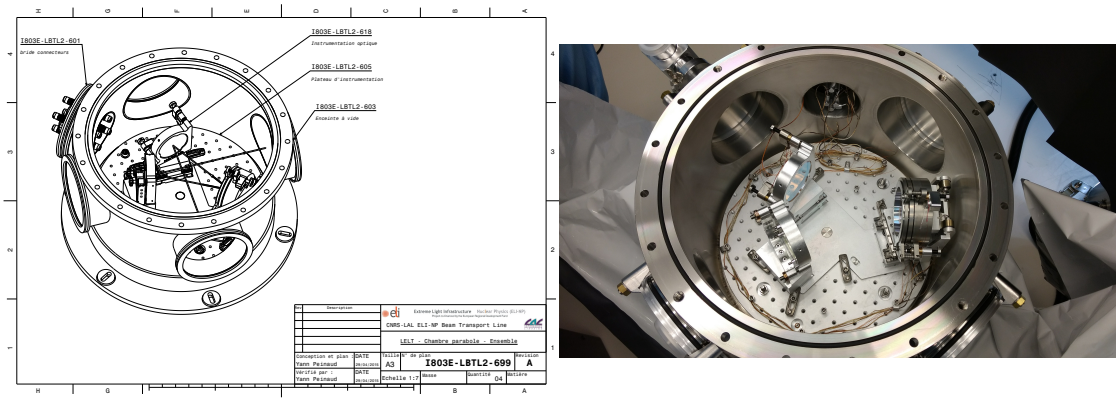

Figure 3.9: Drawing and photograph of a three-mirror system in its vacuum chamber for the interaction laser transport line. The parabolic mirror is the one in the right part of the chamber.

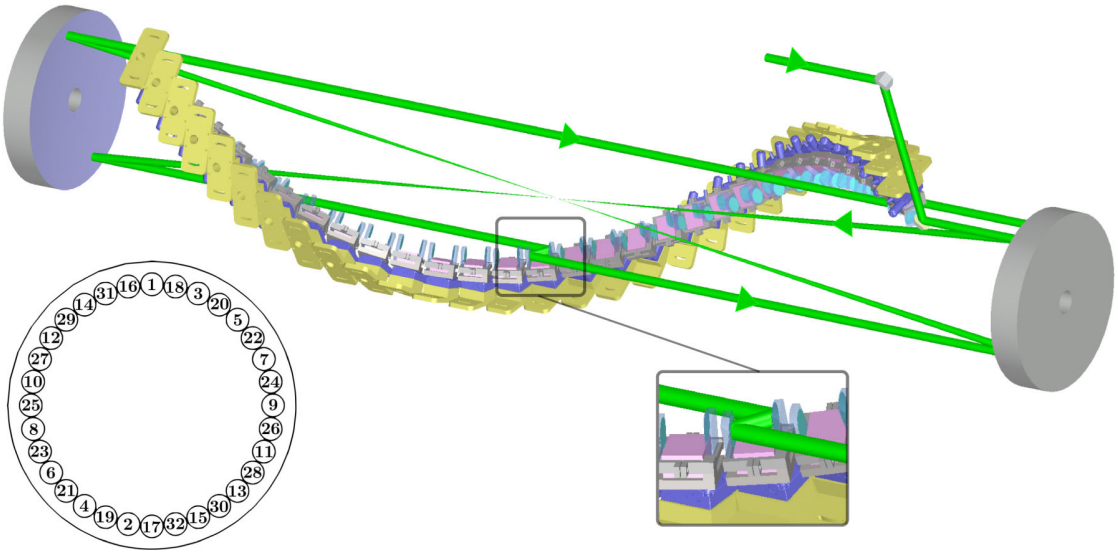

Figure 3.10: Isometric view of the ELI-NP GBS optical recirculator. On the bottom left, a projection of the sequence of impact of the laser pulse on the parabolic mirrors is shown. Reprinted from [71]

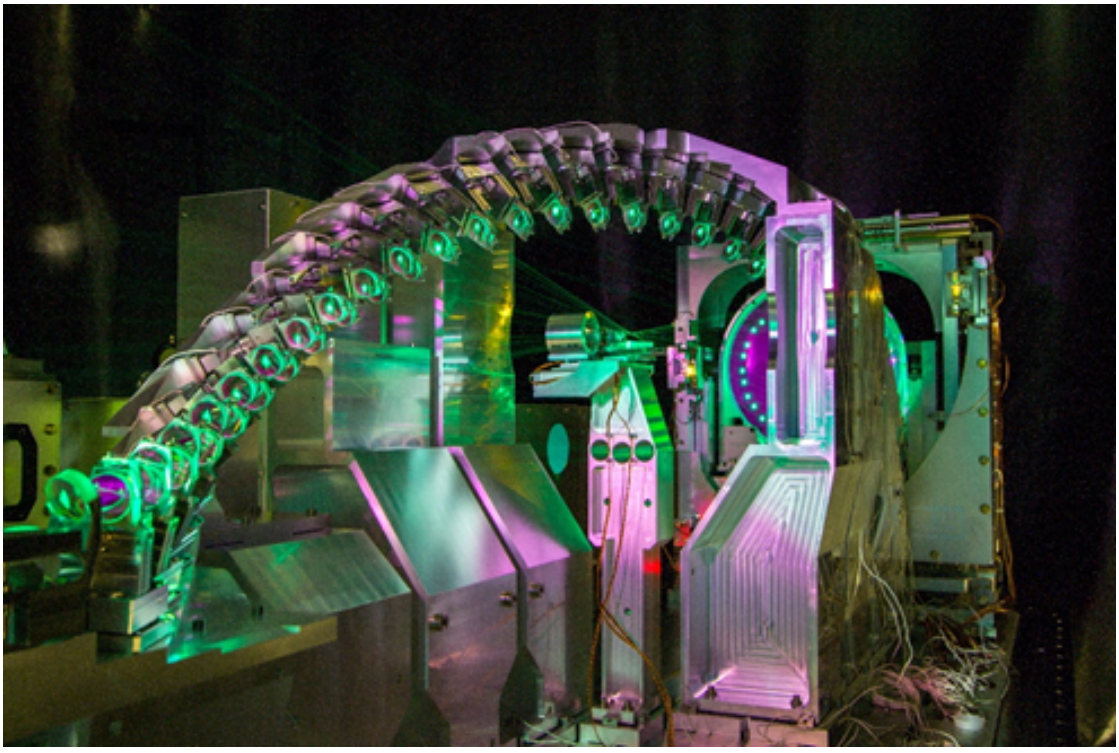

Figure 3.11: Photo of the recirculator.

times. A diamond sensor monitoring tool will be presented in the next chapter.

3.2.5 Recirculator modules

To ensure the correct propagation of the interaction laser inside the recirculator, or Laser Beam Circulator (LBC), 4 optical modules have been developed and will be installed together with the recirculator on the same optical table. They are the Injection Box (IB), the Synchronisation Tool (ST), the Fine Alignment Device (FAD) and the Laser Diagnostics (LD). They appear in orange, red, blue and purple respectively in Figure 3.12. Their design and requirements are described below.

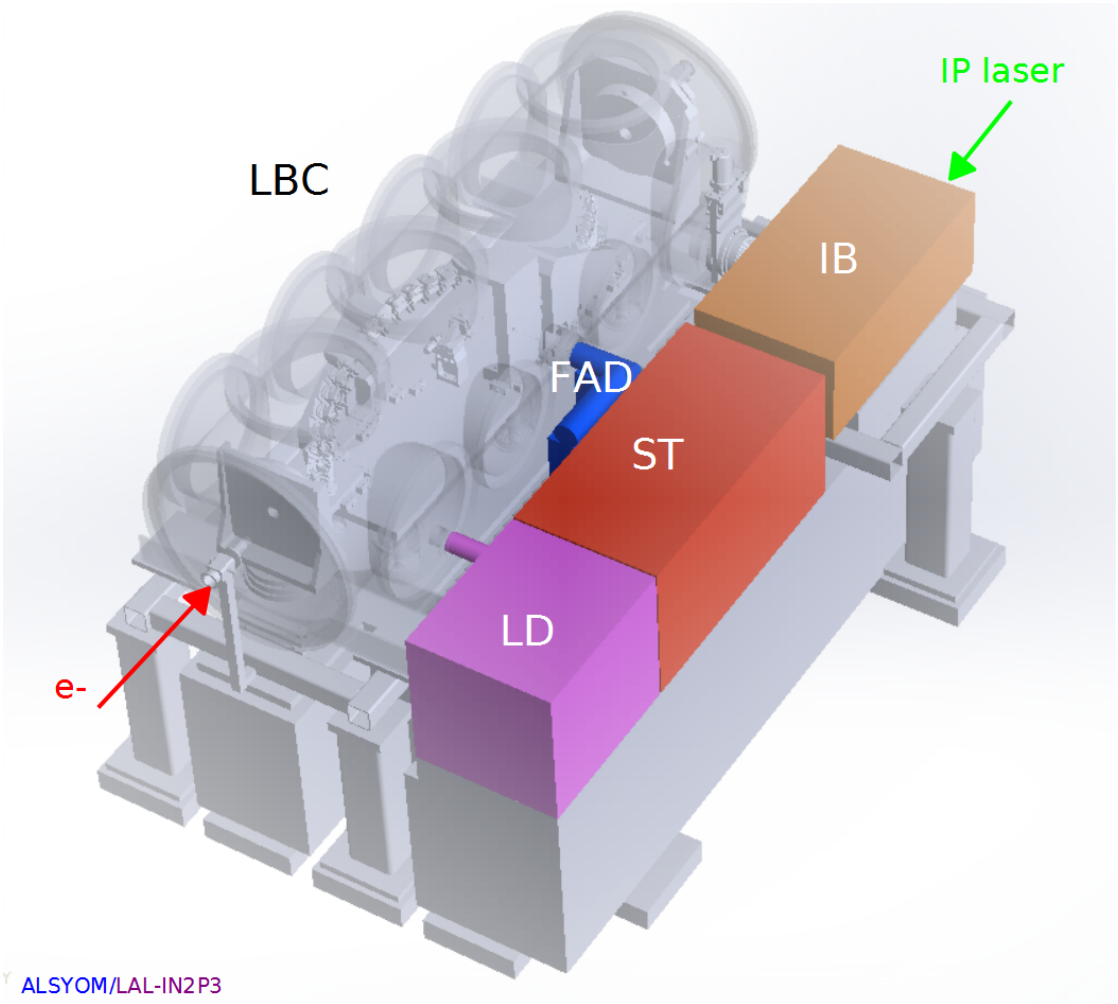

Figure 3.12: 3D model of the Laser Beam Circulator (LBC) and its modules.

The Injection Box is the last module in which the high intensity laser goes through before being injected into the recirculator. As such, its main purpose is to ensure the correct position and pointing of the laser beam and its stability over time. The mirrors need to have a high laser induced damage threshold to sustain 20 W. They are fitted on motorised mirror mounts made of a special stainless steel alloy that has a low coefficient of thermal expansion. To minimise vibrations, the whole module is under high vacuum and a pressure below 10^{-6} mbar. Its optical setup is presented on Figure 3.13.

The IB has a second purpose and that is to inject the laser beam provided by the Synchronisation Tool into the recirculator. A beamsplitter in the IB allows the extraction of a small percentage of the high intensity laser to send it to the LD.

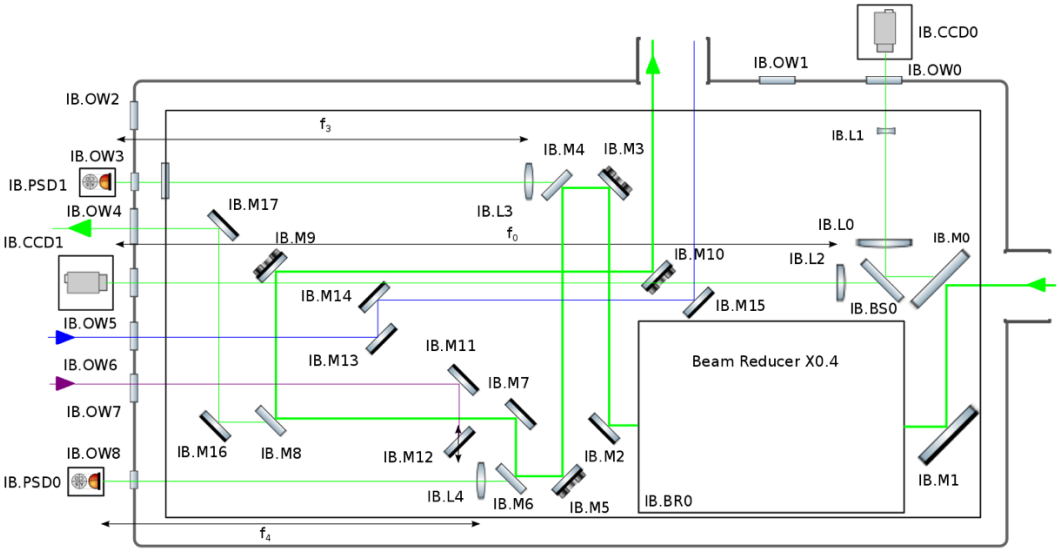

Figure 3.13: Optical setup of the Injection Box with the green line indicating the path of the high intensity laser, the purple one that of the ST laser branch that coincides with the green path from mirror IB.M12 onwards and the blue one that of the ST laser branch emulating the electrons.

The purpose of the Synchronisation Tool is to ensure the synchronous arrival at the interaction point of the laser beam with the electrons. As mentioned previously, 32 electron bunches separated by 16.108 ns are generated at a frequency of 100 Hz.

The path length of the laser for each pass in the recirculator must therefore also be 16.108 ns, with a tolerance of 100 fs. To satisfy these requirements, the ST uses a standalone femtosecond oscillator laser at 1030 nm and repetition rate of 62.09 MHz. It is then frequency doubled by second harmonic generation to match the 515 nm wavelength of the high intensity laser. This is done because the optics and their coatings are optimised for this wavelength. The laser beam is split in two in the ST with the first one sent directly to the IB that then injects it on the electron axis in the LBC to emulate the electron bunches. The second branch of the laser goes through a pulse picker to select one out of every 32 pulses. This branch is then also sent to the IB that injects it in the LBC exactly on the same path as the high intensity laser will take. Based on interferometry, the two branches of the laser can be synchronised in the FAD. The ST will only be used during alignment phases of the machines and not during normal gamma-ray production.

The Fine Alignment Device consists of an imaging system and a software to control the motors of the IB and LBC. Before production of gamma-rays, an alignment and synchronisation phase will take place, during which a thin pellicle mirror will be placed at the interaction point. This pellicle will be mounted on a motorised translation to move it in and out of location as needed. The pellicle acts as a beamsplitter with reflectivity smaller than 0.05 to allow the pulse to pass multiple times without affecting its intensity drastically. The two branches of the ST laser will join again at the interaction point and if synchronised correctly form interference patterns. The reflected rays of the pellicle are sent to an Intensified time-gated Charge-Coupled Device (ICCD), the PI-MAX4 from Princeton Instruments [72], to analyse the patterns of the 32 consecutive passes and run an iterative algorithm to optimise the position of each of the 31 Mirror Pair Systems. The layout is presented in Figure 3.14.

Lastly, the Laser Diagnostics module is there to check that the interaction laser is performing as expected. A small extraction from the IB is sent to the three instruments that comprise the LD. A powermeter measures the power of the laser. A wavefront sensor profiles the laser beam and allows online feedback to correct it if necessary by instructing mirror movement in the IB. An autocorrelator controls the laser pulse duration.

All these modules will be operated remotely via cabling to the central control command.

3.2.6 Diamond detector based real-time monitoring system

The diamond detector based real-time monitoring system is placed 2.6 m after the first interaction point and 6.3 m after the second. It is constituted of a diamond

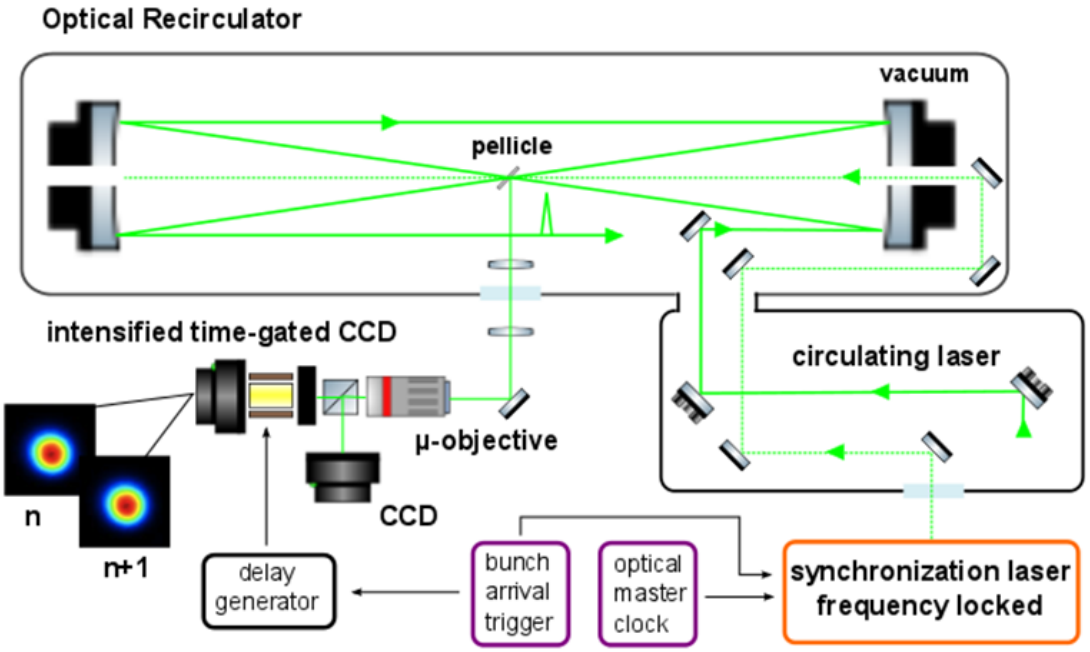

Figure 3.14: Layout of the Fine Alignment Device and its integration with the LBC and IB.

rectangular cuboid of 4.5 mm sides and 0.5 mm depth. It acts as a semiconductor when a high voltage is applied to it. The signal is then read out by a Wavecatcher digitizer. The purpose of this detection system is to monitor in real time the gamma beam exiting the recirculator and control the interaction takes place within the desired specifications. Simulations and experimental tests of this system were performed. They are presented in the next chapter.

3.2.7 Collimation system

Once the gamma-rays are produced, a collimation system is needed to provide the users with a monoenergetic beam. Indeed, the specifications require an energy bandwidth of 0.5%. One aspect that needs to be kept in mind is making sure the experimental area is not contaminated by radiation originating from said collimator. The system that was designed by our colleagues in Italy [73], also members of EuroGammaS, is shown in Figure 3.15. The main building block of the collimator is the slit: two $40 \times 40 \times 20mm^3$ blocks of tungsten alloy (97% tungsten, 2% nickel, 1% iron) on a motorised linear guide that adjusts their aperture individually in the range 0 – 25 mm. 12 such slits are placed on the beam axis in three groups of four, each with a relative rotation of 45°, resulting in an almost circular hole. An additional two slits are placed 20 cm downstream to clean the beam halo. These 14 slits are placed in a vacuum-pumped cabinet. Simulation results show that this collimation system can obtain the required 0.5% energy bandwidth for all the range of energies available at ELI-NP. Also, the simulated dose rate from photons and neutrons scattered by the collimator stays below 10^{-8} Gy/s, which is deemed acceptable.

3.2.8 Characterisation system

After the collimator, a characterisation system [74] will be placed to evaluate the generated gamma beam during the commissioning of the machine. It is composed of 4 instruments. The first one is the Compton spectrometer (CSPEC). It measures the energy and position of electrons and photons produced by the Compton interaction of the gamma beam on a micrometric target. This allows the reconstruction of the energy spectrum of the gamma beam. The second instrument is a segmented calorimeter (GCAL) where the gamma photons deposit energy as they go through it. This gives an estimation of the beam average energy and its intensity. Third comes the nuclear resonant scattering spectrometer (NRSS). A light element placed in an aluminium chamber scatters photons by nuclear resonance. The detection system is comprised of a precise spectrometer – a LYSO scintillator coupled to a photocathode – surrounded by BaF_2 scintillators that serve as fast gamma

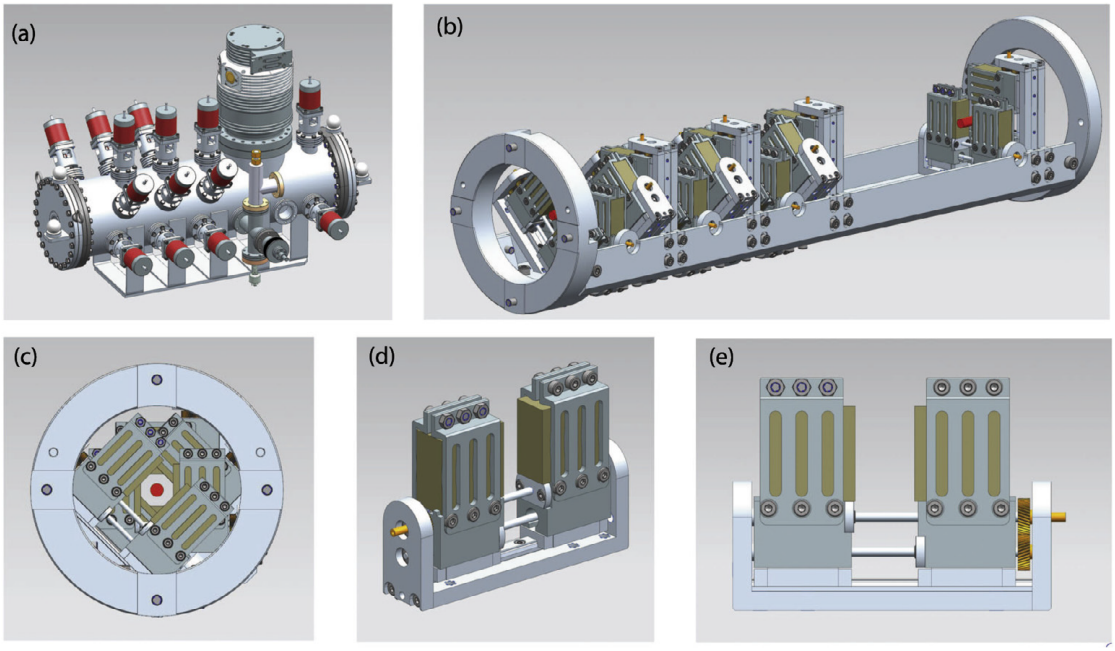

Figure 3.15: 3D models of the collimation system. *(a) Vacuum chamber containing the collimator. (b) Frame housing the 14 slits composing the collimator. (c) Collimation Hole. (d) Perspective view of a single slit. (e) Front view of a single slit.* Reprinted from [73].

counters. The detectors face this chamber at an angle of 135° with respect to the gamma beam. This allows for absolute energy calibration of the CSPEC and GCAL by scanning in energy the gamma beam, which is done by modifying the electron energy. At each nuclear resonance energy level, which are well known, the two former detectors are calibrated against the precise NRSS. Finally, the gamma beam profile imager [75] uses a scintillator crystal coupled to a CCD to evaluate the spatial distribution of the gamma beam.

3.2.9 Research Goals

The first experimental goals of the Romanian Nuclear Institute "Horia Hulubei" are described in a technical design report [76]. They will be performed when the machine is fully operational. One area of research will be nuclear resonance fluorescence that has been already touched upon in Chapter 1. Another research area that will be explored is photofission. An example that can be cited is the recent work of Csige et al. [77]. In this article they present new findings that confirm a triple-hump potential energy surface for extremely deformed Uranium-238 nuclei, that was believed to be only double-humped previously. More detailed analysis of the photofission reaction in actinides is hoped to be achieved with the narrow energy bandwidth of the gamma beam at ELI-NP. These studies, coupled with others regarding neutron capture rates, should in turn help in the understanding of astrophysical processes such as nucleosynthesis in heavy proton-rich stable nuclides [78].

Also, at the ELI-NP facility, two 10PW lasers are being constructed. One of the aims is to use them to research Nuclear Excitation through Electron Capture (NEEC), sometimes also called inverse internal electron conversion (IIEC). It is a process where a free electron is captured in one of the allowed shells of an atom. This releases a photon of a specific energy which is then reabsorbed by the nucleus of the atom taking it to an excited state. This phenomenon could explain the relative abundance of certain elements such as gold and platinum in the Universe. This rare process was theorised in 1976 [79] and a first observation was reported this year [80]. The experiment was performed at the ATLAS facility at Argonne National Laboratory with a beam of ^{90}Zr ions. The detector used was a Gammasphere [81], an array of 92 Germanium detectors disposed in a sphere as shown in Figure 3.17, with a Lithium target at its centre. NEEC was researched in a specific channel of ^{93}Mo with a half-life of 3.5 ns. By looking at the gamma-rays arriving in coincidence in a 2μs window, the process was confirmed to occur.

The high-power lasers at the ELI-NP facility should ease this area of research by providing high-temperature and high-density plasmas that have a large number of free electrons and thus increasing the probability of NEEC [78].

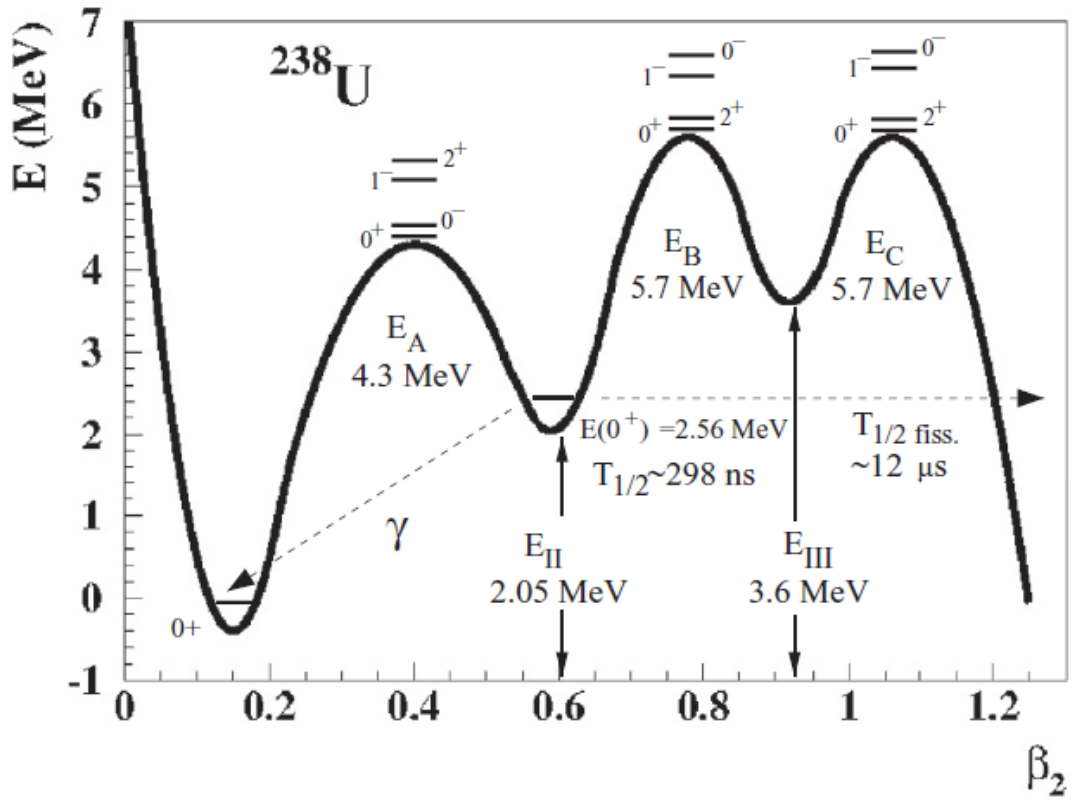

Figure 3.16: Potential energy surface as a function of the quadrupole deformation parameter β_2, with the triple-hump fission barrier clearly visible. Reprinted from [77]

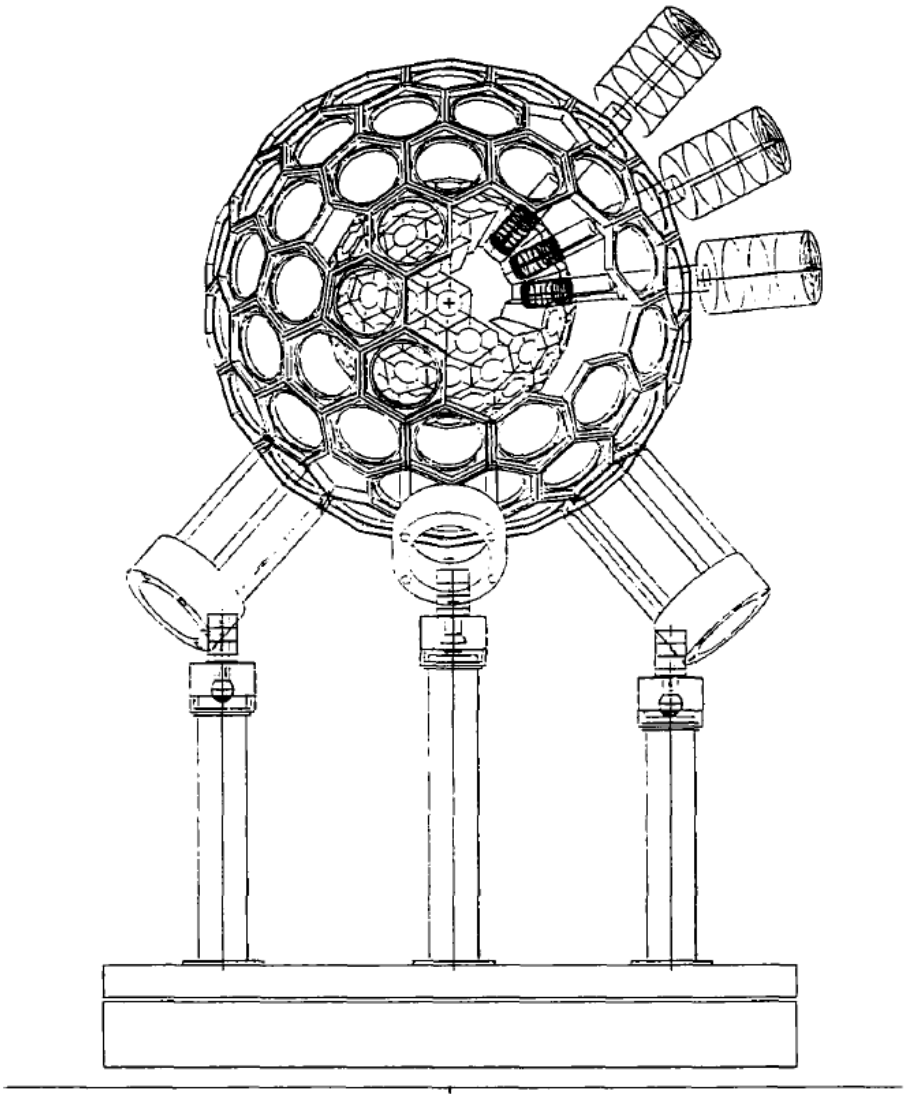

Figure 3.17: Sketch of a Gammasphere. Reprinted from [81]

3.3 Chapter summary

After detailing the Hungarian ELI-ALPS and Czech ELI-Beamlines pillars of the Extreme Light Infrastructure Project and their goals, the third Romanian pillar that is ELI-NP is presented with its components. Electrons are stripped from a photocathode by photoelectric effect and then accelerated to two interaction points – one low and one high energy – where they collide with a circulating laser pulse to generate 32 bunches of gamma-rays at a rate of 100 Hz. They then go through a collimator before being delivered to the user room. Along the line, a number of devices will be used to ensure the correct synchronisation, stability and performance of all the elements. One of these is the diamond sensor that will be used to monitor in real-time the gamma beam a few meters after the interaction point. This is expanded upon in the next chapter.

Once the machine is completed, it will serve initially for NRF and photofission experiments proposed by the Romanian Institute of Nuclear Physics, which oversees the whole project. It will then at a later stage be open to other research institutions.

Chapter 4

Photocathode laser system synchronisation

4.1 Synchronisation system at ELI-NP

A good synchronisation of all the parts of the machine is essential for the production of the gamma beam for the end-users. Indeed, the synchronisation between the electron bunches and the laser pulses at the interaction point must be below 500 fs. To fulfil this requirement at such a large scale infrastructure, an optical signal reference distribution system is used. The reference signal is generated by a Reference Master Oscillator (RMO) which is a μ-wave crystal oscillator with ultra-low phase noise characteristics. Its frequency is 2856 MHz.

The RMO then seeds an Optical Master Oscillator, which distributes the reference signal to the various device clients through actively stabilized fibre links. The stability in each link is of approximately 70 fs.

The various clients (laser systems, RF power stations, beam diagnostics, hardware...) are each individually locked to the reference signal. A schematic layout of this timing and synchronisation system is presented in Figure 4.1. For the rest of the chapter, we will focus only on the synchronisation of the photocathode laser system on which I worked personally. As a reminder, the photocathode laser system is the one described in Section 3.2.1.

4.2 Balanced Optical Cross-correlator

4.2.1 Theory

To ensure the good synchronisation of laser pulses with electron bunches at the interaction point, we need a good timing of the photocathode laser used to generate

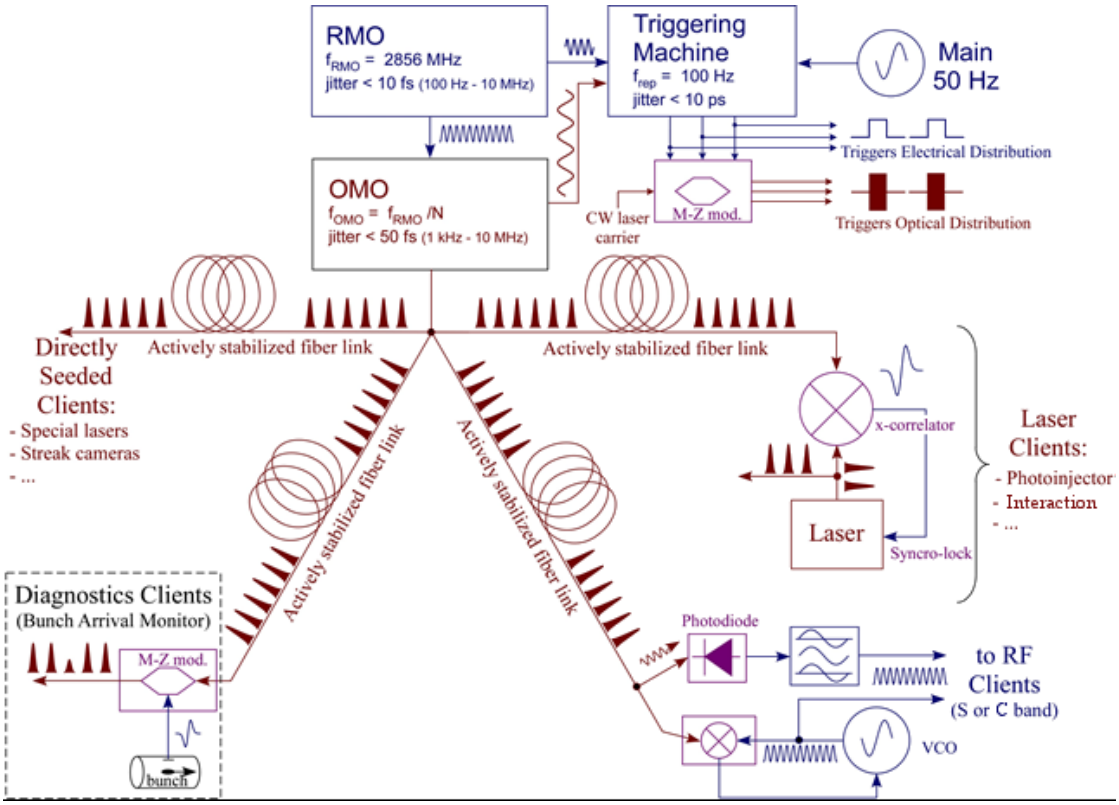

Figure 4.1: Timing and synchronisation system layout for the ELI-NP machine. Reprinted from [62]

the electron bunches. To this purpose, an optical bench was developed to verify the synchronisation of the photocathode laser with respect to the reference signal through a mixer.

The chosen method for mixing is Two Photon Absorption (TPA) in a photodetector as optical mixer [82]. Electronic mixing was ruled out as the timing accuracy required was too challenging in regard to the expertise in our team. An optical mixer based on second harmonic generation in a non-linear crystal was not considered as the optical power available was too low.

The Balanced Optical Cross-correlator (BOC) is an optical mixer (optical cross-correlator) which consists of two delayed lines. The delay introduced allows to generate a bipolar error signal made from the difference between the signal coming from both lines. A photo of the BOC bench and its optical diagram are shown in Figure 4.2.

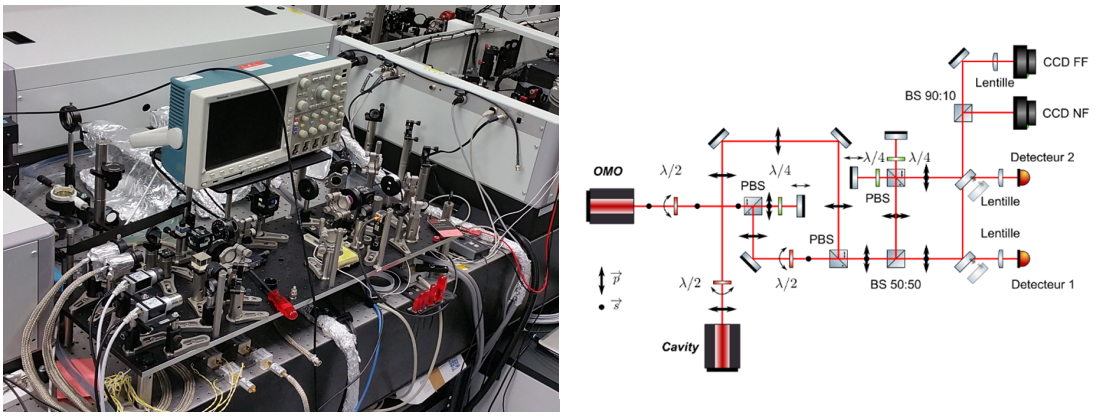

Figure 4.2: Photo and diagram of the balanced optical cross-correlator

4.2.2 Synchronisation Procedure

Due to the way the 32 laser pulses are generated in our system, there are 3 signals to be synchronized to the OMO after adjusting the delay of the BOC: the *phase* signal which is the synchronization of the first pulse of the train and the OMO, the *delay line 16 ns* which is the delay between the first and the second pulse of the train (DL2) and the *cavity repetition rate* which is the period of the cavity (DL3). These three signals are represented in Figure 4.3.

As a result, the procedure to synchronize the 3 signals is the following:

1. Find the phase with 1 pulse (DL1 scan).
2. Find the synchronisation of delay line 16 ns with 2 pulses (DL2 scan).
3. Find the cavity repetition rate with 32 pulses (DL3 scan).

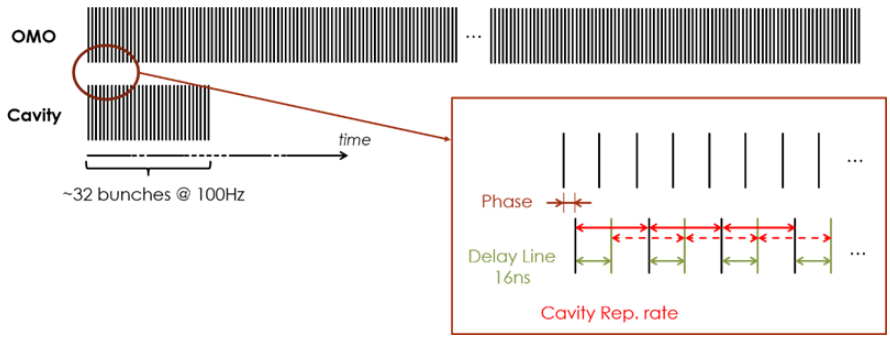

Figure 4.3: Diagram of the signals from the photocathode laser to synchronise with the reference from the OMO. The phase (brown) is the first step of the synchronisation procedure, the delay line (green) the second step and the cavity repetition rate the third step.

4.2.3 Choice of detector

Four different Hamamatsu detectors were tested but only one was compatible with TPA signal, the G1115 detector, a photo of which is shown in Figure 4.4.

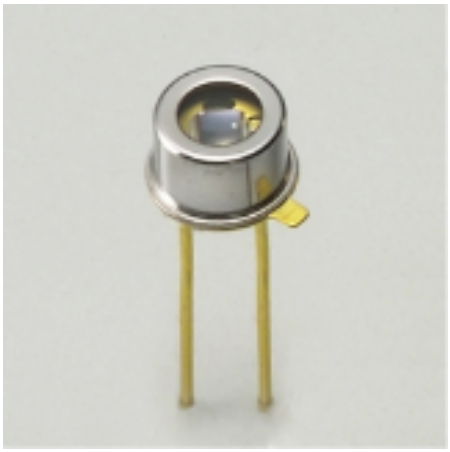

Figure 4.4: Photo of the Hamamatsu G1115 photodiode used for two-photon absorption optical mixing.

The drawback of the G1115 photodiode is a low bandwidth (rise time up to 1 μs). Consequently it is not possible to distinguish the pulses in the train, the frequency being 62.08 MHz. This means that the only information available is an average synchronization of the train. This forces us to use a second bench to synchronize and lock the DL2 while the BOC will lock the DL3 and the phase alternately. We choose to use an interferometer for locking the DL2 (cf. Figure 4.5) once synchronized on OMO with the BOC. Due to the noise in the proximity

of the setup, it is not possible to lock on a fringe. Even if the locking is achieved, we cannot guarantee that after one step of the DL2 the fringe remains the same as the lock is lost during the step. Therefore we choose to use the contrast to lock the interferometer. The accuracy when using the contrast is much less than the pulse width, thus using the OMO (Δt (RMS) $<$ 200 fs) as secondary laser line, we can guarantee a synchronisation to less than 200 fs.

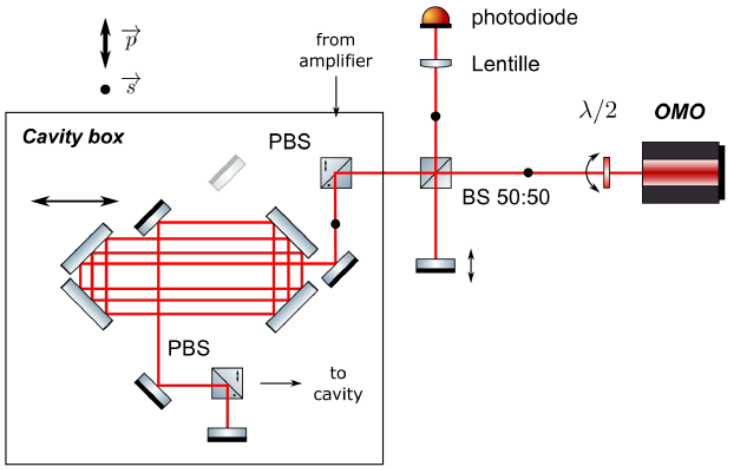

Figure 4.5: Diagram of the interferometer.

To overcome the drawback of the photodiode bandwidth we decide to use 2 amplifiers of at least 20 dB gain for each line with an AC coupling input. The AC coupling ensures the low frequencies are filtered out of the photodiode hence the high frequencies are exacerbated. In this way it is possible to artificially increase the photodiode bandwidth up to the amplifier bandwidth and distinguish the pulses in the train. Using this information it is possible to design a synchronization system that uses only one BOC and measures the synchronization of each pulse independently. As this method is simpler by having only one bench, we decide to use it for the following.

4.2.4 Results

The results shown here were obtained in one day with the OMO laser power at the entrance of the bench approximately equal to 50 mW. The laser power of the train was previously adjusted to obtain the maximum signal to noise ratio of the synchronisation. The raw signals are generated by a G1115 photodiode and

amplified with the Virtual High Bandwidth method using 2 amplifiers (type: Mini-Circuits ZFL-1000LNB+). Then, they are recorded by a 5 Gsample/s oscilloscope in 250 MHz bandwidth mode. First of all, the multi-pulse cavity was aligned to avoid the need to re-align the laser chain during the measurements or between two measurements. Then we proceeded to the different scans explained in Section 4.2.2.

The extraction of the signal is difficult due to the bench sensitivity to various parameters: beam pointing, beam intensity, beam polarization. Consequently we try to be the most independent as possible of these sources of perturbation. For beam pointing, the laser beam spot size on the photodiode of the MPC train is fixed to approximately twice the spot size of the laser beam of the OMO. For intensity variations, we suppose that their origin is mainly from the laser beam train thus a linear photodiode (Thorlabs DET36A) was used at the output of the compressor for normalisation procedures. The impact of laser polarisation on the measurement is assumed to be negligible.

The signal for each pulse is calculated as the peak amplitude on the G1115 photodiode divided by the corresponding peak amplitude squared coming from the linear photodiode. Once the scan is done, a calibration factor is calculated for each G1115 photodiode to normalize their signal. The calibration is the average signal of the ten first points of the scan (where there is no synchronization signal). This provides the signal for each line, then we take the difference of each line to obtain the error signal.

4.2.4.1 Phase

The first scan consists of blocking the injection in the MPC and switching off the Pockels Cell to get only one pulse on the BOC. The results obtained for this scan are presented in Figures 4.6, 4.7 and 4.8. From the zero-crossing of the error-signal, we see that the synchronisation is under 30 μm, which corresponds to 200 fs.

4.2.4.2 Delay line 16 ns

Once the phase is set at the zero crossing of Figure 4.8, the second scan with the DL2 is performed. For this scan, the Pockels Cell is switched on to get 2 pulses on the BOC. The results obtained for this scan are presented in Figures 4.9, 4.10 and 4.11. From the zero-crossing of the error-signal, we see that the synchronisation is under under 30 μm, which corresponds to 200 fs.

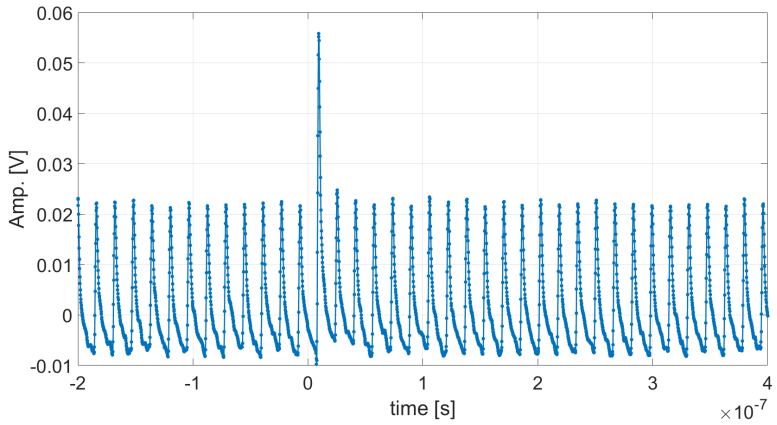

Figure 4.6: Typical waveform obtained with the photodiode 1.

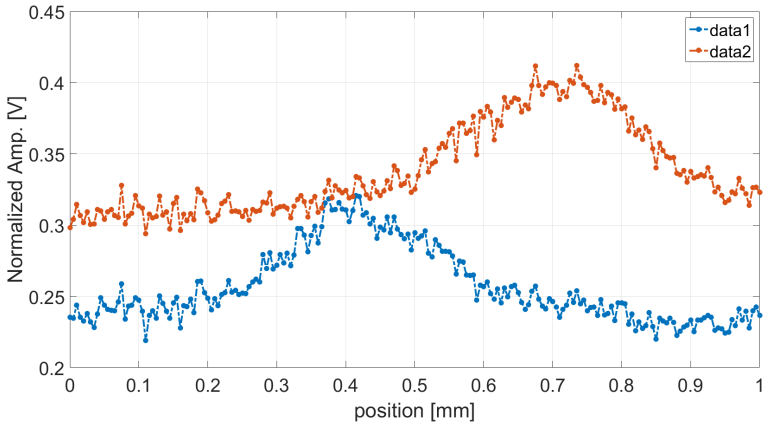

Figure 4.7: Raw extracted signals (without the normalization by the calibration factor) with respect to the scan position.

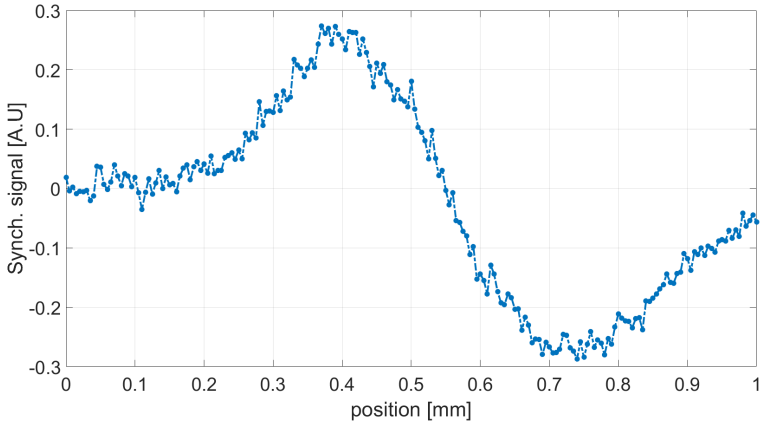

Figure 4.8: Error signal obtained for the phase scan.

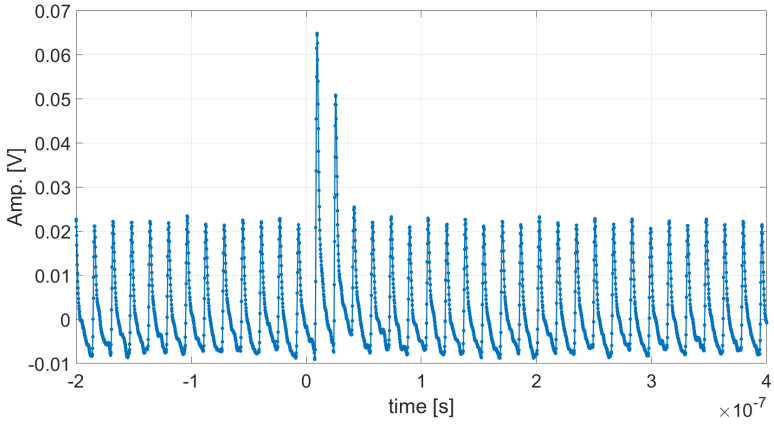

Figure 4.9: Typical waveform obtained with the photodiode 1.

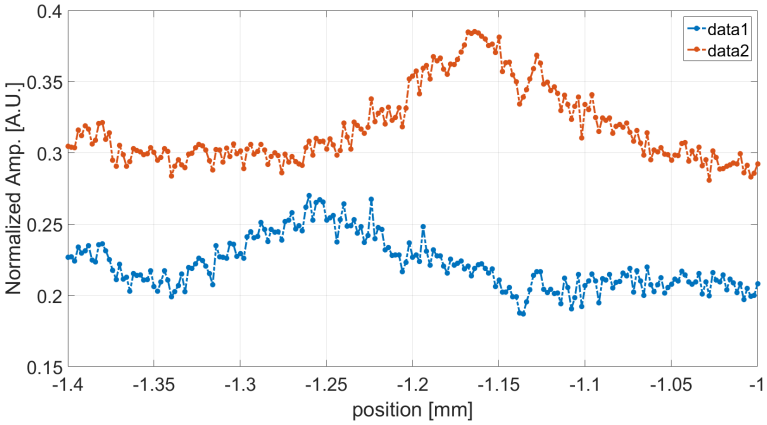

Figure 4.10: Raw extracted signals (without the normalization by the calibration factor) with respect to the scan position.

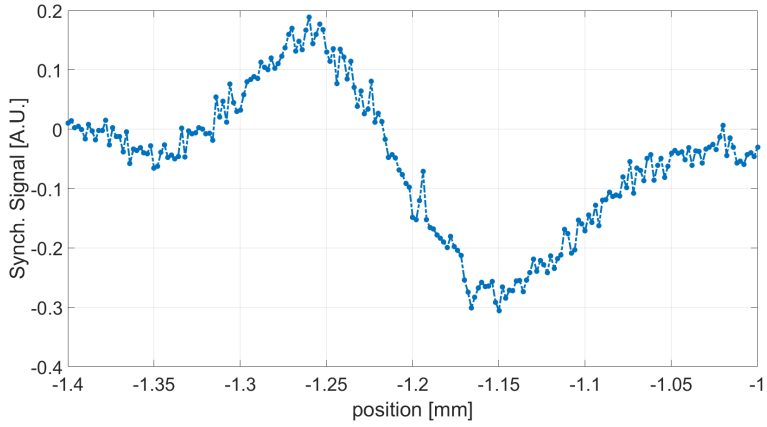

Figure 4.11: Error signal obtained for the 16 ns delay line scan.

4.2.4.3 Cavity repetition rate

Finally, once the DL2 is set at the zero crossing of Figure 4.11, the last scan with the DL3 is performed. For this scan the MPC is unblocked, thus we have 32 pulses on the BOC. The results obtained for this scan are presented in Figures 4.12, 4.13 and 4.14.

From the Figure 4.14, one can conclude that the position of the synchronization for the different pulses is different. The error signal for all the pulses is represented in Figure 4.15. The $1/x$ shape of the error signal is typically from a bad synchronization of the phase and/or the DL2. If we consider that the MPC produces a twin train which has to be spaced by exactly a period of the OMO (T0 = c/f0) then for the odd (respectively even) pulses the delay with respect to the OMO is $\Delta t_{2k+1} = k(T_0/2 - T_1) + \phi_1$ (respectively $\Delta t_{2k} = k(T_0/2 - T_1) + \phi_2$, where k is the pulse replica, ϕ_1 (respectively ϕ_2) the delay of the first pulse and $T_1 = (L_0 + 2p)/c$ is the period of the cavity with L_0 the initial cavity length and p the DL3 position.

For the synchronization ($\Delta t_{2k+1} = 0$) we obtain:

$$p_{2k+1} = \frac{1}{2}\left(\frac{\phi_1 c}{k} + \frac{T_0 c}{2} - L_0\right) \tag{4.1}$$

The theoretical shape of the synchronization is of the form $1/x$ as shown in Figure 4.15. This can help to further improve the synchronisation if necessary by adjusting the DL1 and DL2 positions.

The synchronisation of the 32 pulses with this method is under 200 fs which is within the specified requirements.

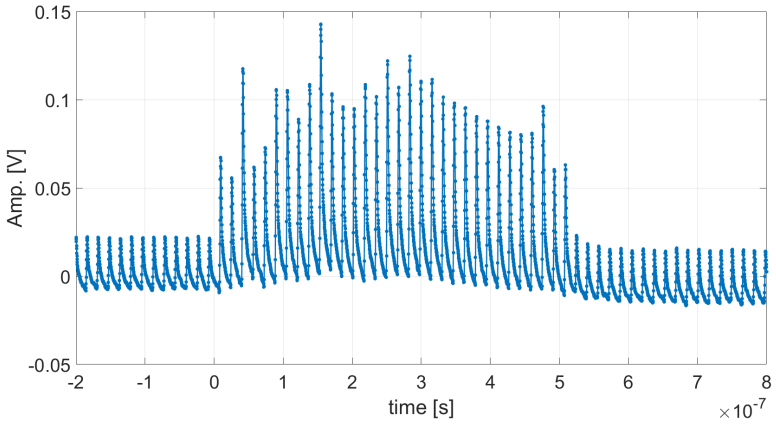

Figure 4.12: Typical waveform obtained with the photodiode 1.

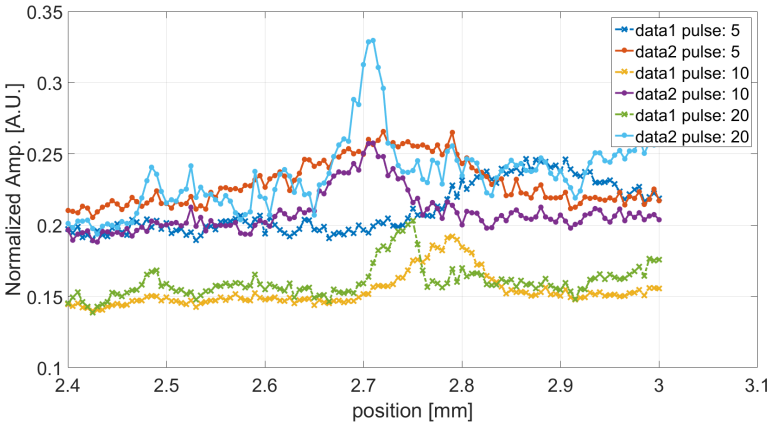

Figure 4.13: Raw extracted signals (without the normalization by the calibration factor) with respect to the scan position.

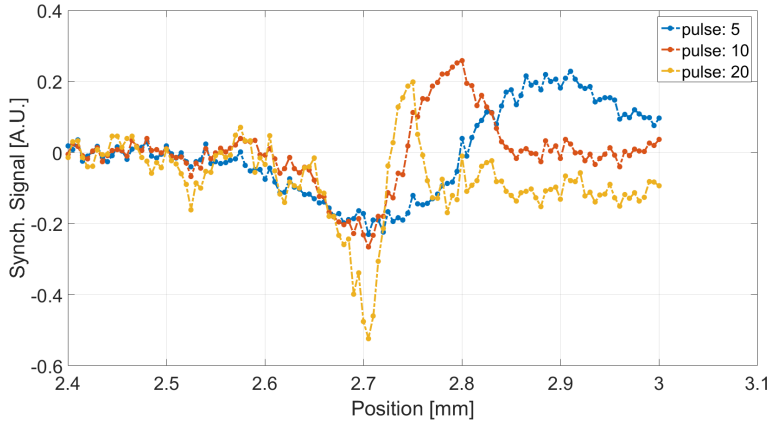

Figure 4.14: Error signal obtained for the cavity repetition rate scan for three pulses out of 32 (number 5, 10 and 20).

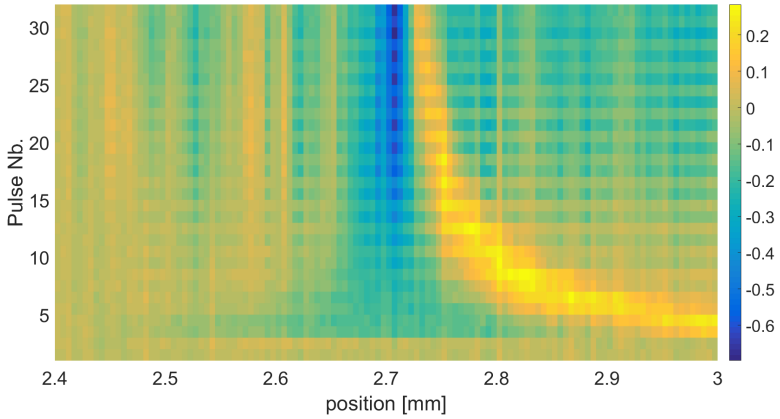

Figure 4.15: Error signal of all 32 pulses obtained for the cavity repetition rate scan. The vertical axis represents the pulse number, the horizontal axis the scan position and the colour scale the synchronisation signal.

4.3 Chapter Summary

In this chapter, the overall synchronisation concerns of the ELI-NP machine were presented. The goal is to have the time of arrival of the electron bunches and laser pulses within 500 fs of each other to ensure a good and constant production of the gamma beam for the users. Then, the specific example of the synchronisation of the photocathode laser system was described. A balanced optical cross-correlator was developed at LAL. It is based on the optical mixing through two-photon absorption in a photodiode of the laser pulses from the multi-pulse cavity with the pulses from the reference optical master oscillator. This method demonstrated a synchronisation of the photocathode laser of under 200 fs which is well within the specified requirements.

Chapter 5

Diamond Sensor Testing

5.1 GEANT4 Simulations

To evaluate the adequate response of the diamond detector in a gamma-ray beam, simulations were performed on GEANT4 [83]. It is a toolkit developed at CERN to simulate the passage of particles through matter. The key steps of the simulation are:

1. The generation of photons that resembles the beam of a Compton gamma source.

2. The propagation of these photons through all the layers of the detector, following strict physical rules.

3. Identifying the particles interacting in the detector.

5.1.1 Gamma beam generation through MATLAB

The first step in the simulations is to generate a flux of photons emulating the Compton interaction. The goal is to create a file of individual photons with their position, momentum and energy. What is done is the Compton interaction between the laser and the electrons is simulated via Monte-Carlo based on their cross-section. The generated gamma rays are then propagated along the z-axis until a given distance D, which is the separation between the interaction point and the position of the diamond detector. This is one of the input values we introduce into our simulation. The other input parameters that we have are the electron energy P_e, the laser wavelength λ, the angle of incidence between the electron and laser beams α, the Stokes parameters of the laser S_{1-3} and the electron beam polarization.

Finally, the last parameter the user defines is the size of the surface in the x-y plane in which he wants gamma rays.

From these parameters, first a cross-section σ is calculated, given by the following equation [40]:

$$\sigma = J \times J_2 \times (A + S_1 \times B + S_2 \times C + S_3 \times (P_1 \times S_x 2 + P_2 \times S_y 2 + P_3 \times S_z 2)) \quad (5.1)$$

In all the simulations in this thesis, the electron beam is supposed as unpolarised such that $P_1 = P_2 = P_3 = 0$. The above equation thus simplifies to:

$$\sigma = J \times J_2 \times (A + S_1 \times B + S_2 \times C) \quad (5.2)$$

$$J = (1 - \beta^2) \times r_0^2/(1 - \beta \times \cos(\theta_0))^2; \quad (5.3)$$

$$J_2 = \frac{D}{(D^2 + x^2 + y^2)^{3/2}}; \quad (5.4)$$

$$\begin{aligned} A = a \times (1 + cos(\theta)^2 + (k_i - k_f) \times (1 - \cos(\theta))); \\ B = a \times \sin(\theta)^2 \times \cos(2\phi); \\ C = a \times \sin(\theta)^2 \times \sin(2\phi); \end{aligned} \quad (5.5)$$

$$a = 0.5 \times (\frac{k_f}{k_i})^2; \quad (5.6)$$

$$\begin{aligned} k_i = 2 \times \gamma \times E_p/m_e; \\ k_f = 1/(1 - \cos(\theta) + 1/k_i); \end{aligned} \quad (5.7)$$

where E_p is the photon energy in MeV.

$$\begin{aligned} \theta_0 = \tan^{-1}\big(\frac{\sqrt{x^2 + y^2}}{D}\big) \\ \theta = \cos^{-1}\big(\frac{\cos(\theta_0) - \beta}{1 - \beta \times \cos(\theta_0)}\big); \\ \phi = \tan^{-1}\big(\frac{y}{x}\big); \end{aligned} \quad (5.8)$$

$$\begin{aligned} E_e = \sqrt{m_e^2 + P_e^2}; \\ \gamma = E_e/m_e; \\ \beta = \sqrt{1 - 1/\gamma^2}; \end{aligned} \quad (5.9)$$

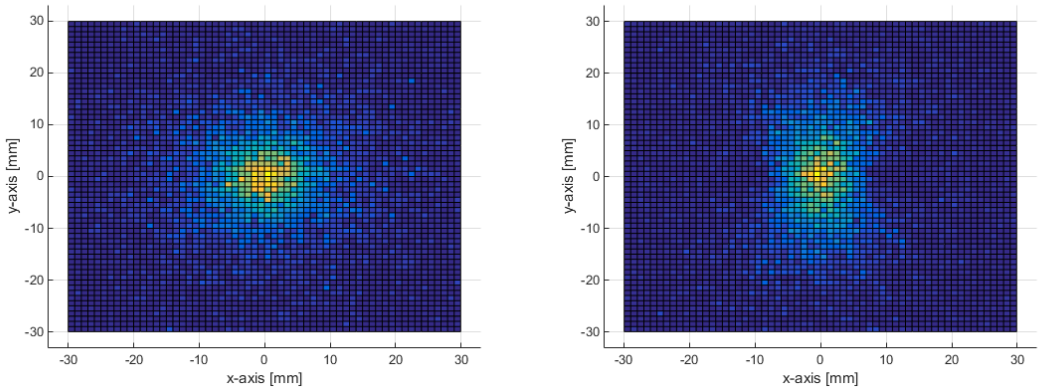

Figure 5.1: Two-dimensional transverse projection of the number of photons in the simulated gamma beam, for circular polarisation of the laser on the left and horizontal polarisation on the right.

The photons generated from this simulation can be represented on a 2D x-y transverse map where x is the right-left axis, y the top-down axis and z the direction of propagation of the gamma-rays. Two examples are given in Figure 5.1. The parameters for these examples were chosen to be representative of the conditions that will be found at ELI-NP, namely electrons at 80 MeV, a laser wavelength at 515 nm, a crossing angle of 8° and the distance from the interaction point at 2.6 m. The mean energy distribution along the x and y-axis for the photons of the simulation used for Figure 5.1-left are presented in Figure 5.2.

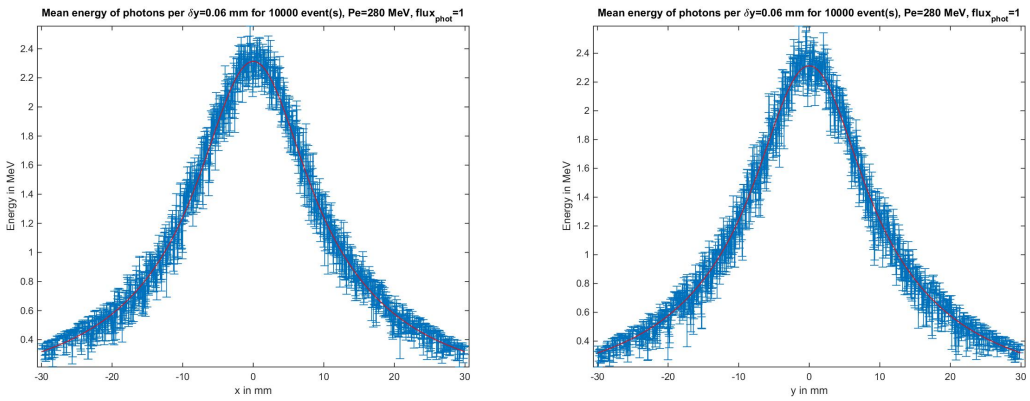

Figure 5.2: Mean energy distribution in x and y-axis

5.1.2 Detector Geometry

The main detector part is a diamond rectangular cuboid of 4.5 mm sides and 0.5 mm depth. In the centre of both sides, a 3 mm squared titanium-platinum-gold metallization with a thickness of 470 nm serves to carry the charges to a remote amplifier. This is then put on a plate with dimensions $10 \times 10 \times 1.6mm^3$ for handling purposes. This plate can be made from PCB (polychlorinated biphenyl) or ceramic depending on the use-case of the detector, open-space for the former and vacuum environment for the latter.

For tracking purposes, a number of vacuum detectors are placed around this system. These are purely simulation constructs that give information on the particle trajectories once they have exited the materials and are not interacting any more.

Finally, the detectors provided by CIVIDEC are available in 2 models: single-block or four quadrant sensor. Their difference comes in the metallization. In the 4-quadrant sensor, it is divided into 4 equal parts that each collects charges from the corresponding region of the sensor as shown in Figure 5.3. For the simulation work, this does not lead to a drastic change as it is the charge deposited at a specific position that is evaluated. The metallization serves only as another material where physical phenomena can happen thus affecting the final charge deposited in the diamond.

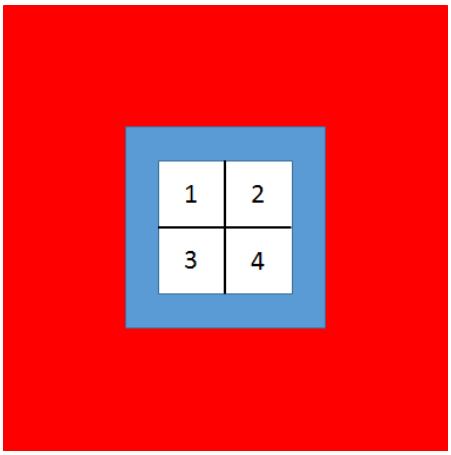

Figure 5.3: Face-on drawing of the 4-quadrant detector. The base plate appears in red, the diamond in blue and the metallization divided in 4 in white.

5.1.3 Physics Lists

One important parameter to take into account during GEANT4 simulations is the physics list [84]. This is the set of physical models that defines all the possible interactions between particle and matter. The one we use here is called QGSP_BERT. It is the one used by default by the ATLAS and CMS experiments at the LHC. The Quark-Gluon String (QGS) and the Bertini(BERT) [85] cascade models for which the list gets its name focus on protons, neutrons, pions and kaons interactions with nuclei at different energies. Many other models are used for different physical phenomena such as neutron capture, nuclear interactions with electrons, muons and hadrons or the electromagnetic package [86] that interests us primarily here as the interactions we have in the diamond are photon or electron based.

5.1.4 Tungsten foil

To increase the low probability of interaction of photons in diamond, a tungsten foil was added in front of the detector to serve as electron converter. Indeed, as a high atomic number material, tungsten releases electrons that are stripped by the high energy gamma rays. This tungsten foil needs to be as close to the detector as possible as the electrons are emitted in a large cone around the axis of propagation of the gamma beam. Figure 5.4 shows this practically. Here, 20 MeV photons are shot at the centre of a 0.5 mm tungsten layer at an orthogonal incidence. We then count all the electrons traversing the volume of the detector placed behind. As the detector is placed further from the tungsten, the number of electrons decreases, with already half less electrons after the gap is widened by 7 mm.

The distance between the foil and the detector also has an importance for the 4-quadrant version of the detector as it blurs the spatial information of interacting particles.

The thickness of the tungsten was optimised by the same method. 20 MeV photons were shot at the centre of the foil in contact with the detector. The number of electrons as a function of the tungsten thickness is shown in Figure 5.5. This number increases at first, reaches a plateau at 2 mm before decreasing. This is explained by the fact that some electrons produced near the surface of the foil are reabsorbed inside the material before being able to exit.

For this reason, the thicknesses chosen to test experimentally at newSubaru are 0.5, 0.75, 1 and 2 mm.

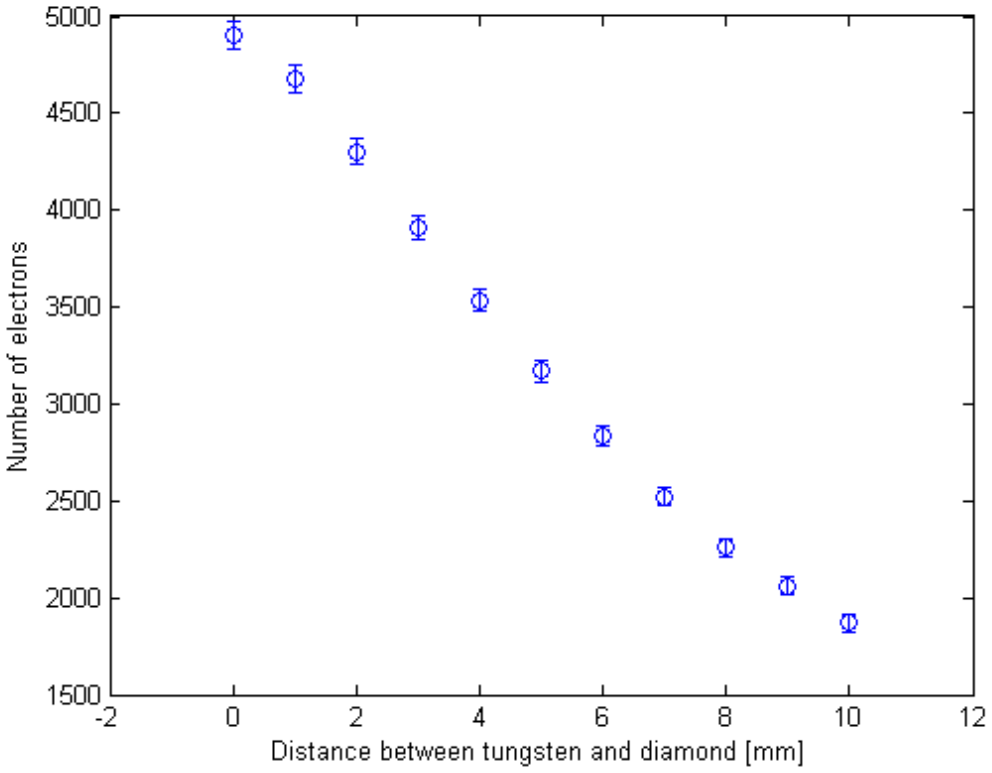

Figure 5.4: Number of electrons depositing energy counted in the detector as a function of the distance between the tungsten and diamond layers, in the range 0 to 10 mm.

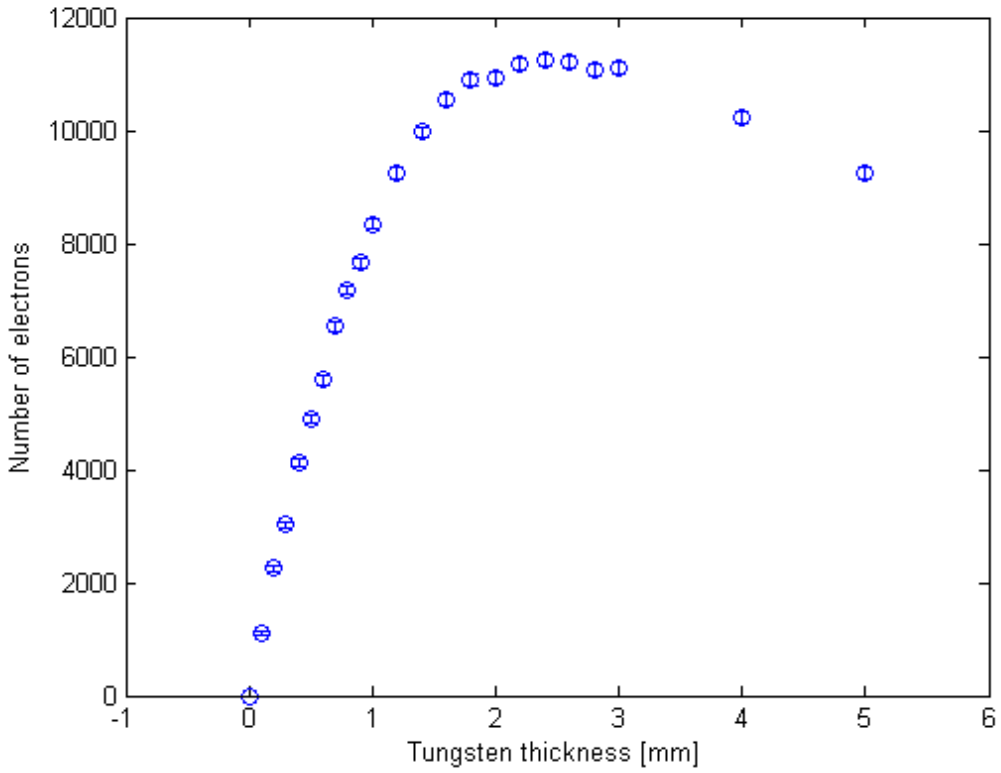

Figure 5.5: Number of electrons depositing energy counted in the detector as a function of the tungsten thickness, in the range 0 to 5 mm.

5.1.5 Background noise

From simulation files from our colleagues in Italy, we were able to measure the influence of the background noise on the diamond detector due to the environment it is in. To achieve this, in GEANT4 we place a thin sensitive detector made of vacuum. It is placed 6 m after the interaction point, where our real detector would be to see what particles traverse it. The collimation system is also modelized, 3m further. A beam pipe, with a 2 cm radius, goes in a straight line from the interaction point to the collimator. The inverse Compton interaction was simulated by our Italian colleagues with the CAIN Monte-Carlo package which creates a file of photons resulting from the interaction, with their respective position and momentum. They are then introduced into GEANT4 to be propagated.

First of all, we see that our simulation is working as expected by looking at the photons passing through our sensitive surface. The distribution of photons in the x-y plane 6 m after the interaction point is given in Figure 5.6 for a vertical polarisation of the laser beam.

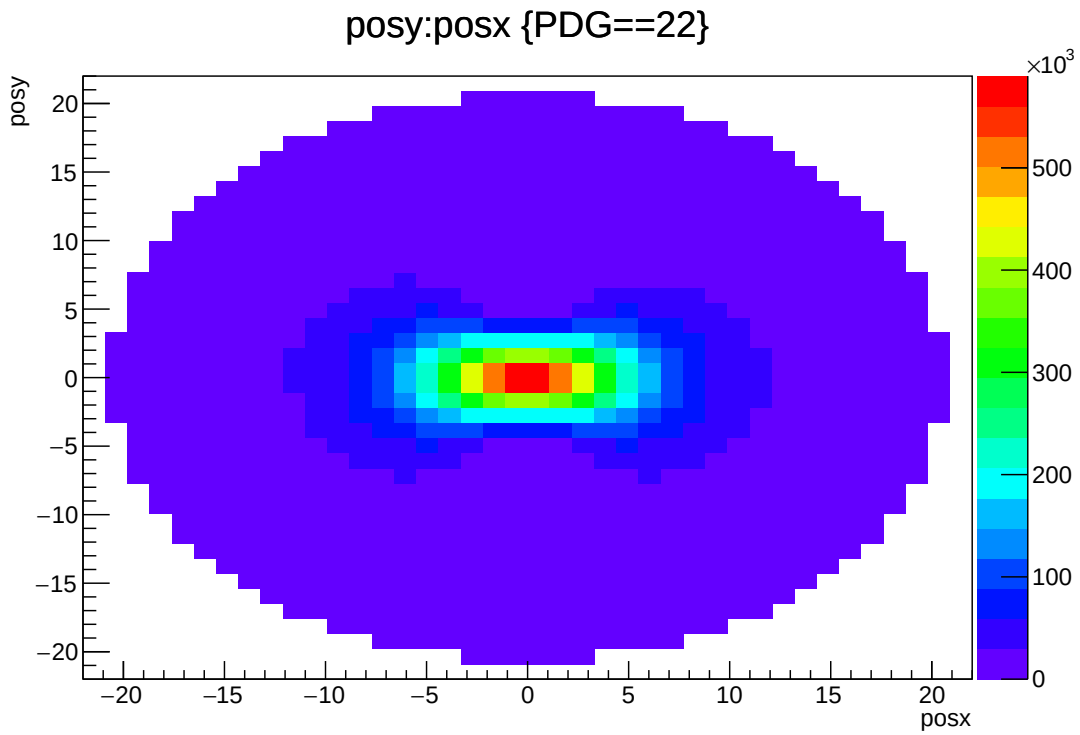

Figure 5.6: Distribution of photons in the x-y plane 6 m after the interaction point. The shape is given by a vertical polarisation of the laser beam. The colour scale gives the number of entries.

We then look at any other particles that might have passed through the surface of interest and we see that a number of electrons and positrons are indeed present. The distribution of electrons is shown in Figure 5.7.

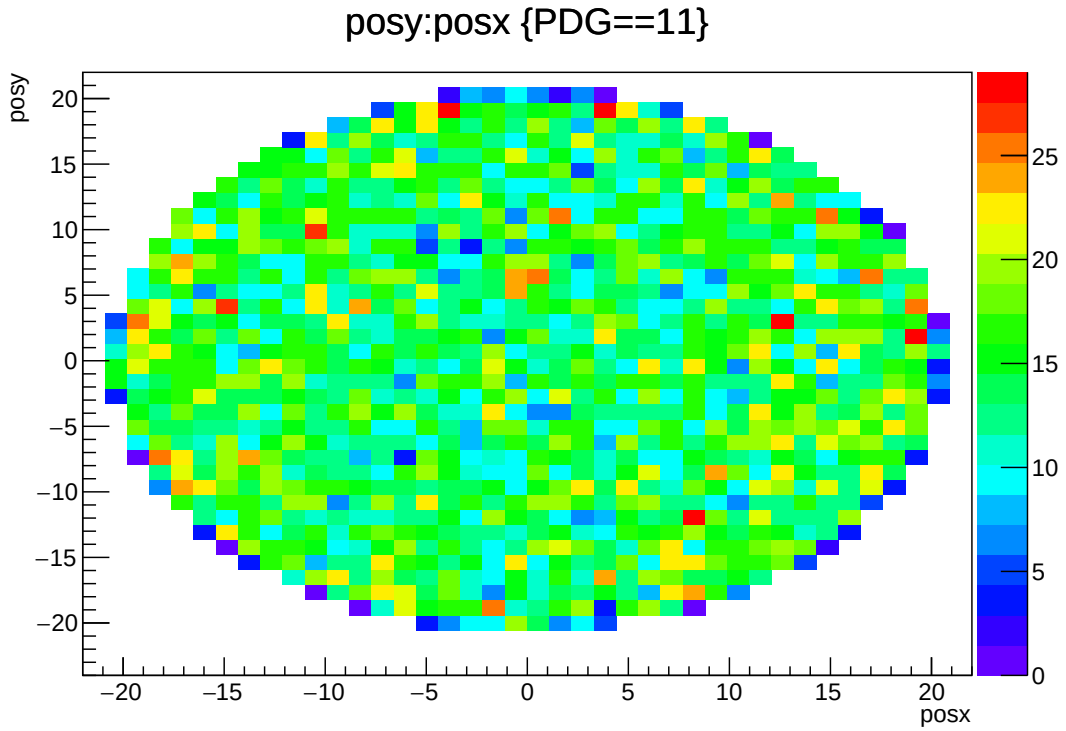

Figure 5.7: Distribution of electrons in the x-y plane 6 m after the interaction point. The colour scale gives the number of entries.

From GEANT4, we can extract where these electrons originate from by identifying their vertices. As shown in Figure 5.8, the vast majority of electrons comes from the beam pipe, within 50 cm before and after the detector. These are electrons stripped by high energy photons colliding with the inner wall of the pipe. Their count nevertheless is far inferior to the number of photons passing through and we can therefore suppose the background noise from this source to be zero. A negligible amount of electrons is also backscattered from the collimator.

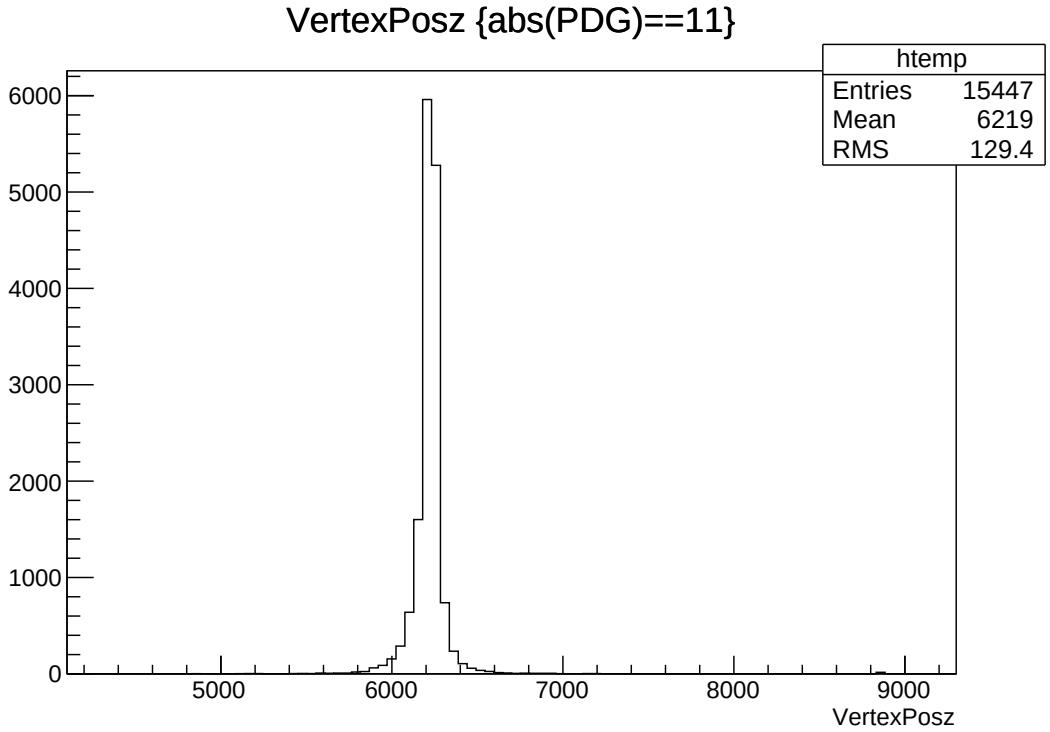

Figure 5.8: Distribution of the z-coordinates of the vertices of origin of the electrons passing through the sensitive detector.

5.2 Test at HIγS

5.2.1 Experimental set-up and data

The HIγS facility [47, 87, 88] is to this day the most intense source of photons in the 1 to 100 MeV energy range. They are produced by Compton scattering off electrons. A free electron laser (FEL) installed in the accelerator generates the interacting photon beam. The tuning of the photon energy is achieved by changing the electron energy and the FEL wavelength, that can involve changing optical mirrors. By using either a planar or a helical wiggler, both linear and circular polarisations can be obtained for the laser. Provided that on-axis photons are selected and that smearing due to the finite size and emittance of the beams is negligible, the photon beam polarisation is expected to be given by the laser polarisation, This has been checked by measurements carried out at HiγS [87]. The optical cavity at the Duke FEL Laboratory (DFELL) is 53.7 m long allowing Compton interactions at a rate of 5.58 MHz. The number of produced photons reaches 10^9 per second over the full solid angle but the exact intensity depends upon the desired photon beam energy. The monochromaticity of the beam is enhanced by a series of circular apertures centred on the beam that allow the selection of on-axis photons[1]. The drawback is a reduction of the photon flux.

In this experiment, a diamond sensor was placed at 63.47 meters from the Compton interaction point and 10.51 m downstream of an 18 mm aperture. The transverse diameter of the photon beam where the diamond sensor is located is therefore about 20 mm.

The apparatus installed in the beam consists of an sCVD diamond sensor from the CIVIDEC company [89] of transverse size 4.5x4.5 mm^2 and 500 μm thickness. The Ti-Pt-Au electrode metallisation has an active area of 4x4 mm^2 and a thickness of 500 nm. With a 400 V bias voltage used in the subsequent experiment the expected FWHM of the pulse is approximately 5 ns for MIPs (Minimum Ionizing Particles). In order to observe the small signal provided by the diamond sensor, a low noise, broadband amplifier also provided by CIVIDEC [89] is employed. The amplitude of the amplified signal from a MIP amounts to about 7 mV. This level of signal is very close to the electronic noise which has an RMS value of 1.4 mV, dubbed σ_{noise}. Over the two days of data taking, the noise was found to be stable, with the variation to this figure being approximately 0.03 mV peak to peak. The diamond sensor and the preamplifier are mounted on two translational stages along the horizontal and vertical axes in order to precisely place the diamond sensor in the γ beam. A pre-alignment of the position of the sensor to within 1 cm is made with the help of a He-Ne laser tracker. The

[1]The Compton process induces a correlation between the energy of the emitted photon and its angle with respect to the reference electron beam axis.

output signal of the amplifier is read out by a USB WaveCatcher [90]. This data acquisition system allows 1024 points to be registered with a sampling frequency of 3.2 GHz. Waveforms are sent to a PC connected to the DAQ by USB whenever a new trigger is received and the reception and storage of the previous event has been made by the PC. The passage of electrons through Beam Position Monitors (BPMs) of the accelerator [91] produces the trigger signal. Coincidences of this trigger with the detector signal allows events to be registered at rates of a few hundreds of Hertz. A threshold of 7 mV is applied to the detector signal. Indeed, triggering with the BPM alone would lead to a large fraction of trigger with no signal in the sensor, since the number of incident photons is only a few units and the detection efficiency about a fraction of a percent. The number of events recorded per unit of time is limited by the bandwidth of the communication between the PC and the WaveCatcher. Nevertheless, the actual equivalent rate between two consecutive events is computed, thanks to counters embedded in the DAQ, and stored with the waveforms allowing the actual rate of events seen by the DAQ to be reconstructed. This system was mounted within a couple of hours and operated without any manual intervention for three days.

The photon beam energies used were 2, 3 and 7 MeV corresponding to electron energies of 280, 335 and 511 MeV, respectively. The photon production rate was approximately 10^6-10^7 photons/s. Two different settings of the DFELL were used during this experiment. They are dubbed *regular* and *bunched*. In *regular* mode, two electron bunches are circulating in the storage ring. They are both lasing and producing photons by Compton backscattering. They are separated by 179 ns, which corresponds to twice the revolution frequency of 2.79 MHz. In the *bunched* mode, a first electron bunch serves as the lasing material. This created laser beam collides with three other electron bunches separated in time by 16.8 ns, which were injected into every third RF bucket for the first nine (out of a total of 64). This mode is of particular interest as it presents a similar temporal configuration as the one that will exist at the ELI-NP-GBS. Data related to the machine is also stored in an EPICS [92] database provided on site. This information allows matching the data taken with the WaveCatcher to precise running conditions, namely, the electron beam energy, the FEL laser polarisation and the relative flux measured using a 5-paddle monitor [93], placed a few metres upstream from the diamond sensor. The 5-paddle allows determining the flux with a systematic uncertainty of 2 % but this performance has never been proven experimentally at the energies used in the present analysis [93].

The 5-paddle flux measurements are updated in the database approximately once a minute. The acquisition of a run of 10000 events lasts about one to two minutes. Moreover, a constant shift of a few seconds between the data taken and the database information is present and cannot be corrected for offline. These

facts render the run by run normalisation of the rate of observed events by the 5-paddle reference difficult. Only average measurements over tens of minutes can be corrected with the information from the EPICS database.

5.2.2 Results

The signal of a particular run is presented in Fig. 5.9 where the fast response of the signal is clearly seen. The data is corrected for pedestals, event by event, by averaging over the first 100 samples. Contributions to the small diamond sensor signal due to cross-talk in the Wavecatcher channels from the large trigger signal are corrected for by subtracting 7.5×10^{-4} times the trigger signal from the diamond sensor signal. This coefficient has been extracted using data when the photon beam production was switched off but with electrons still present in the accelerator. It was not found to vary over time by more than 10%. Applying this correction lowers the estimation of the charge, calculated using Eq. 5.10, by approximately 10%. The average pedestal correction is 5.5 mV with an RMS value of 0.6 mV. Jitters of a few nanoseconds are observed in the trigger signal and are corrected for. The residual jitter is below the sampling period: 0.3125 ns. Candidate peaks with an amplitude of at least $5\,\sigma_{\text{noise}} = 7$ mV are recorded and searched for. Events with multiple candidates are discarded unless otherwise stated. The full width at half maximum (FWHM) of the signal pulses is extracted after a smoothing procedure consisting of applying a moving average filter over 10 consecutive points. The resulting distributions are given in Fig. 5.10 for three beam energies. The average FWHM pulse duration is 6.2 ns with an RMS value of 0.2 ns for 2 MeV photons. This value is similar at 3 and 7 MeV. The smoothing procedure changes this value by about 10 %.

The collected charge Q is given by

$$Q = \frac{\epsilon}{GR}\int_{t_1}^{t_2} u(t)dt, \tag{5.10}$$

where ϵ is the charge collection efficiency, $G = 140$ is the gain of the preamplifier, $R = 50\,\Omega$ is the input resistance of the WaveCatcher, $u(t)$ is the measured voltage, and t_1 and t_2 are the first instants of zero-crossings of $u(t)$ before and after the maximum of $u(t)$, respectively. The integral is computed numerically. The precise calibration of Q is not performed in this experiment since the rate and not the collected charge of the events is proportional to the flux due to the small number of photons per bunch and the relatively low efficiency of the detector. However it is interesting to compare the collected charge for various photon energies with respect to the response to electrons with energies corresponding approximately to those of

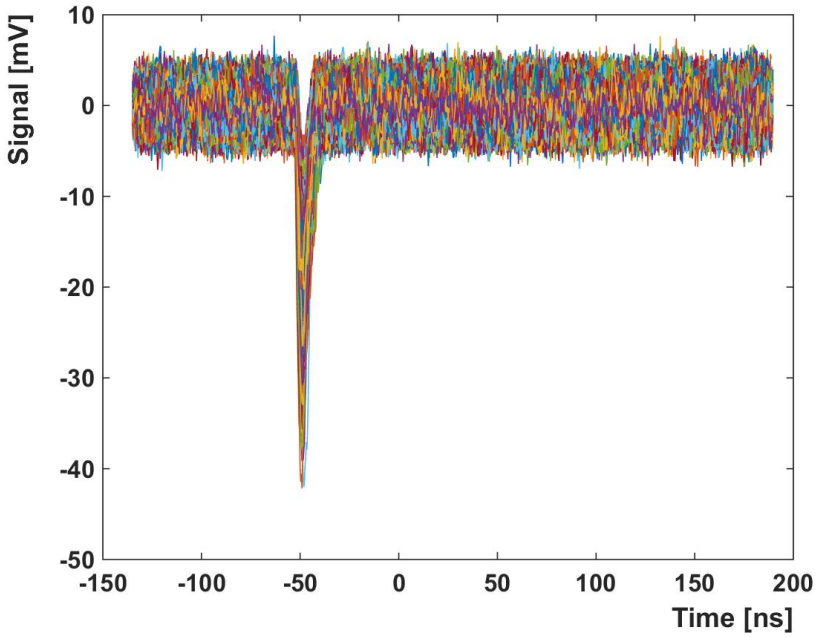

Figure 5.9: Observed signal of a run of 10000 events collected at a photon beam energy of 3 MeV. The events are corrected for trigger jitters, cross-talk and pedestals. The typical pulse duration is of the order of a few nanoseconds and all the events are well synchronised.

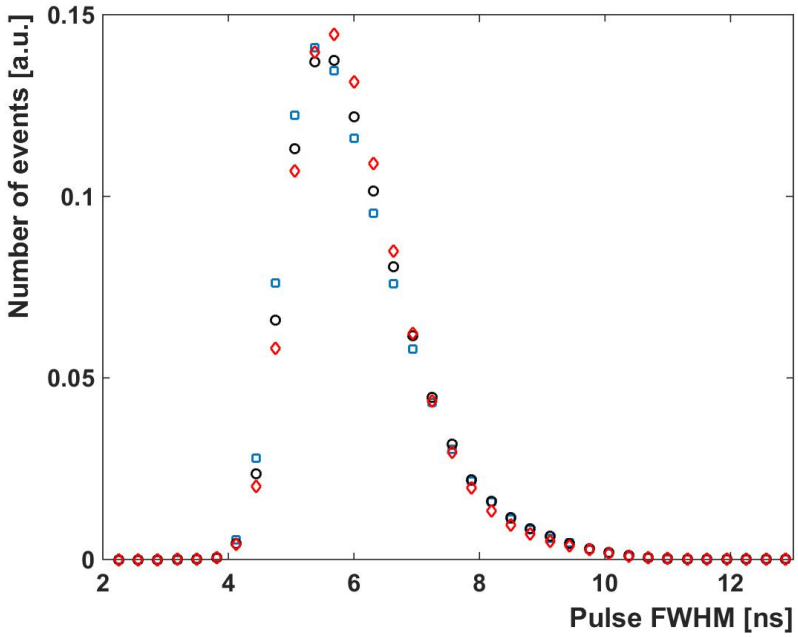

Figure 5.10: Distribution of the FWHM of the signal candidates for photon beam energies of 2, 3 and 7 MeV in blue squares, black circles and red rhombi, respectively. Only events with single candidates are considered in this figure. The error bars are not shown as they are smaller than the size of the points.

a MIP. This comparison is affected by the fact that signal candidates are selected by requiring the amplitude of the maximum of the detected peaks to exceed by 7 mV the pedestal voltage level. As a matter of comparison, the expected most probable amplitude of the MIP signal is 7 mV. This leads to only the upper part of the spectrum of interacting photons being selected which biases the distribution of the collected charge significantly. The mean collected charge for photons is thus normalized using the value for electrons emitted by Sr^{90}. For the calibration procedure, the diamond sensor is placed in between the radioactive source and a scintillating plate read out by a photomultiplier tube. The latter is used as a trigger signal in coincidence with the signal from the diamond sensor to which a threshold is placed at 7 mV. As a side effect the spectrum of the electrons which are selected by this procedure is modified and their energy is on average simulated to be about 1.5 MeV, close to the MIP energy. This ratio is close to unity and does not vary significantly between 2 and 7 MeV as presented in Fig. 5.11. This value is compared to a GEANT4 simulation, seen in the previous section, for which the energy deposition in a 500 μm thick diamond sensor is computed as a function of the energy. The average energy deposition is computed both for incident photons of energies varying from 1 to 10 MeV and for electrons of 1.5 MeV. Only energy depositions in excess of 280 keV, which corresponds to the threshold of 7 mV in the trigger, are included in the average. The determination of the ratio of energy depositions from the simulation is deteriorated mainly from uncertainties related to the actual energy spectrum of incident electrons that are selected by the trigger and from uncertainties in the conversion of the voltage threshold to a deposited energy threshold. For the former, the maximum deviation of the average energy deposition of 0.5, 1 and 2 MeV electrons compared to 1.5 MeV electrons is taken as a correlated uncertainty for all the points. For the latter, the maximum deviation for the ratio of energy deposition for photons versus 1.5 MeV electrons with a threshold of 224 and 336 keV with respect to a 280 keV threshold is used as a correlated uncertainty. It is the dominant uncertainty. The simulation and the experiment are in agreement.

Given the low efficiency of the diamond sensor to photons, the detection of successive ones when running in the *bunched* configuration is rare. Some events were nevertheless found and one of them is shown in Fig. 5.12. As expected from Fig. 5.10, two successive signal events separated by 16.8 ns are distinguishable. The time structure of the photon beam is measured distributing the difference in time of the signals from the BPM and the diamond sensor. It is shown for both *bunched* and *regular* running conditions in Fig. 5.13. Secondary γ beams separated by multiples of the bucket duration of 5.6 ns are visible with approximate relative rates of 10^{-4} in both running conditions. Such events are expected due to the long duration of the DFELL laser beam and the fact that electrons are populating

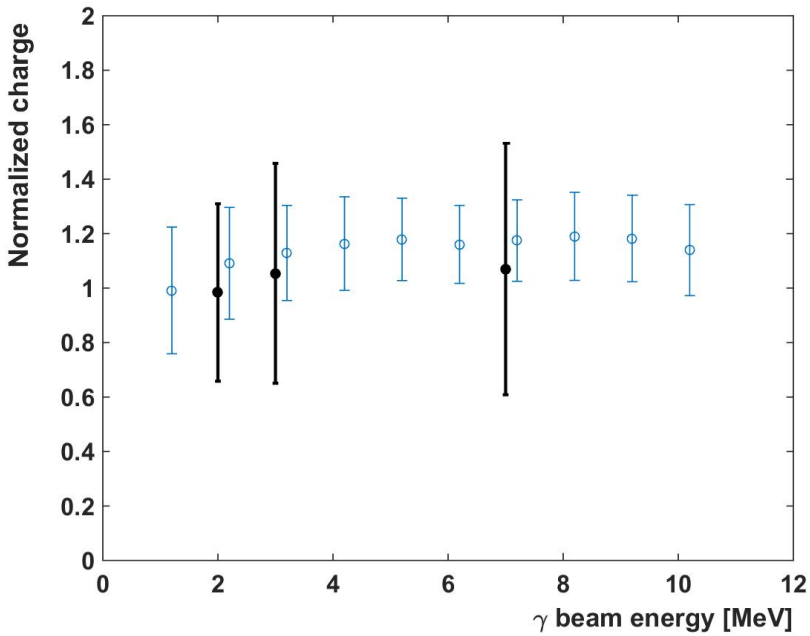

Figure 5.11: Mean collected charge for γ beam energies of 2, 3 and 7 MeV normalised by the value for electrons which have energies close to those of MIPs is given in black filled circles., see text for details. Error bars correspond to the RMS of the collected charges for photons. The blue unfilled circled represent the expectation from a GEANT4 simulation. Errors related to the simulation are correlated. The collected charge is found to be roughly independent of the photon energy, as expected from the simulation.

several buckets at the injection in the DFELL. The secondary peak at 179 ns in *regular* mode is related to the detection of photons from two successive collisions at 5.58 MHz. The relative magnitude of these peaks is of the order of 4×10^{-4} which is related to the product of the geometrical acceptance, the efficiency of the detector to 3 MeV photons and the number of photons in the two bunches. A value of around 0.3% is obtained for the diamond detection efficiency which is the number of photons detected divided by the total number of photons traversing the diamond sensor. An independent estimation of the diamond sensor efficiency is made using the measured event rates. The ratio of event rates of the diamond sensor and the 5-paddle is measured to be of approximately 0.5, see Figs. 5.14 and 5.15. Given the expected efficiency of the 5-paddle of about 0.7% [93], the estimated efficiency of the diamond sensor turns out to be of 0.35%. Both estimates are consistent within 25% which can be explained by the various approximations made.

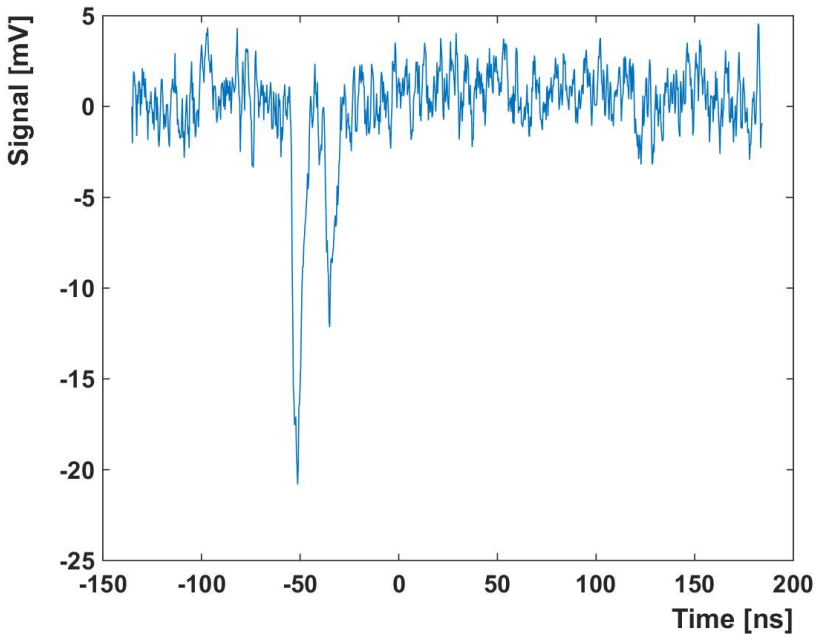

Figure 5.12: An event with two candidates separated by approximately 16 ns showing the excellent separation of two consecutive peaks.

A good proportionality between the diamond rate measurement and the 5-paddle flux monitor is observed but with relative fluctuations of 20%. Averaging over tens of minutes allowed measuring event rates by scanning the main vertical and horizontal axes around the centre of the beam. Data at 7 MeV is used to perform scans in both axes with a circularly polarised photon beam. The result

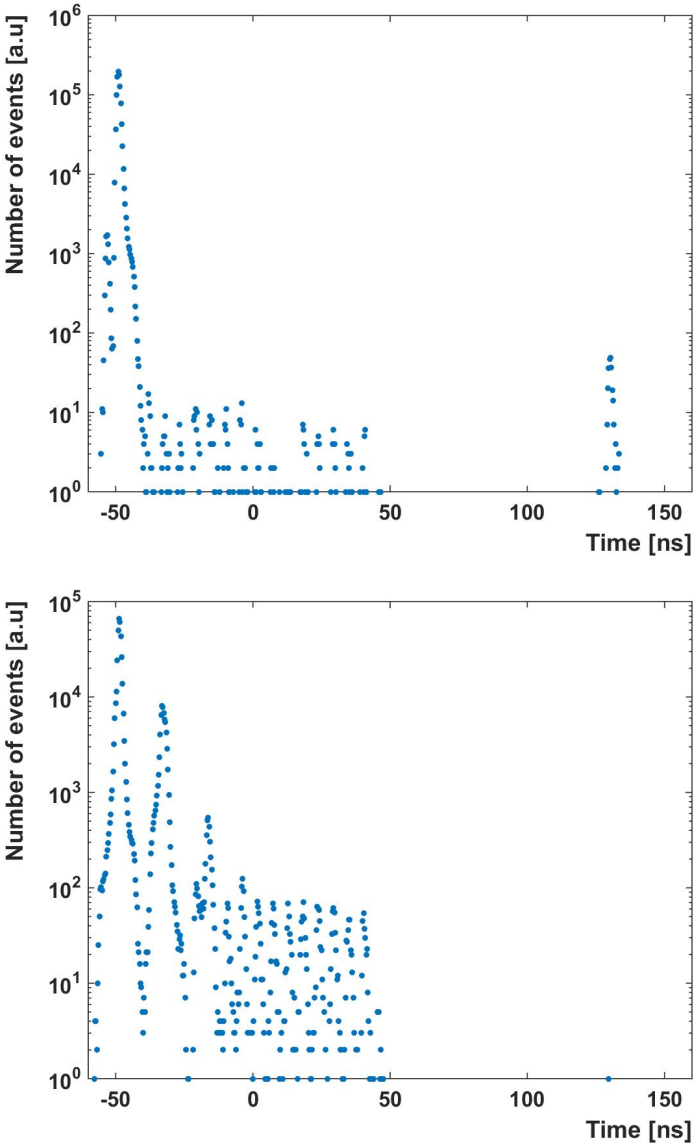

Figure 5.13: Distribution of the arrival time of the photons with respect to the trigger for *regular* (top) and *bunched* running conditions (bottom) at 3 MeV. In *regular* mode a secondary peak separated from the first one by 179 ns is observed as expected. Three main peaks separated by approximately 16 ns are seen in *bunched* mode. There is no event uncorrelated with the time structure of the DFELL accelerator, especially 100 ns after the main peak, which indicates that any physical background is negligible in this analysis.

is shown in Fig. 5.14 and compared to the expectation of Eq. 5.11 for head-on Compton backscattering and polarized electron beams [40] with conditions similar to those used in the actual data taking process. Assuming constant electron beam charge and laser flux the measured event rate is expected to be proportional to the cross-section of the Compton process integrated over the geometrical acceptance of the detector

$$\sigma_C = \int_{(x,y)\in\mathcal{A}} \frac{d\sigma}{dxdy} dxdy, \text{ with} \tag{5.11}$$

$$\frac{d\sigma}{dxdy} = \frac{L}{\left(L^2+x^2+y^2\right)^{3/2}} \frac{(1-\beta^2)r_0^2}{(1-\beta\cos\theta)^2} \frac{k_f^2}{2k_i^2}\big(A + S_1 B + S_2 C\big), \tag{5.12}$$

$$A = 1+\cos^2\theta^* + (k_i - k_f)(1-\cos\theta^*), \tag{5.13}$$

$$B = \sin^2\theta^* \cos 2\phi, \tag{5.14}$$

$$C = \sin^2\theta^* \sin 2\phi, \tag{5.15}$$

$$k_f = \frac{1}{1-\cos\theta^* + 1/k_i}, \tag{5.16}$$

$$k_i = 2\gamma\frac{hc}{\lambda m_e}, \tag{5.17}$$

$$\cos\theta^* = \frac{\cos\theta - \beta}{1-\beta\cos\theta} \text{ where} \tag{5.18}$$

β and γ denote the relativistic factors related to the electron beam, m_e is the electron mass, λ is the laser wavelength, S_1 and S_2 are the Stokes parameters of the laser beam related to horizontal and 45° linear polarizations, respectively, $r_0 \simeq 2.8 \times 10^{-15}$ m is the classical electron radius, $\theta = \arctan(\sqrt{x^2+y^2}/L)$, $\phi = \arctan(y/x)$, and x, y and L are the positions in the horizontal, vertical and longitudinal axes in the laboratory frame with respect to the interaction point, respectively. The integration is performed in the plane $z = L$ over the area $\mathcal{A}$ which represents the square diamond sensor with the surface outside the acceptance of the circular aperture removed. Both experimental distributions of Fig. 5.14 are compatible with each other and with the simulation in the central region of ± 7.5 mm around the centre of the beam within approximately 5%. Due to the lack of a detailed model of the collimator and potential misalignment of the centre of the photon beam with respect to the collimator, the tails of the distributions are not correctly replicated. Average event rates at each position are normalised by the average 5-paddle flux monitor over the scan, the RMS value of the latter being used to compute the error bars. The contribution of the statistical uncertainty to the error bars is negligible. The normalisation of theory and data is obtained by equating the average over the five most central points. The data is shifted by 2.5 mm in the horizontal plane due to an imprecise pre-alignment. Residual misalignment of less than 2.5 mm is not corrected for.

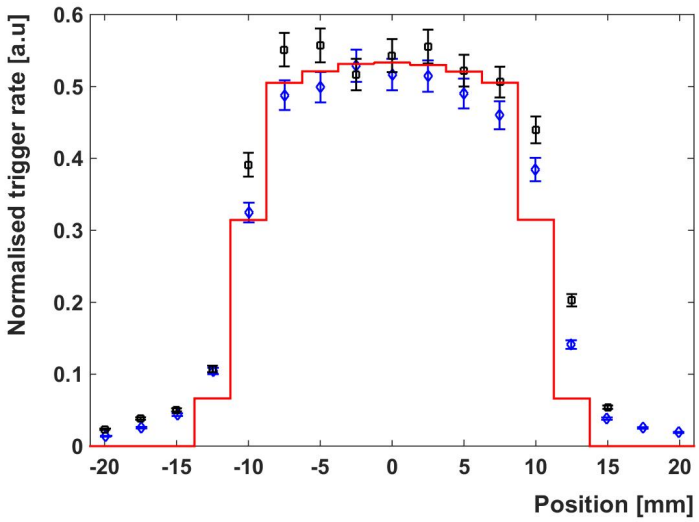

Figure 5.14: Event rates for circularly polarised photon beam as a function of the horizontal (blue squares) and vertical (black rhombi) position, normalised by the 5-paddle average flux over the duration of the measurement. Error bars represent the variation of the flux obtained with the 5-paddle during the measurement. The red line represents the simulation without a detailed description of the collimation system.

The comparison of data and theory for horizontally polarised beam is given in Fig. 5.15. In both cases, data is compatible with expectations. The transverse shape of the beam is expected to depend on the polarisation of the laser beam [40, 94] which is closely related to the polarisation of the photon beam for on-axis photons provided that smearing effects are small and that the energy of the electron beam is not polarized [95]. However, the expected difference in shape is only of a few percent for purely linearly and circularly polarised beams. They cannot be distinguished from one another with the actual data. To do so would require higher precision experiments.

5.2.3 Discussion

This experiment demonstrates the operation of a diamond detector as a fast photon sensor to distinguish photon bunches separated by approximately 16 ns. It has been used to probe the time structure of the photon beam of the free electron laser at HIγS. The main targeted use of the diamond detector is thus validated before installation at ELI-NP-GBS. It will also allow monitoring the time structure of the photon beam. Thus, it will be useful to check the synchronisation and overlap of the electron and laser beams.

The relative precision of the flux measurements are of the order of a few percent as required for its use in ELI-NP-GBS. The main difficulties encountered are related to the low efficiency of the detector and the fact that rates instead of amplitudes of signal are measured. While the DFELL offers a high repetition rate and a low flux of photons per bunch, the ELI-NP-GBS machine will be in the opposite regime, specifically, a repetition rate of 100 Hz and a flux of 10^7 photons per bunch. This regime will allow performing actual measurements of the deposited charge, rather than the event rates, in order to probe variations in the intensity of each photon bunch. By putting the diamond sensor only a few metres away from the Compton interaction point, the geometrical acceptance of the diamond sensor will also be increased.

An evaluation of the shape of the photon beam by scanning the diamond in the beam seems to be feasible, provided that it is made before the collimator and with more stable conditions. Such a device may thus also be useful for absolute positioning of the beam in an external reference frame if, for instance, a laser tracking target is attached to the mechanics of the diamond sensor. An investigation of four-quadrant diamond detectors may also be advantageous to increase the sensitivity to the position of the centre of the beam and to its shape. This was done in the following experiment, described in the next section.

The collected charge is found to be independent of the energy of the photons in the range 2 to 7 MeV. Simulations suggest it should be true in the range 1 to 10 MeV. The diamond sensor may advantageously be used as a precise and

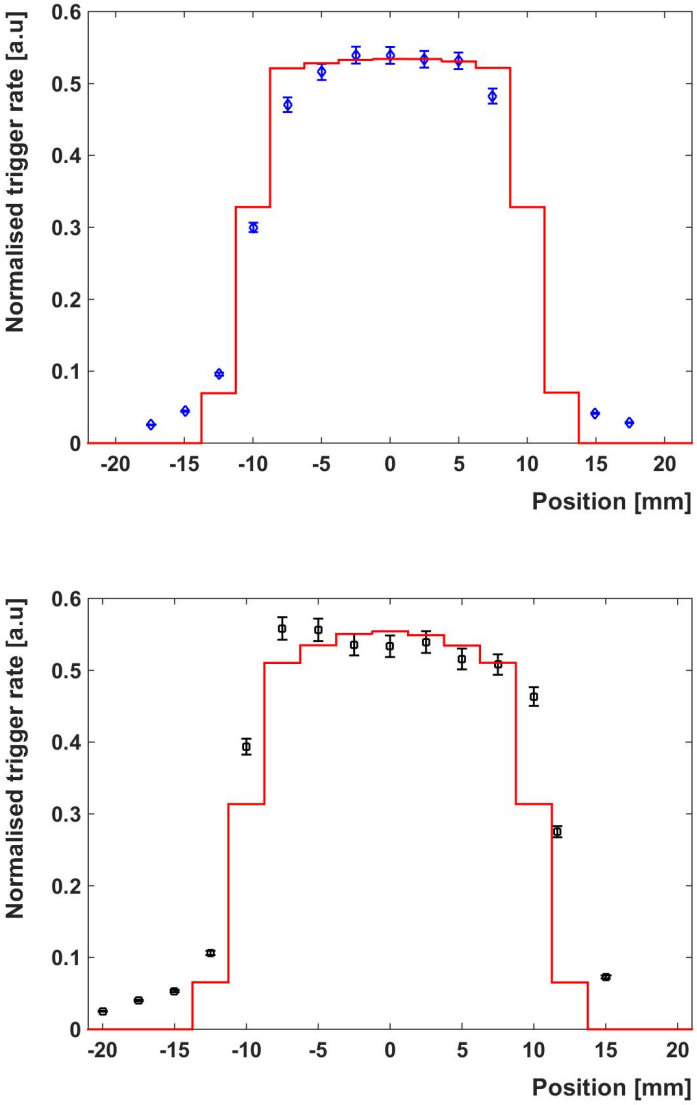

Figure 5.15: Event rates for horizontally polarised photon beam as a function of the horizontal (top) and vertical (bottom) position, normalised by the 5-paddle average flux over the duration of the measurement. Error bars represent the variation of the flux obtained with the 5-paddle during the measurement. The red line represents the simulation without a detailed description of the collimation system.

linear tool for absolute flux measurements in this range in the regime of single interactions. This requires carefully checking the linear response of the detector. Precise calibration of the charge with a known radioactive source (γ emitter) is also needed to ensure this mode of operation. With a large flux of photons, as expected with the ELI-NP-GBS, the interaction probability must be accounted for. Simulations suggest that the average energy deposited per incoming photon is varying by a factor of two in the range 0.1 to 100 MeV. A detailed experimental study of the scale and the energy dependence of this value is required to allow absolute flux measurements with the diamond sensor in a high flux photon source. On site cross calibrations will be possible at ELI-NP-GBS thanks to a calorimeter [62] dedicated to the characterisation of the average flux. This will allow for an investigation of ageing effects that could arise.

5.3 Test at newSubaru

5.3.1 Set-up

After the demonstration of a working set-up at HIγS, a second experiment was organised at newSubaru, between June 13th and June 24th 2016, to determine more qualitatively the performance of our detector. A number of improvements were made for this purpose. First of all, the detector was changed to a 4-quadrant detector that offers extra information on the intensity gradient of the gamma beam by comparing measurements quadrant to quadrant. A photo of the detector is show in Figure 5.16. The downside of this is that it increases the chances of mistakes or mishandling as each quadrant needs its own preamplifier. Indeed, one of them was more noisy than the others. This could not be solved during the data-taking. The Wavecatcher was changed to a more recent version with 8 channels where 6 channels were used: 1 for each quadrant, 1 for the trigger given by the clock of the accelerator and 1 was connected to a photodiode monitoring the laser to ensure its stability during run time.

The filter-wheel to test the different thicknesses of tungsten was completely removed as it could not bring them close enough to the diamond. Instead, a mount was manufactured with a 3D printer to bring the tungsten layer to within 2 mm of the diamond surface, as seen in Figure 5.17. This however necessitates physical intervention each time a different thickness is to be tested. This is facilitated by the ease of access to the experimental hutch, shown in Figure 5.18, that only needs a few seconds to put shielding in front of the $20 \times 30mm^2$ absorber hole to make the hutch a radiation free area. The distance between the laser-electron interaction point and the detector located in the aforementioned experimental hutch is 22.4 m.

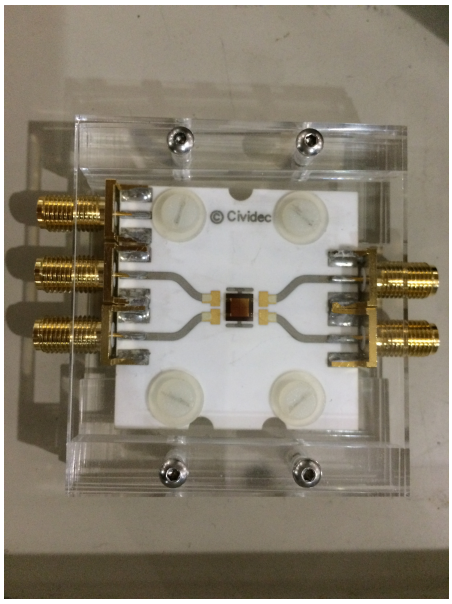

Figure 5.16: Photo of the 4-quadrant diamond detector used during the experiments at newSubaru.

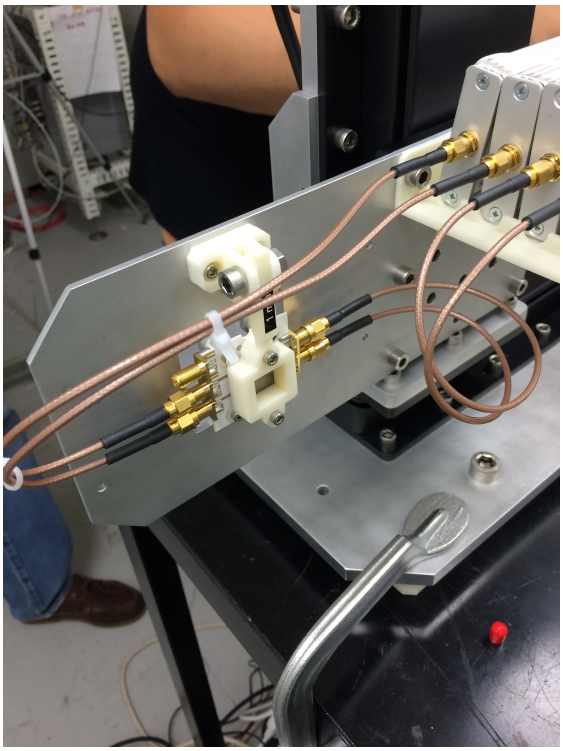

Figure 5.17: Photo of the detector with the tungsten mount in front of it. Here the thickness is 1 mm.

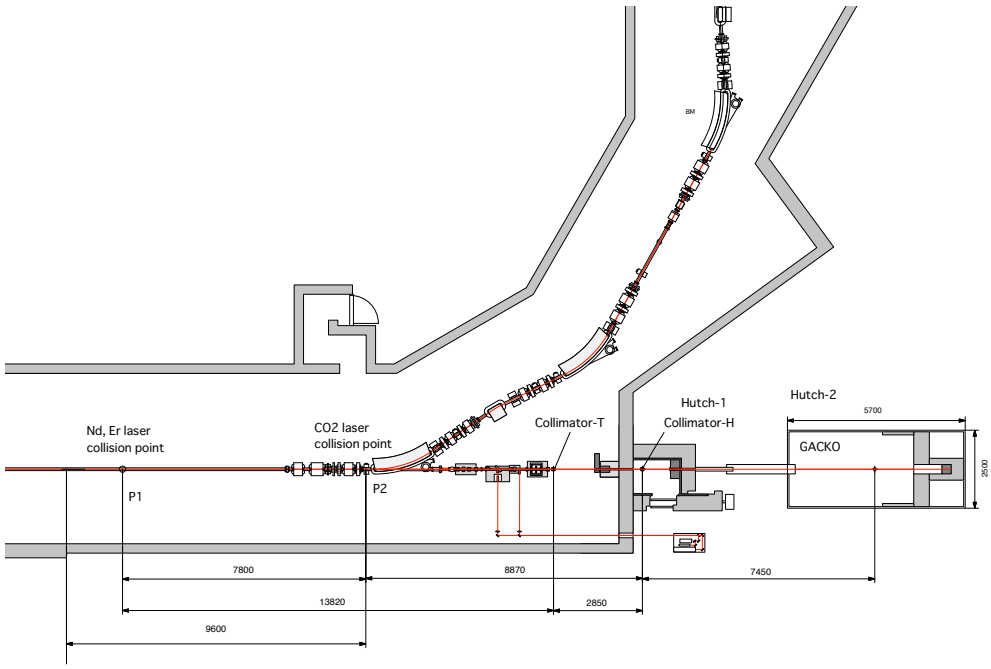

Figure 5.18: Detail of the floor plan at newSubaru depicting Beamline 1 and its experimental hutch.

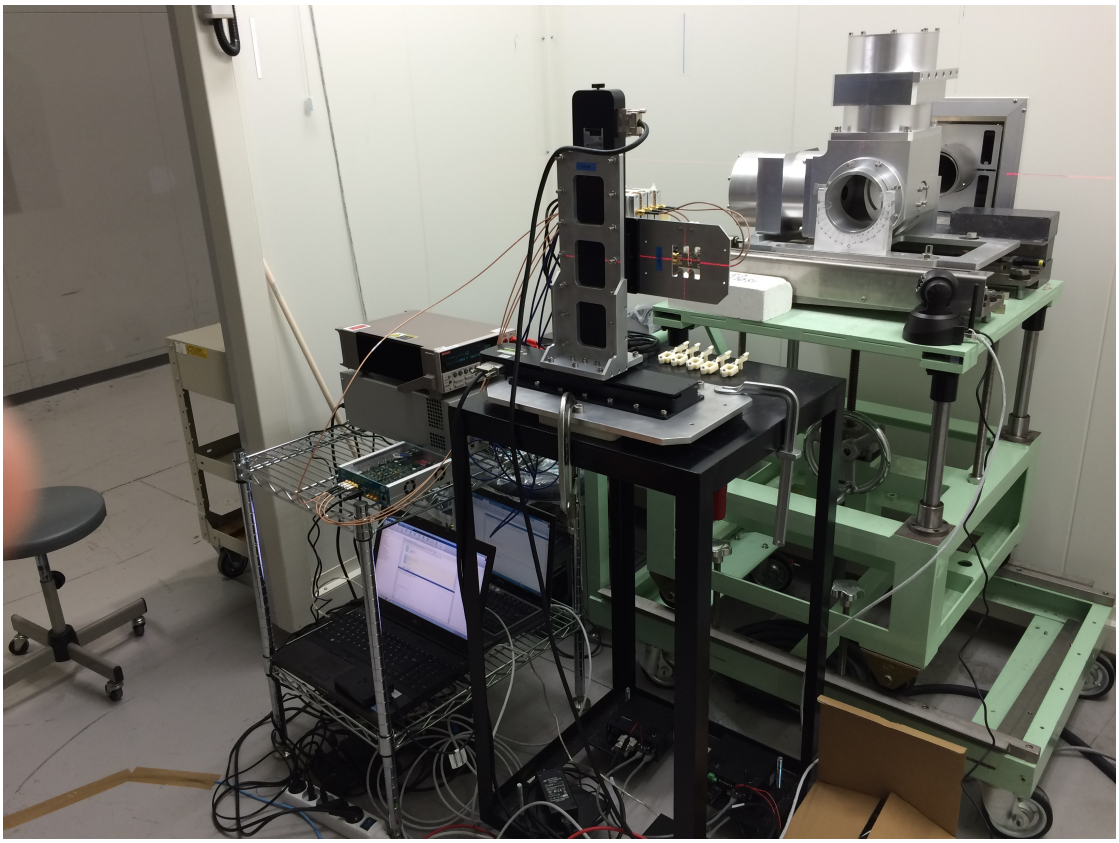

Figure 5.19: Photo of the experimental set-up at newSubaru.

The typical signal measured by the Wavecatcher for one run of 6000 events is shown in Figure 5.20, after performing a baseline correction by subtracting the average of the first 100 points to each event signal individually. It can then be used like this or in the smooth version which is when a running average filter over 10 points is applied to each signal with the *smooth* function in MATLAB. Candidates are found by using the *findpeaks* function with a minimum height and prominence of 8 mV. Sometimes, multiple candidates can be found in the same event as shown in Figure 5.21.

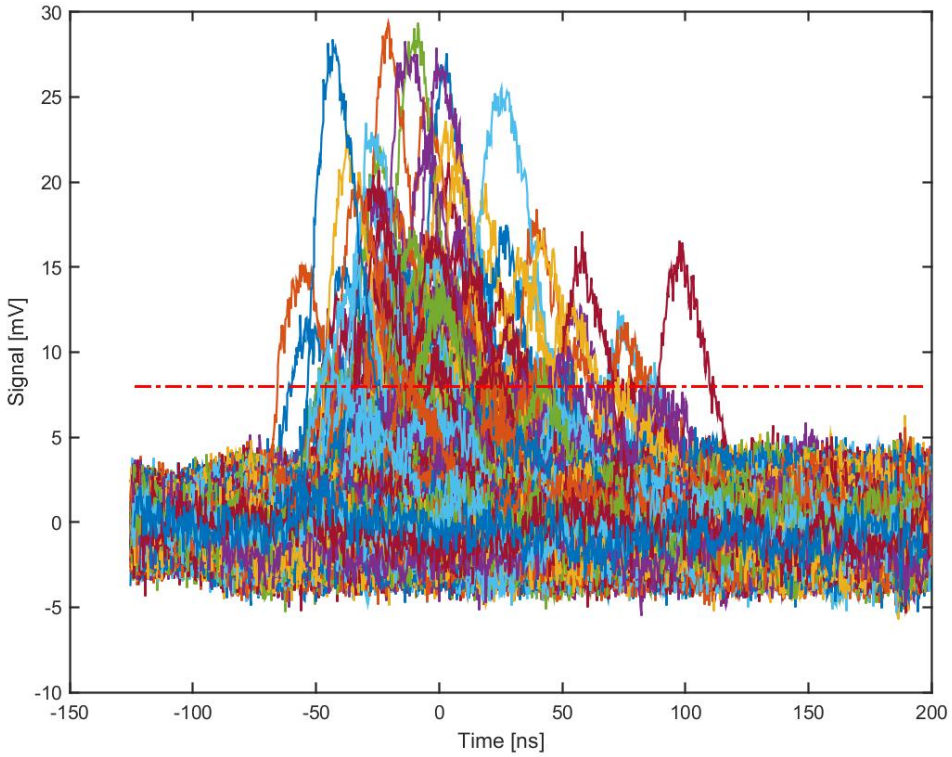

Figure 5.20: Signal of a run of 6000 triggered events for quadrant 4 of the detector with laser power of 16.8 W. The dashed line represents the cut-off of 8 mV for selecting candidate peaks.

5.3.2 Centre of beam

The detector is first placed approximately on the centre of the gamma beam by using a laser tracker already on site present for this purpose. At this point, we take, for example, 60000 triggered events. We then look at each individual quadrant

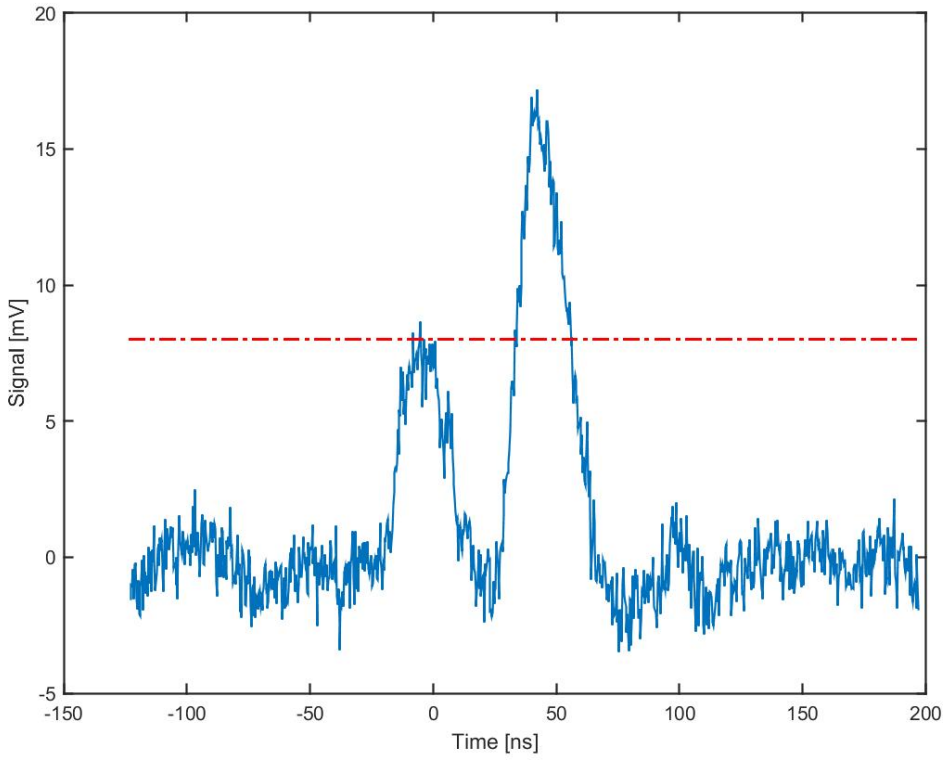

Figure 5.21: One event was found with multiple peaks in the run presented in the previous figure.

and count the number of candidates of gamma-rays interacting in the detector. From this number of candidates per quadrant, a derivative is calculated with the operations $(N_2 + N_4) - (N_1 + N_3)$ in the x-axis and $(N_1 + N_2) - (N_3 + N_4)$ in the y-axis with N_{1-4} the number of candidates in quadrants 1 to 4 following the numbering convention shown in Figure 5.3. If the derivative is positive (negative), the detector is moved in the positive (negative) direction, by a step of 0.1mm using the translation plates. This is repeated until the derivative is close enough to zero depending on the precision desired and the time available. This procedure was validated effectively and will be useful during the commissioning of the machine as an extra tool to verify the gamma beam is indeed centred on the right axis.

5.3.3 Laser Power dependence

We measured the mean amplitude of the signal in the detector as a function of laser power. This was found to be constant in the range 1 to 19 W available on the present laser. This is shown on Figure 5.22, with the straight lines being linear fits matching a flat slope.

5.3.4 Laser Frequency dependence

A second experiment was performed, this time varying the repetition rate of the laser by 2 kHz increments between 15 and 25 kHz. Again, this has no effect on the average amplitude of the signal as seen on Figure 5.23, with the fit again giving a flat slope.

5.3.5 Tungsten thickness testing

The next step in the experiment was to validate the use of the tungsten preshower in front of the diamond detector. As stated previously, the thicknesses used were 0.5, 0.75, 1 and 2 mm. When computing the mean integral over the FWHM of each peak over the number of total events (Figure 5.24) or the number of peaks detected (Figure 5.25), we see a sharp rise between 0 and 1 mm before a stabilisation at 2 mm. The same behaviour was observed in the simulations, as can be seen in Figure 5.5. This leads us to the conclusion that if tungsten is to be used at ELI-NP to increase the total efficiency of the detector, the preferred tungsten thickness will be 1 mm.

5.3.6 Scan beam-shape and polarisation

Finally, the more time-consuming experiment conducted was testing the scanning procedure. This was done by moving the detector by 1 mm steps along the x-axis,

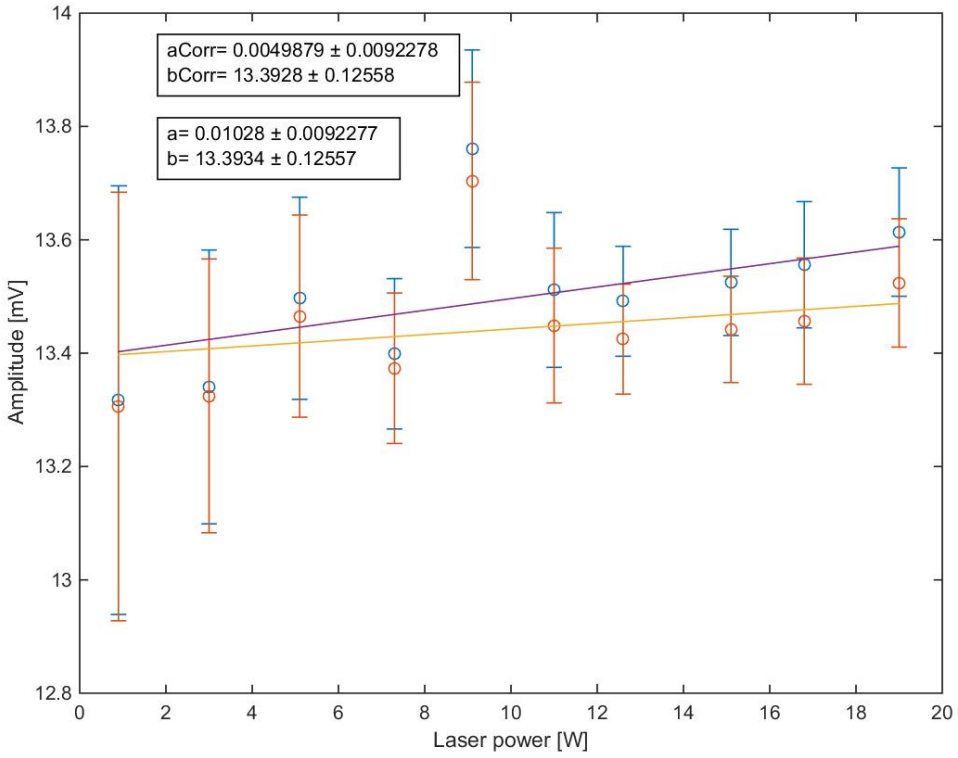

Figure 5.22: Mean amplitude of signal as a function of laser power

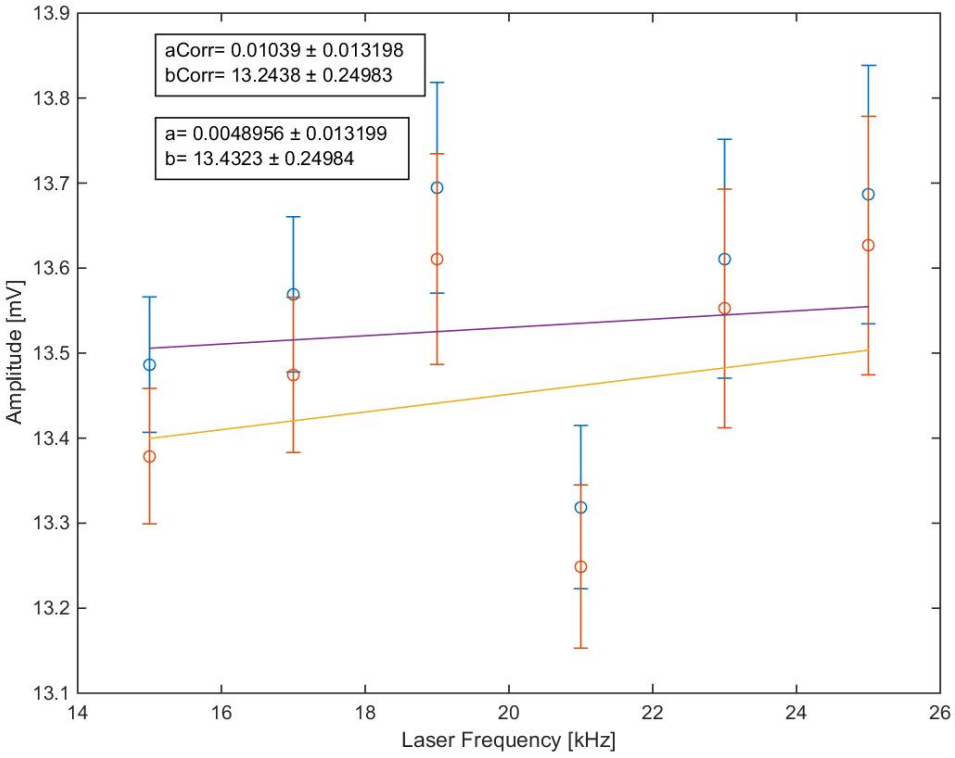

Figure 5.23: Mean amplitude of signal as a function of laser power

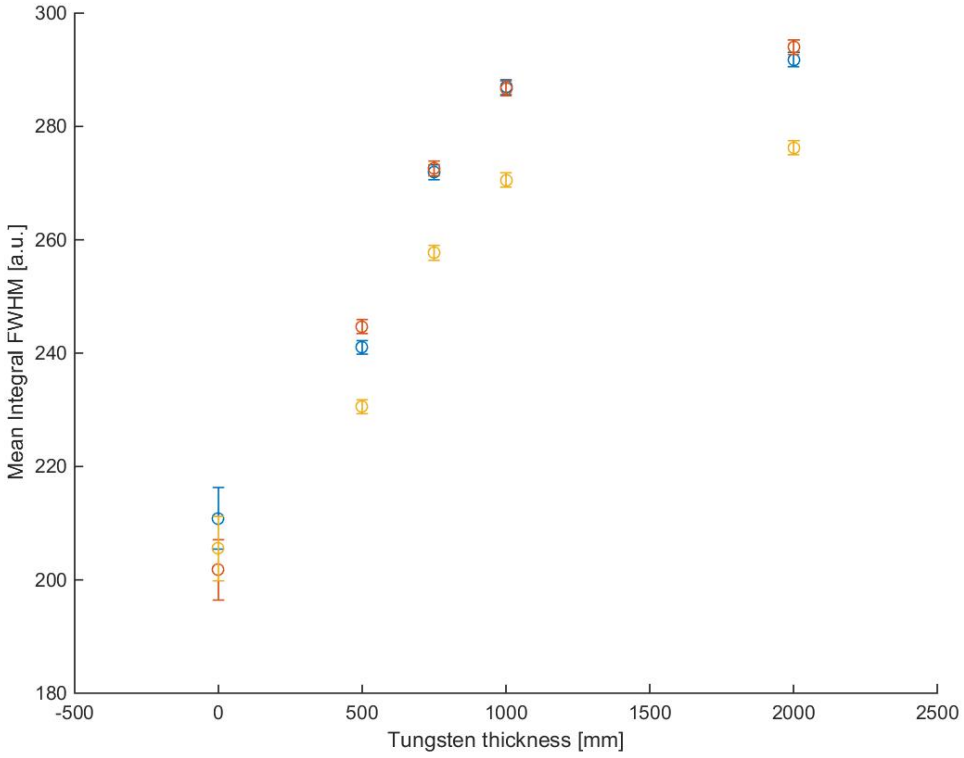

Figure 5.24: Mean integral of signal as a function of tungsten thickness

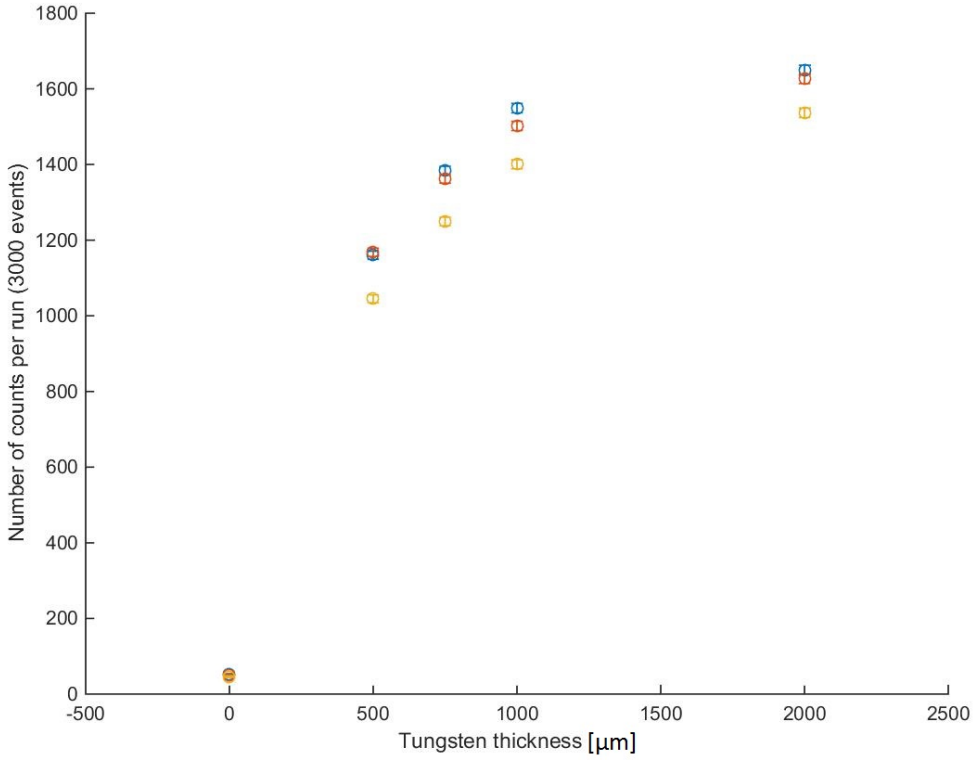

Figure 5.25: Number of counts where one event was detected as a function of tungsten thickness

a determined number of times. At the end of each line, the detector was shifted by 1 mm in the y-direction to obtain in the end a square grid of positions. For each position a run of 6000 events was taken. From this, we can take the number of peak candidates for each position and create a 2D map of the beam shape. We can get more granular information by taking the quadrants individually. Since they are separated by 1.5 mm, the stepping of 1 mm gives information for every 0.5 mm apart from the first and last position. Various examples of scans are presented in Figures 5.26-5.29. The beam presents a circular shape when the polarisation of the laser is circular. The beam shape is elliptical for a linear polarisation with the orientation given by the direction of polarisation of the laser. This is clearly visible in the Figures 5.27-5.29 where the global shape of the beam is similar but rotated according to polarisation. The x and y axes are the same for the four figures with the colours representing the number of candidates detected at each position from blue lowest to red highest.

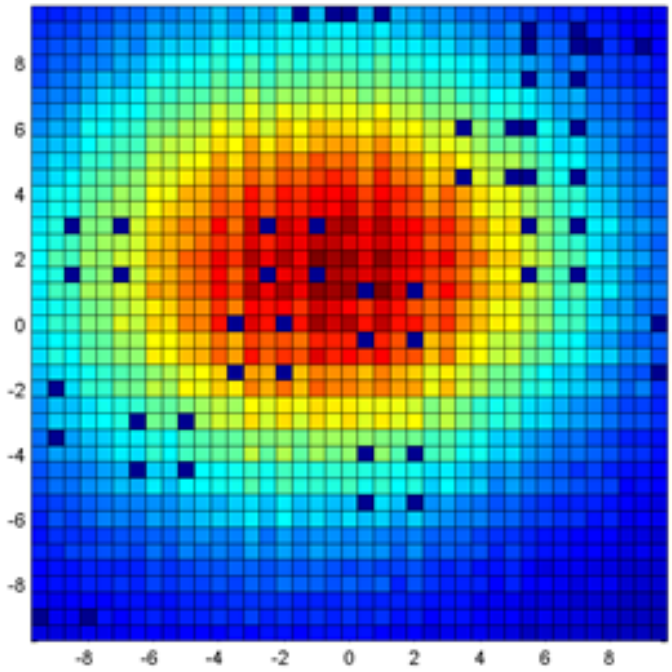

Figure 5.26: Projection of the gamma beam profile after a scan in x and y, with a circular laser polarisation. Some positions are missing due to corrupted files during data transfer.

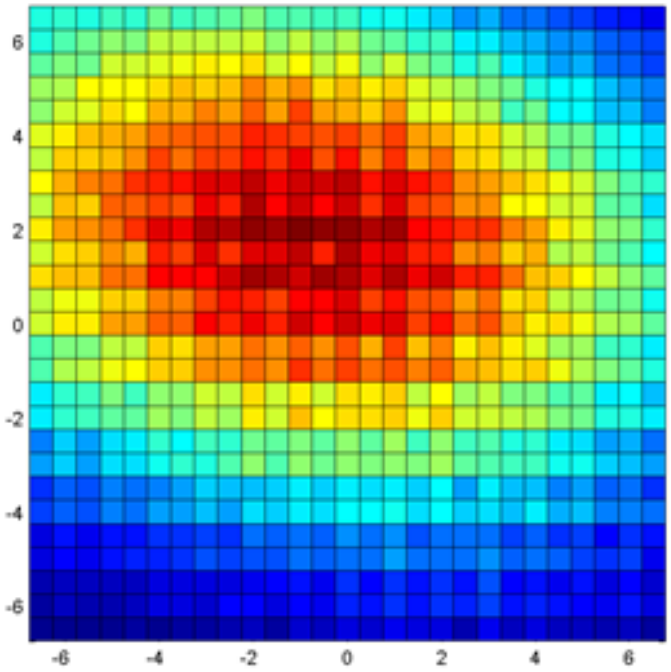

Figure 5.27: Projection of the gamma beam profile after a scan in x and y, with the laser linearly polarised at 22°.

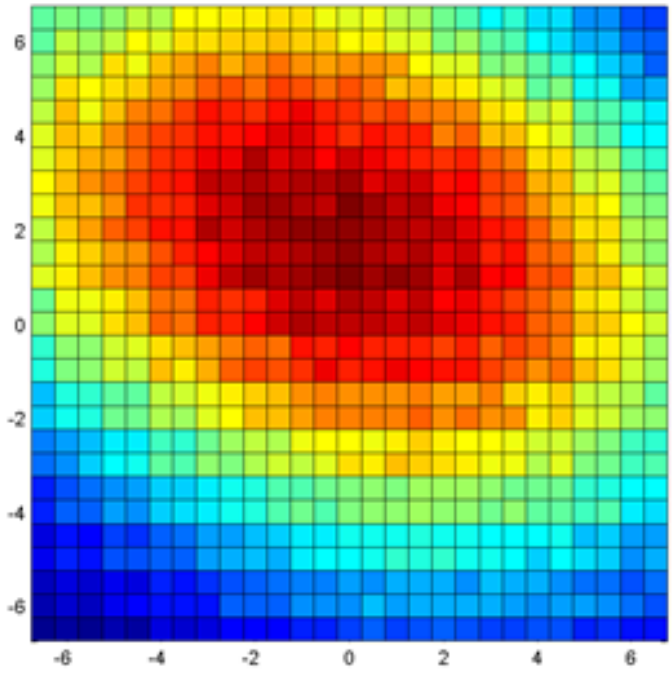

Figure 5.28: Projection of the gamma beam profile after a scan in x and y, with the laser linearly polarised at 45°.

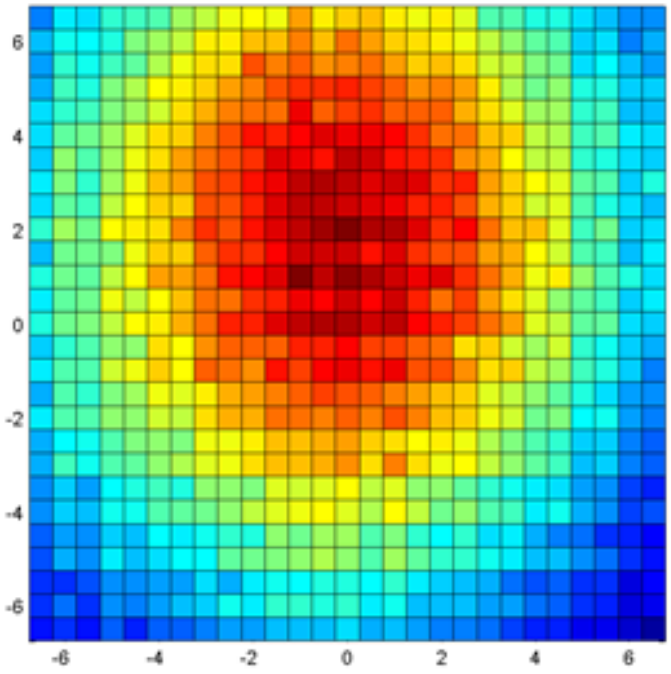

Figure 5.29: Projection of the gamma beam profile after a scan in x and y, with the laser linearly polarised at 90°.

5.4 Installation

A vacuum chamber designed at LAL will enclose the diamond detector. It is to be installed on the gamma beam axis about 2.6 m after the first interaction point. It is big enough to hold the detector as well as its two translation plates to place it at the desired position. A drawing of the chamber is shown on Figure 5.30.

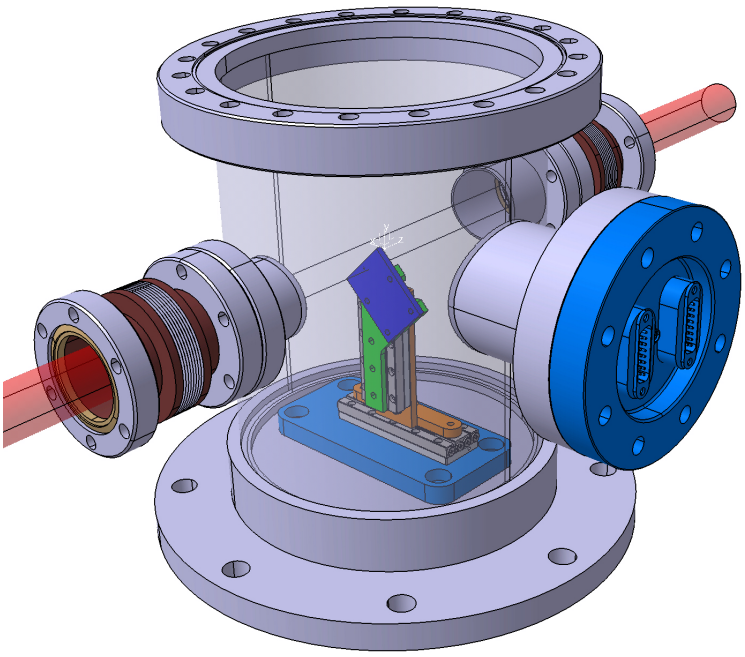

Figure 5.30: 3D Model of the vacuum chamber containing the diamond detector and its translation plates.

The detector itself will be almost identical to the one used during the experiments at newSubaru: a $4.5 \times 4.5 \times 0.5 mm^3$ diamond with 4-quadrant metallisation on a ceramic plate. The only difference is the diamond is positioned near one of the edges of the plate, of size $37 \times 28 mm^2$. A photo is shown in Figure 5.31. This is a custom design made by CIVIDEC for this application. Indeed, this is done so that the detector can be placed as close as possible to the centre of the gamma beam during run time. This will enable live-monitoring without deteriorating the central part which carries on to the user room.

The same set-up will also be used for the second high-energy interaction point, for which the completion point is in the more distant future. The vacuum chamber containing the detector is expected to be 6.3 m after this second interaction point.

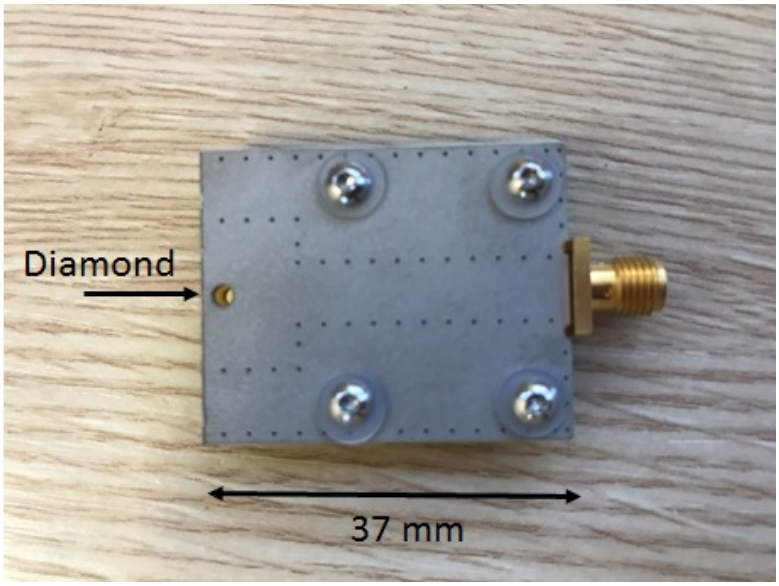

Figure 5.31: Photo of the final design of the diamond detector to be installed at ELI-NP. The diamond is situated on the left edge, under the round hole in the shielding that protects the electronics.

5.5 Chapter summary

In this final chapter, we delved in detail into the characteristics of the diamond sensor and the results from two experiments performed at HIγS and newSubaru, validating its future use for the ELI-NP project. First, simulations enabled an understanding of the physical processes at work during the passage of gamma-rays in a layer of diamond. They also demonstrated the absence of background noise due to the accelerator. For the first time a diamond-detector was used to study qualitatively a gamma beam and the results are presented and validate this proof of principle. The detector proves it is fast enough and can resolve photons separated by 16 ns, an essential condition for its eventual utilisation where it needs to ensure without a doubt the good overlapping, both spatially and temporally, of each individual laser-electron bunch pair. Beam-shape measurements were also executed and indicate that the verification of the gamma beam polarisation is possible.

Conclusion

In the first two chapters, an overview of gamma-rays, their discovery, detection methods and means of production, essentially through inverse Compton source machines has been presented. This was done to situate the problem this thesis is trying to resolve: having an online diagnostic system to ensure continuously the good overlapping both temporally and spatially of the laser and electron bunches of the ELI-NP inverse Compton gamma source. This is essential for the functional operation of the completed machine as a user facility.

In the context of the ELI-NP project, and more specifically, the optical recirculator system that necessitates a very fine and complex alignment procedure, a real-time monitoring system was developed to ensure the correct production of a gamma beam to be delivered to users. Indeed, it is used to check individually the collision of a laser pulse 32 times with 32 electron bunches separated by 16 ns. For this purpose, a diamond detector was chosen for multiple reasons. Its compact size lets it fit inside a vacuum chamber that will be installed directly on the beam pipe. The use of two translation plates will enable the detector to scan the beam, find its centre or simply wait to be used off-axis without needing to break the vacuum. Diamond is naturally radiation hard, which is important for the long-term lifetime of the system in the radiation-prone environment of an accelerator. Coupled with low-noise amplifiers and the Wavecatcher data-acquisition system, the diamond detector presents signals with an FWHM of 6 ns, which is fast enough to resolve successive photons separated by 16 ns. This was the first time, to our knowledge, that the photon beam time structure on the scale of a few nanoseconds has been probed with a detector.

A 4-quadrant detector was also tested to great success. This will not only enable to report on the quality of interaction but also on the position of the gamma beam with respect to its beam pipe. The use of a tungsten preshower has also been validated, with a thickness of 1 mm giving a ten-fold increase in gain, albeit blurring the spatial resolution.

Lastly, an advantage of diamond in this precise use case is its low efficiency to gamma rays. Indeed, the detector might be used during commissioning to monitor the beam while other instruments further downstream necessitate access to the

beam as well. With an efficiency lower than 1%, the detector can be used in parasitic mode while having a negligible effect on the beam. Of course, it can be just moved out of the way remotely using the translation plates connected to the control command if it becomes in any way a hindrance. The final design of the system also presents a detector at the edge of its base-plate to enable it to probe the region near the centre of the beam without obstructing the beam that continues through the collimator until the user room.

Transverse beam shape measurements were performed by scanning the beam in 1 mm steps. This imaging technique matches well with the expected results from simulation where the shape of the gamma beam is governed by the polarisation of the interaction laser.

Bibliography

[1] Paul Villard. Sur la réflexion et la réfraction de rayons cathodiques et des rayons déviables du radium. *Comptes rendus hebdomadaires des séances de l'académie des sciences*, 130:1010–1012, 1900.

[2] Paul Villard. Sur la rayonnement du radium. *Comptes rendus hebdomadaires des séances de l'académie des sciences*, 130:1178–1179, 1900.

[3] Leif Gerward. Paul Villard and his discovery of gamma rays. *Physics in perspective*, 1(4):367–383, 1999.

[4] E. Rutherford. The magnetic and electric deviation of the easily absorbed rays from radium. *The London, Edinburgh, and Dublin Philosophical Magazine and Journal of Science*, 5(26):177–187, 1903.

[5] Douglas C Giancoli. *Physics for scientists and engineers*. Pearson Education International, 2008.

[6] Joen M. Iannucci and Laura Jansen Howerton. *Dental radiography: Principles and techniques*. Elsevier, 2013.

[7] Richard A. Quinn, Claire C. Sigl, and John J. Callinan. *Radiography in Modern Industry, Fourth edition*. Eastman Kodak Company.

[8] Fujifilm Corporation. *The fundamentals of industrial radiography*. Fujifilm Corporation.

[9] Ronald Halmshaw. *Industrial radiology: theory and practice*, volume 1. Springer Science & Business Media, 2012.

[10] Centronic. *Geiger Müller tubes*. Centronic.

[11] Koji Wada, Toru Yoshikawa, and Masaru Murata. Decontamination work in the area surrounding fukushima dai-ichi nuclear power plant: Another occupational health challenge of the nuclear disaster. *Archives of Environmental & Occupational Health*, 67(3):128–132, 2012. PMID: 22845725.

[12] Richard W. Bukowski and George W. Mulholland. *Smoke detector design and smoke properties*. U.S. Department of Commerce, National Bureau of Standards, 1978.

[13] L. Michel and E. Crépon. Arrêté du 18 novembre 2011 portant dérogation à l'article R. 1333-2 du code de la santé publique pour les détecteurs de fumée à chambre d'ionisation. *Journal officiel de la république française*, 2011.

[14] VK Zworykin, GA Morton, and L Malter. The secondary emission multiplier-a new electronic device. *Proceedings of the Institute of Radio Engineers*, 24(3):351–375, 1936.

[15] Toshikazu Hakamata. *Photomultiplier tubes*. Hamamatsu Photonics K. K., 1978.

[16] Glenn F Knoll. *Radiation detection and measurement*. John Wiley & Sons, 2010.

[17] Robert Hofstadter. Alkali halide scintillation counters. *Phys. Rev.*, 74:100–101, Jul 1948.

[18] Duc Vo. Comparison of portable detectors for uranium enrichment measurements. *Journal of Radioanalytical and Nuclear Chemistry*, 276(3):693–698, 2008.

[19] George L. Clark. *Encyclopedia of X-rays and Gamma rays*, chapter Gamma scintillation spectrometry: Determination of Uranium-235, page 410. Reinhold Publishing Corporation, 1963.

[20] Doug Reilly, Norbert Ensslin, Hastings Smith Jr, and Sarah Kreiner. Passive nondestructive assay of nuclear materials. Technical report, Nuclear Regulatory Commission, Washington, DC (United States). Office of Nuclear Regulatory Research; Los Alamos National Lab., NM (United States), 1991.

[21] C Ur, A Zilges, N Pietralla, J Beller, Bertrand De Boisdeffre, Mihail Cernaianu, Vera Derya, Bastian Löher, Catalin Matei, George Pascovici, C Petcu, Christopher Romig, D Savran, G Suliman, E Udup, and V Werner. Nuclear resonance fluorescence experiments at eli-np. *Romanian Reports in Physics*, 68:S483–S538, 2016.

[22] P B Moon. Resonant nuclear scattering of gamma-rays: Theory and preliminary experiments. *Proceedings of the Physical Society. Section A*, 64(1):76, 1951.

[23] Franz R Metzger. Nuclear resonance fluorescence in some heavy nuclei. *Journal of the Franklin Institute*, 261(2):219–236, 1956.

[24] Glen Warren, Jac Caggiano, and Patrick Peplowski. Potential applications of nuclear resonance fluorescence. In *AIP Conference Proceedings*, volume 1194, pages 106–119. AIP, 2009.

[25] William Bertozzi and Robert J Ledoux. Nuclear resonance fluorescence imaging in non-intrusive cargo inspection. *Nuclear Instruments and Methods in Physics Research Section B: Beam Interactions with Materials and Atoms*, 241(1-4):820–825, 2005.

[26] Dale L Bailey, David W Townsend, Peter E Valk, and Michael N Maisey. *Positron emission tomography*. Springer, 2005.

[27] U. Amaldi, G. Borghi, M. Bucciantonio, R. Kieffer, J. Samarati, F. Sauli, and D. Watts. Development of tof-pet detectors based on the multi-gap resistive plate chambers. *Nuclear Instruments and Methods in Physics Research Section A: Accelerators, Spectrometers, Detectors and Associated Equipment*, 778:85 – 91, 2015.

[28] S. Korpar, R. Dolenec, P. Križan, R. Pestotnik, and A. Stanovnik. Study of tof pet using cherenkov light. *Nuclear Instruments and Methods in Physics Research Section A: Accelerators, Spectrometers, Detectors and Associated Equipment*, 654(1):532 – 538, 2011.

[29] Lars Leksell. Stereotactic radiosurgery. *Journal of Neurology, Neurosurgery & Psychiatry*, 46(9):797–803, 1983.

[30] Börje Larsson, Kurt Liden, and Bert Sarby. Irradiation of small structures through the intact skull. *Acta radiologica: therapy, physics, biology*, 13(6):512–534, 1974.

[31] Jeremy Ganz. *Gamma knife neurosurgery*. Springer Science & Business Media, 2010.

[32] Lawrence S Chin and William F Regine. *Principles and practice of stereotactic radiosurgery*. Springer Science & Business Media, 2010.

[33] David I Thwaites and John B Tuohy. Back to the future: the history and development of the clinical linear accelerator. *Physics in Medicine & Biology*, 51(13):R343, 2006.

[34] Wendell Lutz, Ken R Winston, and Nasser Maleki. A system for stereotactic radiosurgery with a linear accelerator. *International Journal of Radiation Oncology• Biology• Physics*, 14(2):373–381, 1988.

[35] Richard T Kouzes, James H Ely, Luke E Erikson, Warnick J Kernan, Azaree T Lintereur, Edward R Siciliano, Daniel L Stephens, David C Stromswold, Renee M Van Ginhoven, and Mitchell L Woodring. Neutron detection alternatives to 3he for national security applications. *Nuclear Instruments and Methods in Physics Research Section A: Accelerators, Spectrometers, Detectors and Associated Equipment*, 623(3):1035–1045, 2010.

[36] SB Hosur and NM Badiger. Determination of rest mass energy of the electron—an undergraduate laboratory experiment. *European Journal of Physics*, 28(6):1233, 2007.

[37] Autorité de Sûreté Nucléaire. ASN website. *https://www.asn.fr/*, 2018.

[38] Arthur H Compton. A quantum theory of the scattering of x-rays by light elements. *Physical review*, 21(5):483, 1923.

[39] LD Landau and EM Lifshitz. *Quantum electrodynamics*. Pergamon Pr, 1983.

[40] U. Fano. Remarks on the classical and quantum-mechanical treatment of partial polarization. *J. Opt. Soc. Am.*, 39(10):859–863, Oct 1949.

[41] Eugene Hecht. *Optics, 4th Edition*. International edition, Addison-Wesley, San Francisco, 2002.

[42] Richard H Milburn. Electron scattering by an intense polarized photon field. *Physical Review Letters*, 10(3):75, 1963.

[43] FR Arutyunian and VA Tumanian. The compton effect on relativistic electrons and the possibility of obtaining high energy beams. *Physics Letters*, 4(3):176–178, 1963.

[44] FK Goward and David Errington Barnes. Experimental 8 mev. synchrotron for electron acceleration. *Nature*, 158(4012):413, 1946.

[45] T. H. Maiman. Stimulated optical radiation in ruby. *Nature*, 187(4736):493, 1960.

[46] Joseph Ballam, GB Chadwick, R Gearhart, Zaven GT Guiragossian, PR Klein, A Levy, M Menke, JJ Murray, P Seyboth, G Wolf, et al. Total and partial photoproduction cross sections at 1.44, 2.8, and 4.7 gev. *Physical Review Letters*, 23(9):498, 1969.

[47] Henry R Weller, Mohammad W Ahmed, Haiyan Gao, Werner Tornow, Ying K Wu, Moshe Gai, and Rory Miskimen. Research opportunities at the upgraded hiγs facility. *Progress in Particle and Nuclear Physics*, 62(1):257–303, 2009.

[48] Klaus Wille. *The physics of particle accelerators: an introduction*. Clarendon Press, 2000.

[49] MW Ahmed, AE Champagne, CR Howell, WM Snow, RP Springer, and Y Wu. Higs2: The next generation compton γ-ray source. *Prospectus Document for the Nuclear Science Advisory Committee*, 2012.

[50] Sho Amano, Ken Horikawa, Kazuki Ishihara, Shuji Miyamoto, Takehito Hayakawa, Toshiyuki Shizuma, and Takayasu Mochizuki. Several-mev γ-ray generation at newsubaru by laser compton backscattering. *Nuclear Instruments and Methods in Physics Research Section A: Accelerators, Spectrometers, Detectors and Associated Equipment*, 602(2):337–341, 2009.

[51] University of Hyogo. newsubaru website. *http://www.lasti.u-hyogo.ac.jp/NS-en/facility/ring/*, 2018.

[52] Gérard A. Mourou, Georg Korn, Wolfgang Sandner, and John L. Collier. *Extreme Light Infrastructure Whitebook: Science and Technology with Ultra-Intense Lasers*. THOSS Media, 2011.

[53] Sergei Kühn, Mathieu Dumergue, Subhendu Kahaly, Sudipta Mondal, Miklós Füle, Tamás Csizmadia, Balázs Farkas, Balázs Major, Zoltán Várallyay, Eric Cormier, et al. The eli-alps facility: the next generation of attosecond sources. *Journal of Physics B: Atomic, Molecular and Optical Physics*, 50(13):132002, 2017.

[54] Paul B Corkum. Plasma perspective on strong field multiphoton ionization. *Physical Review Letters*, 71(13):1994, 1993.

[55] Jonathan A Wheeler, Antonin Borot, Sylvain Monchocé, Henri Vincenti, Aurélien Ricci, Arnaud Malvache, Rodrigo Lopez-Martens, and Fabien Quéré. Attosecond lighthouses from plasma mirrors. *Nature Photonics*, 6(12):829, 2012.

[56] F Quéré, Cédric Thaury, P Monot, S Dobosz, Ph Martin, J-P Geindre, and P Audebert. Coherent wake emission of high-order harmonics from overdense plasmas. *Physical review letters*, 96(12):125004, 2006.

[57] B Rus, P Bakule, D Kramer, J Naylon, J Thoma, M Fibrich, JT Green, JC Lagron, R Antipenkov, J Bartoníček, et al. Eli-beamlines: progress

in development of next generation short-pulse laser systems. In *Research Using Extreme Light: Entering New Frontiers with Petawatt-Class Lasers III*, volume 10241, page 102410J. International Society for Optics and Photonics, 2017.

[58] T. Tajima and J. M. Dawson. Laser electron accelerator. *Phys. Rev. Lett.*, 43:267–270, Jul 1979.

[59] K. Oide, M. Aiba, S. Aumon, M. Benedikt, A. Blondel, A. Bogomyagkov, M. Boscolo, H. Burkhardt, Y. Cai, A. Doblhammer, B. Haerer, B. Holzer, J. M. Jowett, I. Koop, M. Koratzinos, E. Levichev, L. Medina, K. Ohmi, Y. Papaphilippou, P. Piminov, D. Shatilov, S. Sinyatkin, M. Sullivan, J. Wenninger, U. Wienands, D. Zhou, and F. Zimmermann. Design of beam optics for the future circular collider e^+e^- collider rings. *Phys. Rev. Accel. Beams*, 19:111005, Nov 2016.

[60] S K Barber, J van Tilborg, C B Schroeder, R Lehe, H-E Tsai, K K Swanson, S Steinke, K Nakamura, C G R Geddes, C Benedetti, E Esarey, and W P Leemans. Parametric emittance measurements of electron beams produced by a laser plasma accelerator. *Plasma Physics and Controlled Fusion*, 60(5):054015, 2018.

[61] Ahmed H Zewail. Femtochemistry: Atomic-scale dynamics of the chemical bond. *The Journal of Physical Chemistry A*, 104(24):5660–5694, 2000.

[62] L. Serafini et al. *EuroGammaS proposal for the ELI-NP Gamma beam System.* EuroGammaS, 2014.

[63] DT Palmer, RH Miller, H Winick, XJ Wang, K Batchelor, M Woodle, and I Ben-Zvi. Simulations of the bnl/slac/ucla 1.6 cell emittance compensated photocathode rf gun low energy beam line. In *Particle Accelerator Conference, 1995., Proceedings of the 1995*, volume 4, pages 2432–2434. IEEE, 1995.

[64] Triveni Rao and David H Dowell. An engineering guide to photoinjectors. *arXiv preprint arXiv:1403.7539*, 2014.

[65] F Le Pimpec, CJ Milne, CP Hauri, and F Ardana-Lamas. Quantum efficiency of technical metal photocathodes under laser irradiation of various wavelengths. *Applied Physics A*, 112(3):647–661, 2013.

[66] Donna Strickland and Gerard Mourou. Compression of amplified chirped optical pulses. *Optics communications*, 55(6):447–449, 1985.

[67] G. Cheriaux, P. Rousseau, F. Salin, J. P. Chambaret, Barry Walker, and L. F. Dimauro. Aberration-free stretcher design for ultrashort-pulse amplification. *Opt. Lett.*, 21(6):414–416, Mar 1996.

[68] W. Seka, S.D. Jacobs, J.E. Rizzo, R. Boni, and R.S. Craxton. Demonstration of high efficiency third harmonic conversion of high power nd-glass laser radiation. *Optics Communications*, 34(3):469 – 473, 1980.

[69] David Alesini, Roberto Boni, Mauro Migliorati, Valerio Pettinacci, Valerio Lollo, Luca Ficcadenti, Andrea Mostacci, Luigi Palumbo, Bruno Spataro, Roberto Di Raddo, et al. The damped c-band rf structures for the european eli-np proposal. In *IPAC2013: Proceedings of the 4th International Particle Accelerator Conference*, 2013.

[70] Kevin Dupraz. *Conception et optimisation d'un recirculateur optique pour la source haute brilliance de rayons gamma d'ELI-NP*. PhD thesis, Université Paris Sud, 2015.

[71] K Dupraz, K Cassou, N Delerue, P Fichot, A Martens, A Stocchi, A Variola, F Zomer, A Courjaud, E Mottay, et al. Design and optimization of a highly efficient optical multipass system for γ-ray beam production from electron laser beam compton scattering. *Physical Review Special Topics-Accelerators and Beams*, 17(3):033501, 2014.

[72] Princeton Instruments. PI-MAX4 webpage on the Princeton Instruments website. *https://www.princetoninstruments.com/products/PI-MAX4-emICCD*, 2018.

[73] G Paternò, Paolo Cardarelli, Michele Marziani, Enrico Bagli, Federico Evangelisti, Mirco Andreotti, Mauro Gambaccini, V Petrillo, I Drebot, A Bacci, et al. A collimation system for eli-np gamma beam system–design and simulation of performance. *Nuclear Instruments and Methods in Physics Research Section B: Beam Interactions with Materials and Atoms*, 402:349–353, 2017.

[74] M.G. Pellegriti, O. Adriani, S. Albergo, M. Andreotti, D. Berto, R. Borgheresi, G. Cappello, P. Cardarelli, E. Consoli, G. Di Domenico, F. Evangelisti, M. Gambaccini, G. Graziani, M. Lenzi, M. Marziani, L. Palumbo, G. Passaleva, A. Serban, M. Spina, O. Starodubtsev, M. Statera, A. Tricomi, A. Variola, M. Veltri, and B. Zerbo. Eurogammas gamma characterisation system for eli-np-gbs: The nuclear resonance scattering technique. *Nuclear Instruments and Methods in Physics Research Section*

A: Accelerators, Spectrometers, Detectors and Associated Equipment, 865:60 – 62, 2017. Physics and Applications of High Brightness Beams 2016.

[75] Paolo Cardarelli, Gianfranco Paternò, Giovanni Di Domenico, E Consoli, M Marziani, M Andreotti, Federico Evangelisti, Stefano Squerzanti, Mauro Gambaccini, Sebastiano Albergo, Gigi Cappello, A Tricomi, M Veltri, O Adriani, R Borgheresi, G Graziani, G Passaleva, A Serban, Oleksandr Starodubtsev, and Luigi Palumbo. A gamma beam profile imager for eli-np gamma beam system. *Nuclear Instruments and Methods in Physics Research Section A: Accelerators, Spectrometers, Detectors and Associated Equipment*, 893, 03 2018.

[76] DL Balabanski, F Ibrahim, A Krasznahorkay, I Boztosun, D Choudhury, S Coban, P Constantin, L Csige, PV Cuong, T Dickel, et al. Photofission experiments at eli-np. *Romanian Reports in Physics*, 68:S621–S698, 2016.

[77] L Csige, DM Filipescu, T Glodariu, J Gulyás, MM Günther, Dietrich Habs, HJ Karwowski, A Krasznahorkay, GC Rich, M Sin, et al. Exploring the multihumped fission barrier of 238 u via sub-barrier photofission. *Physical Review C*, 87(4):044321, 2013.

[78] Dimiter L Balabanski. Nuclear physics and astrophysics experiments at eli-np: The emerging future. In *EPJ Web of Conferences*, volume 165, page 01003. EDP Sciences, 2017.

[79] V.I. Goldanskii and V.A. Namiot. On the excitation of isomeric nuclear levels by laser radiation through inverse internal electron conversion. *Physics Letters B*, 62(4):393 – 394, 1976.

[80] CJ Chiara, JJ Carroll, MP Carpenter, JP Greene, DJ Hartley, RVF Janssens, GJ Lane, JC Marsh, DA Matters, M Polasik, et al. Isomer depletion as experimental evidence of nuclear excitation by electron capture. *Nature*, 554(7691):216, 2018.

[81] I-Yang Lee. The gammasphere. *Nuclear Physics A*, 520:c641–c655, 1990.

[82] Takeo Minamikawa, Naoki Tanimoto, Mamoru Hashimoto, Tsutomu Araki, Minoru Kobayashi, Katsumasa Fujita, and Satoshi Kawata. Jitter reduction of two synchronized picosecond mode-locked lasers using balanced cross-correlator with two-photon detectors. *Applied physics letters*, 89(19):191101, 2006.

[83] Sea Agostinelli, John Allison, K al Amako, Jo Apostolakis, H Araujo, P Arce, M Asai, D Axen, S Banerjee, G 2 Barrand, et al. Geant4—a simulation toolkit.

Nuclear instruments and methods in physics research section A: Accelerators, Spectrometers, Detectors and Associated Equipment, 506(3):250–303, 2003.

[84] J Apostolakis, G Folger, V Grichine, A Howard, V Ivanchenko, M Kosov, A Ribon, V Uzhinsky, and DH Wright. Geant4 physics lists for hep. In *Nuclear Science Symposium Conference Record, 2008. NSS'08. IEEE*, pages 833–836. IEEE, 2008.

[85] Hugo W Bertini. Intranuclear-cascade calculation of the secondary nucleon spectra from nucleon-nucleus interactions in the energy range 340 to 2900 mev and comparisons with experiment. *Physical Review*, 188(4):1711, 1969.

[86] J Apostolakis, A Bagulya, S Elles, VN Ivanchenko, O Kadri, M Maire, and L Urban. The performance of the geant4 standard em package for lhc and other applications. In *Journal of Physics: Conference Series*, volume 119. IOP Publishing, 2008.

[87] VN Litvinenko, B Burnham, M Emamian, N Hower, JMJ Madey, P Morcombe, PG O'Shea, SH Park, R Sachtschale, KD Straub, et al. Gamma-ray production in a storage ring free-electron laser. *Physical review letters*, 78(24):4569, 1997.

[88] YK Wu. Accelerator physics research and light source development programs at Duke University. In *Particle Accelerator Conference, 2007. PAC. IEEE*, pages 1215–1217. IEEE, 2007.

[89] CIVIDEC. Cividec website. *https://cividec.at/*, 2018.

[90] D. Breton. USB WaveCatcher: a USB-powered 12-bit 3.2GS/s digitizer. In *16th IEEE-NPSS Real Time Conference (RT09)*, Beijing, China, May 2009.

[91] Y. K. Wu, J. Li, P. Wang, and V. Litvinenko. BPM and orbit correction systems at the Duke storage ring. In *Particle Accelerator Conference, 2003. PAC. IEEE*, pages 2479–2481. IEEE, 2003.

[92] Argonne National Laboratory. Experimental Physics and Industrial Control System (EPICS) website. *http://www.aps.anl.gov/epics/index.php*, 2018.

[93] R.E. Pywell, O. Mavrichi, W.A. Wurtz, and R. Wilson. "photon flux monitor for a mono-energetic gamma ray source ". *Nuclear Instruments and Methods in Physics Research Section A: Accelerators, Spectrometers, Detectors and Associated Equipment*, 606(3):517 – 522, 2009.

[94] S.H. Park, V.N. Litvinenko, W. Tornow, and C. Montgomery. "spatial distribution and polarization of γ-rays generated via compton backscattering in the duke/ok-4 storage ring {FEL} ". *Nuclear Instruments and Methods in Physics Research Section A: Accelerators, Spectrometers, Detectors and Associated Equipment*, 475(1–3):425 – 431, 2001. FEL2000: Proc. 22nd Int. Free Electron Laser Conference and 7th F {EL} Users Workshop.

[95] I.F. Ginzburg, G.L. Kotkin, S.L. Panfil, V.G. Serbo, and V.I. Telnov. Colliding γe and $\gamma\gamma$ beams based on single-pass $e + e-$ accelerators II. Polarization effects, monochromatization improvement. *Nuclear Instruments and Methods in Physics Research*, 219(1):5 – 24, 1984.

Synthèse

Depuis des millénaires, la lumière a été une interrogation et une fascination pour les êtres humains mais sa compréhension n'a vraiment évolué que dans les 150 dernières années. La mécanique quantique a joué un rôle primordial avec le concept de dualité onde-corpuscule. La lumière peut être décrite à la fois comme une particule élémentaire, le photon, et à la fois comme une onde avec tous les principes physiques tels que la diffraction que cela implique. Dans cette thèse, nous nous préoccupons principalement de l'approche en tant que particule avec une emphase sur le domaine haute énergie du spectre électromagnétique : les rayons gamma entre 1 et 20 MeV. En effet, ceci est la gamme d'énergie nominale prévue pour la source de rayons gamma ELI-NP. Cette machine a pour but la production d'un faisceau pulsé de rayons gamma avec une bande passante rms inférieure à 0.5 % et une densité spectrale supérieure à 5000 photons/$(s.eV)$. Afin d'y arriver, un système optique complexe, appelé recirculateur, a été développé pour faire circuler une impulsion laser haute puissance 32 fois. La distance du chemin optique est de 16 ns pour qu'à chaque passage, au centre du système optique, l'impulsion laser puisse interagir avec un paquet d'électrons qui lui transfère son énergie pour générer un train de rayons gamma à une fréquence de 100 Hz. Chaque train est composé de 32 impulsions séparées individuellement de 16 ns. Une fois que la machine est mise en route, le recirculateur est mis sous vide et devient un système "boite noire" sur lequel on ne peut agir de l'intérieur. Il y a donc besoin de vérifier la superposition spatiale et temporelle du laser et des électrons. Cette problématique a été le fil conducteur de ma thèse.

La solution qui a été choisie fut le développement d'un système de contrôle en temps-réel basé sur un détecteur diamant. Il est capable de détecter les rayons gamma avec une résolution temporelle inférieure à 16 ns et sera installé à quelques mètres du point d'interaction.

Le chapitre 1 de la thèse se concentre sur l'histoire des rayons gamma. Premièrement, le contexte dans lequel ils furent découverts est présenté. Ensuite, leurs applications dans le domaine de la recherche nucléaire et médicale sont étudiées. Le sujet des différents instruments utilisés pour la détection des rayons gamma est étendu à travers divers exemples pratiques.

Le chapitre 2 porte sur deux types de sources de rayons gamma et comment elles sont utilisées par les physiciens dans des domaines tels que la médecine, la spectroscopie ou l'enseignement. Les éléments radioactifs sont la seule source naturelle de rayons gamma sur Terre. Lorsqu'un noyau excité se relaxe, il émet un photon d'une énergie discrète donnée. Ces niveaux d'énergies ont été étudiés en profondeur puisqu'ils permettent l'identification nucléaire des éléments. Les sources construites par l'homme n'existent que depuis quelques décennies grâce aux avancées technologiques dans les domaines des lasers et des accélérateurs de particules. Le principe de ces sources est la diffusion Compton inverse : des électrons sont accélérés avant d'entrer en collision avec les photons d'un laser. Au point d'interaction, un transfert d'énergie permet aux photons d'aller du domaine visible à celui des rayons gamma. Plusieurs machines de ce type existent de par le monde. Deux d'entre elles qui ont servi pour des expériences lors de mon doctorat sont présentées : High Intensity gamma Source à l'Université de Duke aux Etats-Unis et newSubaru à l'Université de Hyogo au Japon.

Une troisième machine Compton, ELI-NP Gamma Beam Source, est présentée dans le chapitre 3. Le laboratoire dans lequel j'ai travaillé, le Laboratoire de

l'Accélérateur Linéaire, s'occupe du développement de la majorité des composants optiques de la machine au sein de consortium EuroGammaS. Le système du recirculateur permet 32 interactions laser-électrons séparées par 16 ns.

Un aspect crucial pour la production du faisceau gamma est l'arrivée synchrone au point d'interaction des paquets d'électrons et des impulsions laser. Ceci nécessite une synchronisation de tous les éléments de la machine. Le chapitre 4 présente la procédure de synchronisation du système laser de la photocathode grâce à un cross-corrélateur optique développé au LAL.

De nombreux appareils sont nécessaires pour assurer la qualité et la stabilité du faisceau gamma. Un de ces appareils est le système de contrôle en temps-réel basé sur un détecteur diamant. Le diamant agit comme un semi-conducteur lorsqu'une haute tension lui est appliquée. Lors du passage d'un rayon gamma, de l'énergie est déposée à travers une interaction physique et un signal est enregistré. L'information extraite est essentielle pour vérifier la synchronisation avec $\Delta t < 1ps$ des impulsions laser et des paquets d'électrons, ainsi que de leur superposition spatiale. Ceci doit être fait online avec un détecteur indépendant du recirculateur, puisque ce dernier est pré-aligné manuellement avant d'être mis sous vide. Les expériences pour valider ce système de détecteur diamant sont présentées dans le chapitre 5.

Titre : Développement du système de contrôle en temps-réel basé sur un détecteur diamant pour la source de rayons gamma ELI-NP

Mots clés : accélérateur, rayons gamma, détecteur diamant, laser, polarisation

Résumé: Cette thèse présente le développement d'un système de contrôle en temps réel basé sur un détecteur en diamant pour la nouvelle source de rayons gamma en cours de construction à Magurele, en Roumanie, pour le projet Extreme Light Infrastructure (ELI). La machine comprend un accélérateur linéaire d'électrons qui se sépare en deux lignes, une à basse énergie entre 80 et 320 MeV et l'autre à plus haute énergie pouvant atteindre 720 MeV. Sur les deux lignes, un recirculateur optique guide un laser haute puissance pour entrer en collision avec 32 paquets d'électrons afin de produire des rayons gamma par interaction Compton inverse. Cette machine est construite par le consortium européen EuroGammaS, dont le Laboratoire de l'Accélérateur Linéaire fait partie et qui a pour mission de développer la plupart des composants optiques. C'est aussi là où j'ai préparé le travail présenté dans ce manuscrit.

Les paquets d'éléctrons séparés de 16 ns collisioneront avec une impulsion laser à une frequence de 100 Hz. Pour s'assurer de la qualité et de la stabilité de ces interactions, le système du détecteur diamant a été mis en place. Cela a impliqué du travail de simulation sous GEANT4 ainsi que des expériences pour tester l'équipement à HiGS aux Etats-Unis et à newSubaru au Japon, deux établissements scientifiques qui proposent aussi des sources de rayons gamma produits par interaction Compton inverse. Les résultats obtenus démontrent l'efficacité de ce système en analysant l'efficacité de détection, la charge collectée ou encore la forme de faisceau. Ceci est encourageant en vue de l'installation et du commissioning qui sont attendus pour 2019.

Title : Development of the diamond detector based real-time monitoring system for the ELI-NP gamma beam source

Keywords : accelerator, gamma rays, diamond detector diamant, laser, polarisation

Abstract: This thesis discusses the development of a real-time monitoring system based on a diamond detector for the new gamma source being built in Magurele, Romania as part of the Extreme Light Infrastructure (ELI) project. The machine consists of an electron linear accelerator that branches into two lines, one at low energy between 80 and 320 MeV and one at higher energy going up to 720 MeV. On both lines, an optical recirculator leads a high power laser to collide with 32 electron bunches to produce gamma rays by inverse Compton interaction. This machine is built by a European consortium named EuroGammaS, of which the Laboratoire de l'Accelerateur Lineaire is a member and tasked with developing most of the optical components. This is where I prepared the work presented in this manuscript.

The electron bunches separated by 16 ns will collide with a circulating laser pulse at a rate of 100 Hz. To monitor the quality and stability of these interactions, the diamond detector system has been set-up. This involved simulation work on GEANT4 as well as two experiments to test the equipment at HiGS in the USA and newSubaru in Japan, two facilities that also offer gamma ray beams produced by inverse Compton scattering. The results obtained demonstrate the effectiveness of the system by analysing detection efficiency, charge collected or beam shape. This is promising in anticipation of the installation and commissioning expected for 2019.